EVALUATION OF EARLY TUMOR ANGIOGENESIS USING ULTRASOUND ACOUSTIC ANGIOGRAPHY

Sarah E. Shelton

A dissertation submitted to the faculty of the University of North Carolina at Chapel Hill in partial fulfillment of the requirements for the degree of Doctor of Philosophy in the Department of Biomedical Engineering.

Chapel Hill
2017

Approved by:

Paul A. Dayton

Stephen R. Aylward

Andrew C. Dudley

Caterina M. Gallippi

Yueh Z. Lee

ABSTRACT

SARAH E. SHELTON: Evaluation of Early Tumor Angiogenesis Using Ultrasound Acoustic Angiography.
(Under the direction of Paul A. Dayton)

Cancer angiogenesis is a feature of tumor growth that produces disorganized and dysfunctional vascular networks. Acoustic angiography is a unique implementation of contrast-enhanced ultrasound that allows us to visualize microvasculature with high resolution and contrast, including blood vessels as small as 100 to 150 μm. These angiography images can be analyzed to evaluate the morphology of the blood vessels for the purpose of detecting and diagnosing tumors.

This thesis describes the implementation, advantages, and disadvantages of acoustic angiography and evaluates tumor vasculature in a pre-clinical cancer model. Measurements of tortuosity and vascular density in tumor regions were significantly higher than those of control regions, including in the smallest palpable tumors (2-3 mm). Additionally, abnormal tortuosity extended beyond the margin of tumors, as distal tissue separated from the tumor by at least 4 mm exhibited higher tortuosity than healthy individuals. Vascular tortuosity was negatively correlated to distance from the tumor margin using linear regression.

Analysis of full images to detect tumors was performed using a reader study approach to assess visual interpretations, and quantitative analysis combined tortuosity with spatial relationships between vessels using a density-based clustering approach. Visual assessment using a reader study design resulted in an area under the receiver

operating characteristic (ROC) curve of approximately 0.8, and the ROC curve was significantly correlated with tumor diameter, indicating that larger tumors were detected more accurately using this approach. Quantitative analysis of the same images used a density-based clustering algorithm to combine vessels in an image into clusters based on their tortuosity (using 2 metrics), radius, and proximity to one another. In tumors, highly tortuous vessels were closely packed, forming large clusters in the analysis, while control images lacked such patterns and formed much smaller clusters. Therefore, maximum cluster size was used to detect tumors, achieving an area under the ROC curve of 0.96.

Finally, superharmonic molecular imaging was used to image targeted microbubbles with higher contrast to tissue ratios than conventional molecular imaging. These molecular images were combined with vascular acoustic angiography images to begin to relate the expression of endothelial markers of angiogenesis with vascular features such as tortuosity.

To my parents, for teaching me the excitement of science, the importance of making a plan, and for inspiring creativity and curiosity in this and every endeavor.
But mostly for their unwavering support and encouragement.

ACKNOWLEDGMENTS

First, I would like to thank my wonderful friends and family for all their support. My parents, sister, and husband have been especially kind and enthusiastic over the years, and I cannot thank them enough for their love and encouragement. My dear friends keep me grounded and in touch with the real world, and remind me of the things that truly matter. I thank my extended family for always expressing interest in what I'm working on, no matter how long I've been in school, and for many fun gatherings and distractions when I needed them.

I also greatly appreciate the support of my colleagues and mentors. I thank my adviser, Paul Dayton, for sharing his advice since I joined the lab in 2012 and for often letting me determine which projects I was excited to work on. To the rest of my committee, Caterina Gallippi, Drew Dudley, Yueh Lee, and Stephen Aylward, I value the help and guidance I have received from all of you at different points during my graduate career. I would not have been as successful without your expertise and your willingness to share it with me. To my allies in the lab, thank you for your companionship, constructive feedback, and cooperation with me. Some of my favorite moments have been in-depth discussions of interesting research questions and our attempts to answer them. I am especially indebted to Dr. Brooks Lindsey for his collaboration across several years and many publications. Also, to Sneha Rao and Jodi Stone, for their help analyzing data and for lots of Matlab code that we wrote together. Several of the experiments described in this thesis would not have been possible without the

cooperation of the Mouse Phase 1 Unit and the Animal Studies Core, especially Alain Vadivia and Mark Ross who spent many hours in the imaging room with me every week. Each of these individuals and all my co-authors have played a vital role in this research.

I am also grateful for the support I received from the National Institute of Health, first through the Integrative Vascular Biology Training program (T32HL069768), then through a Predoctoral to Postdoctoral Fellow Transition Award (F99CA212227). These opportunities have allowed me extra freedom, especially to orient my research toward my interests in angiogenesis, cancer biology, and molecular imaging.

TABLE OF CONTENTS

LIST OF FIGURES

LIST OF TABLES

LIST OF ABBREVIATIONS

2D	Two-dimensional
3D	Three-dimensional
Ang	Angiopoietin
ANOVA	Analysis of variance
AUC	Area under the curve
bFGF	Basic fibroblast growth factor
BIRADS	Breast imaging reporting and data system
B-mode	Brightness mode
CEUS	Contrast enhanced ultrasound imaging
CI	Confidence interval
CPS	Cadence pulse sequence
CT	Computed tomography
CTR	Contrast to tissue ratio
dB	Decibel
DBSCAN	Density based statistical clustering of applications with noise
DM	Distance metric
DSPC	1,2-distearoyl-*sn*-glycero-3-phosphocholine
DSPE	1,2-distearoyl-*sn*-glycero-3-phosphoethanolamine
ECM	Extracellular matrix
eNOS	Endothelial nitric oxide synthase
FVB/NJ	Friend virus B NIH Jackson
GBM	Glioblastoma multiforme
HIF	Hypoxia inducible factor
ICAM-1	Intercellular adhesion molecule 1

IGF	Insulin-like growth factor
IHC	Immunohistochemical
IRB	Institutional review board
Hz	Hertz
MI	Mechanical index
MMP	Matric metalloproteinase
MRA	Magnetic resonance angiography
MRI	Magnetic resonance imaging
PBS	Phosphate-buffered saline
PDGF	Platelet-derived growth factor
PET	Positron emission tomography
PEG	Polyethylene-glycol
PFC	Perfluorocarbon
PlGF	Placental-derived growth factor
PNP	Peak negative pressure
Rb	Retinoblastoma
Re	Reynolds number
RF	Radiofrequency
RGD	Arg-Gly-Asp
RNA	Ribonucleic acid
ROC	Receiver operating characteristic
ROI	Region of interest
SPECT	Single photon computed tomography
SOAM	Sum of angles metric
SV40	Simian virus 40
TGF-β	Transforming growth factor beta

TNF-α	Tumor necrosis factor alpha
ULM	Ultrasound localization microscopy
VCAM-1	Vascular cell adhesion molecule 1
VEGF	Vascular endothelial growth factor
VEGFR	Vascular endothelial growth factor receptor

CHAPTER 1

BACKGROUND

1.1 OVERVIEW

This dissertation uses contrast-enhanced superharmonic ultrasound imaging, known as "acoustic angiography", to examine vascular patterns in tumor and healthy tissue, with a focus on breast cancer. Several aims are addressed in this work:

1. Characterization of normal and pathological patterns of vascularization using acoustic angiography.

2. Determining the performance of acoustic angiography images for tumor detection using visual and quantitative methods.

3. Extension of the high-resolution, superharmonic imaging technique to molecular imaging of targeted microbubbles.

The first chapters of this document describe the background and context of the work, including information about breast cancer, vasculature and angiogenesis, contrast-enhanced ultrasound, as well as details about the mechanisms that enable acoustic angiography and how it is implemented. The subsequent chapters describe several experiments performed in order to address the project aims, which are all focused on improving tumor detection and diagnosis using this unique imaging modality. The first experiments described explore vascular tortuosity and density in spontaneous tumors developed in a genetically engineered mouse model of breast cancer, and the

relationship between tumor size and these parameters. Tumor detection, through image classification, is performed using qualitative and quantitative approaches and also correlated to tumor size. The development of high-resolution superharmonic molecular imaging is also discussed, and initial experiments were performed to relate molecular and morphological images in tumors.

1.2 BREAST CANCER

Breast cancer represents a significant disease burden in the United States as well as across the world. It is the most common form of cancer in females, accounting for 14% of all new cancer cases in the U.S., and the 3rd leading cause of cancer mortality in females [1]. Approximately 13% of women in the U.S. will be diagnosed with breast cancer during their lifetime. Overall, almost 90% of women diagnosed with breast cancer will survive 5 years after diagnosis, but survival depends greatly on the stage of disease at diagnosis because the relative survival is only 25.9% for metastatic disease, compared to 98.6% and 84.6% for localized and regional disease, respectively [1]. Thus, early detection of tumors before they reach the metastatic stage is an important clinical goal in order to maximize patient survival.

Though treatments for breast cancer have become more effective, in part due to a greater understanding of differences between tumor subtypes and driving factors contributing to the growth of different tumors, patient outcomes in advanced stage cancers are still poor [1–4]. Therefore, imaging techniques such as mammography, ultrasound, and magnetic resonance imaging (MRI) are at the forefront of screening and diagnosis, but each suffer from limitations in sensitivity and specificity. Widespread screening mammography has facilitated early detection and resulted in reduced breast cancer-related morbidity and improved progression-free survival and overall survival [5, 6].

However, mammography is imperfect and results in frequent false positives that produce psychological distress in patients and a high number of biopsies [7–10]. While mammograms are effective at identifying suspicious lesions, they perform poorly at distinguishing between benign and malignant conditions. It is estimated that the cumulative risk of a false positive finding after 10 screening mammograms is approximately 50%, which results in several follow-up visits, diagnostic imaging examinations, and sometimes invasive biopsy procedures [11].

While it is unlikely that any imaging modality will soon replace mammography as a widespread screening tool for breast cancer, other imaging modalities are frequently utilized for diagnosis of lesions identified by mammography. Due to the high cost and time required for MRI, ultrasound is commonly used for follow-up imaging, but the specificity of both mammography and diagnostic ultrasound is low (approximately 70%), so biopsies are used to confirm diagnosis. This results in a many biopsies performed every year, with a small proportion of them ($\approx$20%) confirming the presence of cancer.

Acoustic angiography is a recently developed method for contrast-enhanced ultrasound imaging that provides information about blood vessels rather than the shape and size of a lesion, as can be seen on mammograms or traditional B-mode ultrasound. By taking advantage of unique, nonlinear characteristics of microbubble contrast agents and a prototype transducer, we can form an image of the vascular micro-environment supplying a tumor, rather than trying to visualize the tumor itself. Highly vascular lesions are more likely to be malignant [12], and acoustic angiography would provide a very sensitive indication of the degree of vascularity. Beyond that, it also allows visualization of the vascular tortuosity, which is likely to be an even more specific indicator of disease and has been shown in MRI angiography studies of brain cancer to be sensitive to disease recurrence before tumors are visible with tissue imaging modalities [13]. If acoustic angiography successfully improves diagnostic specificity, it would

decrease the false-positive rate and could lead to a significant reduction in the number of unnecessary biopsies performed each year.

1.3 TUMORS AND HYPOXIA

Healthy tissue is arranged such that organized layers of cells are supplied with oxygen and nutrients by vasculature in the surrounding stroma. The distribution and spacing of capillaries is largely determined by the metabolic needs of the specific tissue type, with larger spacing in supportive tissues such as smooth muscle and connective tissue and closer spacing in metabolically active tissues such as muscle fibers, and especially the central nervous system [14]. Though distance between capillaries varies between species and tissue types, healthy tissue is usually located less 100 μm from a capillary, and histological examinations by Krough in 1919 observed no tissue beyond 200 μm from an open capillary [15].

Pathological tissue does not display the same regularity seen in healthy tissue, and may exhibit increased, decreased, or heterogeneous vascular spacing, depending on the disease processes occurring. Several studies of the micro-architecture of tumor tissue have shown that while different types of tumors and even adjacent regions of a single tumor are heterogeneous, their growth produces hypoxia, which promotes neovascularization through the process of angiogenesis [16–19]. Healthy capillary spacing balances oxygen diffusion with metabolism, because tissue beyond the oxygen diffusion limit will be subjected to hypoxia and metabolic stress, which is common in tumors and contributes to their pathophysiology.

Hypoxia can be transient or chronic and is difficult to measure *in vivo*, so most measurements have used fixed tissues to look a distance between capillaries and necrosis (a sign of chronic hypoxia or anoxia), or *in vitro* systems. Studies of tumors in the lung showed that avascular tumor cords with a radius greater than 200 μm exhibited

necrosis, but those with a radius less than 160 μm did not [16]. Olive et al. measured the oxygen diffusion distance to be 100-200 μm by removing cubes of tumor tissue, incubating them in an oxygenated environment, and then tagging hypoxic cells to measure distance to the oxygen interface [17]. Taken together, these studies suggest that the maximum oxygen diffusion distance in tumors may vary, but that it is unlikely to be greater than 200 μm, and likely less than that in many cases. Hypoxia induces a variety of protective signaling pathways, including anti-apoptotic and pro-angiogenic signal cascades, largely mediated through hypoxia inducible factors, especially HIF-1α (hypoxia inducible factor) [18]. Therefore, as tumors grow larger than the oxygen diffusion limit and become hypoxic, they stimulate angiogenesis to promote vascularization of the tumor tissue for the delivery of oxygen and nutrients. Furthermore, even pre-malignant lesions with intact basement membranes can develop necrosis due to inadequate oxygen supply in an avascular tumor which relies on the diffusion of oxygen and nutrients from the surrounding stroma [19]. Angiogenesis is frequently the obvious result of tumor hypoxia, and the key tumor feature to be used for detection and diagnosis in the imaging experiments described in this work.

1.4 ANGIOGENESIS

The human body possess approximately one trillion endothelial cells which line the blood vessels of every organ [20]. Healthy tissue maintains endothelial cells in a quiescent state, which is maintained, in part, by contact and signaling with pericytes and surrounding parenchymal tissue [21]. However, in response to injury or disease, endothelial cells become activated. Activated endothelial cells express adhesion molecules and growth factor receptors, proliferate, reorganize their junctional molecules to allow for migration, and can release cytokines that further enhance inflammatory and angiogenic responses [21]. Endothelial cell activation is required for angiogenesis and can

be induced by a number of disease processes, including several cytokines which are released by hypoxic tumor tissue.

Angiogenesis, the process of forming new blood vessels from existing ones, is a necessary step in wound healing and a component of some healthy physiological processes. However, during tumor formation, the pathways controlling angiogenesis become unbalanced, and a chaotic, disorganized, and dysfunctional network of tumor neovasculature is formed. These abnormal tumor vessels do not form hierarchical networks of arterioles, capillaries, and venules, and include locations of transient stasis and flow reversal. Vessel diameters are irregular, often dilated, and do not correlate to blood flow rates. The cellular structure of the endothelial cells, junctions, and associated cells such as pericytes contribute to the vascular dysfunction of tumor neovasculature, which includes leaky and tortuous vessels. [22–25]

Observations of cancer neovascularization go back to at least 1787 when John Hunter, a surgeon, coined the word "angiogenesis", which was followed by increasingly frequent descriptions of abnormal vasculature in tumors during the 19th and early 20th century [26, 27]. It was not until the middle of the 20th century that cancer angiogenesis was first recognized as a vital step for tumor growth when several researchers proposed and tested the hypothesis that tumor-derived factors served to stimulate neovascularization for tumor growth [28–31].

In the 1970s, Judah Folkman first posited that solid tumors were unable to exceed 2 mm in diameter without stimulating angiogenesis due to the inability of diffusion to supply the excessive metabolic needs of proliferating avascular tumors and suggested targeting angiogenesis as a cancer therapy [32]. Because angiogenesis is an omnipresent feature of tumor growth, it has become a popular subject of study in biology and oncology since Folkman's early publications. The balance of pro- and anti-angiogenic

molecular pathways appears to be disturbed by tumor growth, and angiogenesis is further stimulated by hypoxia induced by insufficient vascular supply of the dsyfunctional neovasculature, thus forming a positive feedback cycle [33, 34].

Sprouting is often regarded as the primary mechanism of angiogenesis. It involves the creation of a new vessel through rearrangement and proliferation of endothelial cells into stalk and tip cells. The tip and stalk cells emerge from an existing vessel into surrounding stroma and tissue in response to soluble molecular signals and chemical gradients, and sprouting terminates through anastomosis of two nearby sprouts, resulting in lumenization of the nascent vessel [35]. Intussusception is another mechanism of angiogenesis distinct from sprouting [36]. Intussusceptive angiogenesis involves the formation of transvascular pillars within the lumen of an existing vessel to split it into two lumens [37].

One of the molecules strongly related to the process of angiogenesis is vascular endothelial growth factor, or VEGF. VEGF-A was also called vascular permeability factor when it was discovered, due to its propensity to produce vascular leakage [38]. VEGF-A promotes angiogenesis by guiding sprouts, inducing proliferation in the stalk cells and directing filopodia and migration across the concentration gradient in the tip cells [39]. Signaling of angiogenesis by VEGF is primarily through the vascular endothelial growth factor receptor 2 (VEGFR2) tyrosine kinase [40].

The VEGF family is not only class of molecules involved in angiogenesis and tortuosity. It interacts with numerous other factors including hypoxia inducible factors (HIFs), angiopoietins (Ang1 and 2), endothelial nitric oxide synthase (eNOS), platelet-derived growth factor (PDGF), tumor necrosis factor (TNF-α), transforming growth factor (TGF-β), and many other molecules and pathways involved in the complex process of angiogenesis [41–43]. Ang2 facilitates sprouting by loosening the vascular smooth muscle cells and upregulating matrix metalloproteinases (MMPs) which break

down basement membrane and extracellular matrix in order to make room for sprout invasion, while Ang1 promotes vessel maturation [44]. Breakdown of the extracellular matrix can cleave several growth factors harbored in the matrix, which are then released into the interstitium, further enhancing angiogenesis. Matrix-bound growth factors include basic fibroblast growth factor (bFGF), VEGF, and insulin-like growth factor-1 (IGF-1) [35]. Placental derived growth factor (PlGF) can also contribute to angiogenesis, possibly through the recruitment of bone marrow derived endothelial progenitor cells, and due to synergistic effects with VEGF as both growth factors bind to VEGFR1, a decoy receptor for VEGFR2 [45].

Decades of research have led to the production of anti-angiogenic drugs, primarily through inhibition of vascular endothelial growth factor (VEGF) and one of its receptors, VEGFR2. However these drugs that aim to inhibit angiogenesis have been largely ineffectual, and the modest improvements in survival in a few types of cancer (such as metastatic colon cancer) do not extend survival more than a few months [46, 47]. It is clear from these clinical experiences and the disconnect between patient outcomes and pre-clinical studies in implanted tumor models that we do not fully understand the complex process of angiogenesis. Though researchers are unable to successfully control tumor angiogenesis, its pervasiveness makes it an attractive target for imaging. Furthermore, we hypothesize that the morphological abnormalities common to tumor neovasculature can be observed using acoustic angiography, thus painting a picture of microvascular structure and enabling vascular tortuosity to be quantified and utilized as an imaging biomarker.

1.5 WHY IS TUMOR VASCULATURE TORTUOUS?

Napoleone Ferrara, the first researcher to purify and clone VEGF, defined tortuosity as "The characteristic serpiginous appearance of newly formed and tumour-associated

vessels. In tumour vessels, tortuosity is believed to be a hallmark of defective structural properties." [48]. The underlying mechanism of vessel tortuosity has not been traced to a single cause, but seems instead to be related to a number of molecular and physical conditions in the tumor micro-environment. As discussed in the previous section, tumor angiogenesis is abnormal and produces disorganized and dysfunctional vasculature [49]. Structurally, tumor vessels (especially venules and veins) are dilated and tortuous, and arteriovenous anastomoses are common, resulting in abnormal flow, including transient stasis and flow reversal [23].

Vascular endothelial growth factor, or VEGF, is most commonly thought of as the driver of tumor angiogenesis and as a major cause of tortuous vasculature. Many studies describing vascular tortuosity have been performed in the retina due to the ease of fudus imaging, a non-invasive technique for visualizing retinal vasculature. Retinal tortuosity during diabetes was correlated to HbA_{1C}, and the authors attributed it to VEGF production in ischemic and hypoxic tissue, which is common in diabetes [50]. Other researchers have implanted pellets for extended release of VEGF in the vitreous humor of rabbits and primates, and observed the induction of tortuous vasculature that resembles human ischemic retinal pathologies [51,52]. VEGF production and tortuosity can also triggered indirectly, and Robinson et al. measured elevated levels of VEGF transcription and retinal tortuosity in mice following TNF-α injection [53]. Neutralizing VEGF also reduces retinal tortuosity in a rat model of oxygen-induced retinopathy [54].

Studies of tumor angiogenesis have observed a spectrum of vessel abnormalities, including tortuosity, that have been correlated to high levels of VEGF, and anti-VEGF treatment can transiently normalize vasculature, thereby decreasing tortuosity [55]. Nagy et al. attribute VEGF-A as the primary cause of tortuosity, driven by hypoxia and hypoxia-independent oncogenic pathways [56]. They attribute tortuosity to vessel lengthening combined with restrictions imposed by tissue: "Tortuosity has generally

been attributed to a restriction on lengthening, which is imposed by vessel anchoring at fixed points upstream and downstream. As a result, growing tumour vessels cannot extend linearly and so they coil." [56]. Hartnett et al. also attribute tortuosity to lengthening, though not specifically attributable to VEGF-A: "tortuosity is believed to be a form of angiogenesis through vessel lengthening" [54]. However, VEGF-C was also found to influence tortuosity because VEGF-C over-expressing tumors demonstrated a dose-dependent response in venous dilation and tortuosity [57]. Furthermore, metabolic stress (hypoxia, low pH, hypoglycemia) generated by the tumor and the immune and inflammatory response (mediated by monocytes, macrophages, platelets, mast cells, and leukocytes) can trigger angiogenesis, resulting in tortuosity, through many of the molecular pathways already mentioned [42].

In addition to the molecular factors that influence vessel morphology, the physical presence of the tumor itself may contribute to vascular tortuosity by displacement of existing vessels by the expanding tumor mass. Solid stress produced by the proliferating tumor and the extracellular matrix can produce forces strong enough to cause transient vessel collapse or stenosis [58]. Stenosis itself has also been observed to promote distal tortuosity, which is likely be caused by flow disturbances [59]. Also, leaky tumor vasculature allows plasma extravasation, which coupled with the lack of functional lymphatics, results in elevated interstitial pressure and altered trans-vascular flow patterns [60].

Tumor vasculature may also experience conditions of flow that further reinforce the development of tortuosity. Endothelial cells can sense flow, and increased shear flow is related to angiogenesis, especially the process of collateralization, and the presence or lack of flow influences vessel maturation in nascent blood vessels [41]. Studies examining flow patterns in tortuous tubes also suggest that tortuosity could be self-reinforcing. Stehbens et al. used dye injection in glass tubes of varying tortuosity to examine flow

disturbances proximal and distal to the locations of curvature and observed that flow disturbances were related to curved, tortuous segments [61].

In fluid dynamics, the Reynolds number (Re) is a dimensionless parameter that describes the ratio of inertial to viscous forces of fluid flow. Flow is considered laminar for Reynolds numbers below 2000 for steady flow in a straight tube, but Stehbens et al. observed flow disturbances at much lower Re in tortuous tubes [61]. The most highly tortuous tubes produced flow disturbances including secondary (helical) flow, backflow, and vortex shedding at the lowest Re. In animal studies with tortuous U-shaped vessels created by microvascular surgery, tears in the intima were observed [62] and endothelial damage was seen in areas of high curvature, whereas proliferative lesions were seen in locations of lower curvature [63]. Thus, tortuosity itself could produce a positive feedback loop by producing flow disturbances that alter endothelial growth and death differentially in adjacent segments of a vessel. Additionally, stenosis produced by increased mechanical stress from the tumor and ECM could also create flow disturbances and trigger a non-uniform endothelial response that could result in tortuous vessel growth. Finally, thrombosis has also been observed in tortuous vessel segments and in shear flow conditions, and thrombosis can induce capillary growth through molecular angiogenic signaling pathways [41].

Some researchers also attribute tortuosity to hypertension, but conflicting results have been reached by researchers correlating blood pressure and retinal tortuosity. A positive association between hypertension and retinal tortuosity has been observed in neonates [64] and adults [65], and is supported by observations and modeling of unconstrained elastic tubes [66]. However, retinal tortuosity was not found to be correlated with hypertension in a study of 109 monozygotic and dizygotic adult twins, and variation between individuals was more closely related to heritability [67]. Additionally, though blood pressure and tortuosity are correlated in infant retinal tortuosity in some

studies, VEGF RNA is also overespressed in infants with tortuous retinal vasculature [68]. Additionally, neutralizing VEGF has been seen to reduce retinal tortuosity in a rat model of retinopathy [54], further implicating the strong association between VEGF and vascular tortuosity in the retina, independently of any correlations found between tortuosity and increased blood pressure.

Furthermore, the possible association between hypertension and tortuosity is unlikely to extend to tumors for several reasons. First, the arterial pressure in tumors is approximately equal to that of normal tissue, whereas the venous pressure is significantly lower [23]. Thus the average blood pressure in tumors is decreased rather than increased, which should correlate with reduced tortuosity according to retinal models. Second, the material properties and microenvironment of a tumor are different from the latex tubing models [66], numerical models [69] and the retina itself. Tumors and the associated stromal cells often produce a stiffer lesion, largely due to abnormal growth and function of the extracellular matrix [70]. These factors would tend to reduce the vascular displacement (and therefore tortuosity) induced by elevated blood pressure.

1.5.1 OBSERVATIONS OF TORTUOSITY IN DISEASE

Retinal tortuosity is often seen in newborns born prematurely, and retinal hypervascularization can cause retinal detachment and blindness in this process known as retinopathy of prematurity [71]. Heneghan et al. segmented images of retinal vessels and quantified a tortuosity metric using a ratio of path length to distance between endpoints, a metric which we will call the "distance metric" in this work [72]. Retinal tortuosity is sometimes used as a surrogate marker for blood pressure [65]. In diabetes, retinal tortuosity was observed, and more prominent in venous vessels than arterial [50, 73]. However, arterial tortuosity (not venous) was more indicative of retinopathy and early nephropathy, which are 2 major causes of morbidity in type

1 diabetes patients [73]. Retinal tortuosity has also been correlated to cardiovascular disease [51, 74] and anemia [75].

Tortuosity has also been described using other imaging modalities outside of the retina. Subjective ratings of tortuosity in angiograms of intercostal arteries showed a trend of increasing tortuosity with age [76]. Subjective tortuosity assessment was also used to analyze 2-D and 3-D CT angiography, MRI, and X-ray images of head and neck vasculature in patients with Loeys-Dietz Syndrome Type 1 [77]. MRI angiography imaging of connective tissue disorders also revealed tortuosity in thoracic vertebral arteries [78]. Tortuosity of major cerebral vessels, particularly those in the neck, was found in 25% of patients with symptoms of cerebrovascular disease [59]. The authors attributed the tortuosity they observed to hypertension and arteriosclerosis. 3-D imaging in the aorta and iliac arteries was used to correlate tortuosity (both subjective ratings and computerized quantifications) to outcomes of aneurysm repair procedures [79]. Measurements of tortuosity based on calculations of curvature were derived from 3-D MRI imaging in order to model blood flow patterns in the femoral artery to predict probable locations of atherosclerosis and to explain differences in the prevalence of atherosclerosis in the superficial femoral artery in men and women [80]. Bullitt et al. observed that a healthy aging population exhibited few changes in vascular tortuosity, but that fewer resolvable vessels were visible in oder adults [81]. She and colleagues also compared cerebral tortuosity of aged individuals with varying levels of physical activity, and found that aerobic activity was correlated to lower tortuosity and higher numbers of small vessels in the brain [82].

In tumors, Bullitt et al. described patterns of tortuosity in patients with glioblastoma multiforme (GBM) [13, 83, 84]. Two of the metrics she described, the distance metric and the sum of angles metric, are also used to quantify tumor vasculature in this

work. Ultrasound imaging has also been used to observe tortuous vasculature in tumors, though not as extensively as tortuosity has been studied in the retina using optical fundus imaging. Tortuosity observed in 3-D power Doppler ultrasound was indicative of ovarian malignancy [85], and microbubble-enhanced color Doppler ultrasound made tortuous vasculature more apparent in tumors [86].

1.5.2 MEASURING TORTUOSITY

Tortuosity, a quality describing the degree of bending and twisting exhibited by a vessel, has been used to describe retinal fundus images, Doppler ultrasound, x-ray angiography, and in cerebral magnetic resonance angiography (MRA), as described in the preceding sections [13, 65, 85–90]. Early evaluations of tortuosity were subjective, visual assessments of the degree of abnormality observed in the images [75, 76, 86, 91]. Eventually, quantitative metrics describing tortuosity based on vessel length, local curvature, and locations of inflection were derived, and with the increasing prevalence of 3-D medical imaging data, 2-D tortuosity metrics were extended to 3-D [78–80, 87, 92]. However, despite the interpretive value of images displaying vascular morphology and the increasing variety of metrics describing tortuosity, few clinical standards exist for evaluating abnormal tortuosity and making diagnoses. Retinal imaging has often resulted in subjective classifications of tortuosity, or simple metrics such as the ratio of vessel length to distance between endpoints. However, Sodi et al. incorporated measurements of local curvature of the 2-D vessels including sums or products of curvature along the vessels and another, the "triangular index", based on fitting triangles [87]. Others have used curvature based metrics including sum of squared curvature along the vessel path [50].

This project will explore multiple metrics of tortuosity to determine those most

sensitive to morphological changes induced by cancer angiogenesis, as imaged by ultrasound acoustic angiography. Additionally, metrics will be combined into a multivariate model for prediction of malignancy based on the combined tortuosity of an acoustic angiography image. Cancer detection using the abnormal vascular "fingerprint" of a tumor is a novel imaging biomarker and may enable the detection of smaller lesions than currently possible. This project aims to develop estimates of the sensitivity and specificity for the detection of tumors smaller than 1 mm^3 in diameter as a step forward in the goal of early detection and improving the specificity of diagnosis

1.5.3 METRICS DEFINED

The two tortuosity metrics used throughout this work are the distance metric and the sum of angles metric. Both metrics are computed using the centerline of the vessel and do not take local vessel diameter into account. While both metrics are length invariant, consistent voxel sizing and sampling should be maintained to ensure accurate comparisons between images.

DISTANCE METRIC

The distance metric is the most commonly cited measure of general "tortuosity" in both 2-D and 3-D imaging, and simple to calculate at any scale. The distance metric is the ratio of the total path length of the vessel to the Euclidean distance between the vessel endpoints. Thus, a straight vessel has a distance metric value of 1 and increases for curved vessels as total path length increases relative to distance between endpoints. For a point, P, along the centerline of a vessel, the distance metric is defined as follows:

$$DM = \frac{\sum_{x=1}^{n-1} \|P_x - P_{x+1}\|}{\|P_x - P_n\|} \tag{1.1}$$

The distance metric is a unitless quantity since it is the ratio of two distances.

SUM OF ANGLES METRIC

The sum of angles metric, on the other hand, is computed by calculating the angle between successive trios of points along the vessel and summing them, followed by normalizing the sum of the angles by the path length of the vessel to ensure length invariance. Length invariance is preferred so that tortuosity values are not dependent on the number of points per vessel, and vessel length can be included as an additional metric in multivariate analysis if it provides useful information for discrimination between tumor and control vasculature. The angles along the centerline are computed by taking the inverse cosine of the dot product between the two unit-length vectors formed by 3 points, as follows:

$$SOAM = \frac{\sum_{x=1}^{n-3} \arccos\left(\frac{\mathbf{V_1}}{\|\mathbf{V_1}\|} \cdot \frac{\mathbf{V_2}}{\|\mathbf{V_2}\|}\right)}{\sum_{x=1}^{n-1} \|P_x - P_{x+1}\|} \tag{1.2}$$

Vectors $\mathbf{V_1}$ and $\mathbf{V_2}$ are the vectors between subsequent points along the centerline. Thus, ($\mathbf{V_1} = P_{x+1} - P_x$) and ($\mathbf{V_2} = P_{x+2} - P_{x+1}$) for n points (P) along each vessel. The sum of angles metric has units in radians per unit length.

The following chapters describe analysis of tumor vascular morphology using the distance metric and the sum of angles metric, as well as other vascular features, such as vascular density.

CHAPTER 2

CONTRAST ENHANCED ULTRASOUND IMAGING

2.1 MICROBUBBLE DEVELOPMENT

Contrast enhanced ultrasound imaging began with the development of microbubbles to enhance signals from the circulatory system in order to overcome the weak scattering by blood. Dr. Charles Joiner, a cardiologist, noticed brief ultrasound enhancement while injecting indocyanine through a catheter in the left ventricle, and it was later discovered that the source of the echoes were bubbles on the catheter tip [93]. Prior to the formulation of encapsulated microbubbles, indocyanine green and agitated saline along with other agents were used in echocardiography, often to detect shunts since the free gas bubbles were removed from circulation very quickly (after a single pass through the lungs) [94–99].

The discovery that contrast could be improved by mixing blood with the saline prior to agitation led to the development of Albunex (Molecular Biosystems, San Diego, CA), a microbubble with an air core stabilized by shell composed of human serum albumin [100,101]. Echovist (Schering AG, Berlin, Germany) was a first generation microbubble stabilized with D-galactose, but these bubbles still did not persist in circulation [93]. The agent Levovist was a successor of Echovist, and it incorporated palmitic acid to act as a surfactant to improve the longevity of the agent [93].

Second generation ultrasound agents focused on stability, and most agents switched

to cores of high molecular weight gases to slow diffusion of the gas through the microbubble shell. Polyethlyene glycol (PEG) was incorporated to prolong circulation time, minimize coalescence, and improve solubility [93]. Optison (Molecular Biosystems, San Diego, CA, currently GE Healthcare Bio-sciences, Pittsburgh, PA) contains a perfluorocarbon (PFC) core with an albumin shell, and reported stronger harmonics than Albunex, the previous albumin-encapsulated microbubble [98]. Sonovue (Bracco, Milan, Italy) consists of a phospholipid shell and a sulfur hexafluoride core, while Definity (Lantheus Medical Imaging, N. Billerica, MA) pairs a phospholipid shell with a PFC core [93]. Currently, the FDA approves of Optison and Definity for echocardiography, specifically opacification of the left ventricle. Sonovue, now known as Lumason in the United States, is approved for liver imaging in adults and children as of 2016.

2.2 MICROBUBBLE PROPERTIES

Microbubbles are blood-pool agents, confined to the circulation due to their size of approximately 1-7 μm. The shell material is thin in comparison to the microbubble size, with thickness between 10 and 200 nm [102]. Microbubbles are cleared primarily by the reticulo-endothelial system, with microbubbles retained in the liver and spleen by phagocytic cells (macrophages and specialized Kupffer cells) [103]. The core gases that diffuse into circulation are cleared by the lungs, and human pharmacokinetic studies showed that the expired half-life of sulfur hexafluoride and PFC gases was very quick, on the order of few minutes, and there was little to no detectable gas in any patients after 90-120 minutes [104, 105].

Their size also makes them resonant within the frequency range of diagnostic ultrasound (2-15 MHz), leading to high reflectivity and nonlinear echoes which enable contrast-specific imaging techniques [93]. The gas core has a high acoustic impedance

mismatch with surrounding blood and tissue due to the low density and very high compressibility of the gas core. The physical properties of microbubbles enable them to very effectively reflect ultrasound, leading to enhancement in B-mode images, but it is their compressibility that leads to unique non-linear properties that differ greatly from tissue [106]. At very low pressures, the microbubble diameter oscillates with the positive and negative cycles of the transmitted ultrasound wave. At more moderate pressures, such as 150-300 kPa (*in vivo*), microbubble expansion increases relative to the contraction, and the speed of the contractive cycle is faster than the expansive cycle, leading to the production of non-linear echoes. Higher pressures result in asymmetric expansion and microbubble fragmentation, but it is worth noting that the precise thresholds determining microbubble behavior vary with diameter and shell composition, ultrasound frequency and pulse repetition rate, as well as boundary conditions. However, the harmonics (integer multiples of the fundamental frequency), subharmonics (half the fundamental frequency), ultraharmonics (half-integer multiples of the fundamental), and superharmonics (combined higher harmonics, ultraharmonics, and non-integer frequency response) originating from microbubbles are distinct from the behavior of tissue, and thus are used to separate microbubble signals from the surrounding tissues.

2.3 CONTRAST IMAGING TECHNIQUES

Though microbubbles are useful for cardiac enhancements, microvascular imaging began once the nonlinear properties of microbubbles were realized. The higher nonlinearity of microbubbles compared to tissue in response to ultrasound makes specialized detection methods possible to distinguish contrast signal from tissue background [107, 108]. Early iterations of contrast detection relied on second harmonic imaging [109]. However, since nonlinear propagation of ultrasound through tissue can also produce harmonics which confound the harmonic contrast signal [110], contrast

specificity and the contrast-to-tissue ration (CTR) was not high. Therefore, contrast pulse sequences known as pulse inversion and amplitude modulation were developed to take advantage of microbubble nonlinearity that was not restricted to the second harmonic signal [111–115]. Subharmonic imaging (at half the frequency of the transmitted pulse) is also more specific to microbubble contrast, but tends to lack the resolution of some of the multi-pulse techniques due to the low frequencies used [116, 117]. Several encoded imaging methods have also been tailored for contrast imaging, including chirp and Golay encoding [118–121]. In recent years, ultra-fast plane wave imaging has also been extended to contrast imaging using both contrast-specific pulse schemes as well as contrast-enhanced Doppler [122, 123].

More recently, ultrasound localization microscopy, otherwise known as super resolution, has been developed to provide very high resolution vascular images. These techniques were inspired by microscopy methods which rely on the stochastic blinking of fluorophores to separate their signals and improve resolution beyond the diffraction limit [124, 125]. The first description of a similar implementation in ultrasound was by Viessmann et al. using low concentrations of contrast to detect and localize single bubbles in tubes, accumulating a sufficient number of frames to combine into an image over a long period of time [126]. This was closely followed by another group who imaged single bubbles in phantoms encased a human skull [127]. Desailly et al. then used microfluidic channels to measure resolution, and incorporated ultrafast imaging to avoid diluting contrast and acquire data more quickly, but their work was limited to *in vitro* experiments [128]. Later, Christensen-Jeffries et al. used the dilute, "single bubble" imaging technique to perform the first ultrasound super resolution imaging *in vivo*, acquiring images in a mouse ear, allowing optical verification of vessel structure and demonstrating the first *in vivo* super-resolved ultrasound images [129]. Less than

a year later, Errico et al. demonstrated the first super-resolution images using ultra-fast acquisition *in vivo*, imaging the brains of rats [130]. This year, Lin et al. applied the ultra-fast super resolution technique to image tumor vasculature, also in rats, and combining several 2D slices into a 3D projection [131].

The main disadvantages of ultrasound localization microscopy or super-resolution imaging are the long acquistions times, even with ultra-fast imaging, and computationally intense image reconstruction. Errico et al. were able to acquire almost 75,000 frames to reconstruct an image of the cortex of a rat (3.5 mm in dept depth) in 2.5 minutes, while a larger image to 11.6 mm required 10 minutes. The long imaging times make physiologic motion a problem and therefore the French group focuses their imaging on the brain because the tissue is extremely stationary when the skull is held in place with a sterotactic device [130]. Lin et al. was able to acquire a sufficient number of images for a 2D image in 26 seconds, but the total acquistion time of 3D images with 200 μm slice spacing was over 30 minutes [131].

2.4 SUPERHARMONIC IMAGING

2.4.1 IMPLEMENTATION

Superharmonic imaging of microbubbles takes advantage of the ability of microbubbles to generate broadband echoes extending several harmonics beyond the transmit frequency. This phenomenon was first exploited for imaging by de Jong, Bouakaz, and Frinking. In a conference proceedings, they published results of simulations of microbubble oscillations, varying bubble encapsulation, thermal and viscous damping, and bubble diameter [132]. With the goal of improving contrast to tissue ratios (CTR), they reported the contributions of higher harmonics, including superharmonics. They also reported the design of a phased-array transducer with interleaved elements of different center frequencies. The 96-element array consisted of 0.9 MHz (40-50%

bandwidth) elements alternating with 2.8 MHz (80% bandwidth) elements. The very low frequency transmit (below 1 MHz) was selected to minimize nonlinear propagation through tissue, a frequency dependent phenomenon [133, 134], and because their desired application is detection of myocardial perfusion. They transmitted an 800 kHz pulse with the low frequency elements and received with the high frequency elements, and results included an *in vitro* image of microbubbles in a tube and a figure reporting CTR in dB for the received RF data at different frequencies which showed a peak CTR receiving the superharmonic signals at 3 MHz. They then followed this conference proceeding with 2 full length manuscripts describing the transducer and superharmonic imaging experiments [135, 136]. In these works, they compared transmitting at 0.8 and at 1.7 MHz. They found that the maximum CTR was approximately 30 dB at the 4th and 5th harmonic levels when transmitting at 1.7 MHz, and as high as 80 dB (also at the 4th and 5th harmonics) when transmitting at 0.8 MHz. They attributed the gain in CTR to reduced frequency-dependent nonlinear propagation at lower transmit frequency. They also demonstrated the *in vivo* feasibility by imaging the heart of a pig, transmitting at 0.8 MHZ with a MI of 0.4 and receiving with the 2.8 MHz transducer and using a bandpass filter of 2.7-4.7 MHz. Further work described their interleaved transducer design in more detail and demonstrated imaging of myocardial perfusion in a pig model [137, 138].

Dr. Ferrara's group also investigated contrast superharmonic imaging, describing the transient wideband acoustic signal attributed to microbubble destruction [139]. Their early studies were *in vitro* experiments using separate transducers to transmit at 2.25 MHz and receive with a 15 MHz transducer. They selected higher frequencies than the work of Bouakaz and de Jong to improve resolution. Additional work used the same transmit and receive frequencies to enhance radiation force in a cellulose tube model of molecular imaging using biotin-avidin targeting, and to image the adherent

microbubbles [140]. Later, they developed a dual frequency array design with a 5.4 MHz linear array flanked by two 1.5 MHz arrays, which was used for *in vitro* [141] and *in vivo* experiments [142] showing improved resolution with superharmonic contrast detection and demonstrating slow-time filtering methods for separating signal from adherent and flowing microbubbles. The animal model used was FVB mice with Met-1 breast tumors implanted in the mammary pads, a model chosen for it's known phenotype of significant angiogenesis.

The Dayton lab and collaborators have also utilized dual-frequcency transducers for superharmonic contrast imaging, emphasizing high frequencies and resolution in order to enable the visualization and quantification of vascular morphology. High contrast, high resolution images are acquired in 3D in order to visualize microvasculature and to subject images to further quantification, such as the characterizations of vascular density and tortuosity described in this work. These transducers, developed in collaboration with other groups, have higher receive frequencies than previously published examples in order to maximize resolution of microvasculature, intended for the imaging of neovasculature associated with cancer and atherosclerosis (vasa vasorum). Collaboration with Dr. Stuart Foster resulted in the design of confocal, single element transducers with transmit frequencies between 2.5 MHz and 4 MHz and high frequency receive elements of 25-30 MHz [143]. These transducers have been used extensively by the Dayton lab for *in vitro* and *in vivo* studies, including the work described in this thesis [144–151]. Collaboration with Dr. Xiaoning Jiang led to the creation of several small dual-frequency transducers designed for intravascular (IVUS) and intra-cavity ultrasound imaging [152–158].

2.4.2 MICROBUBBLE PRODUCTION OF SUPERHARMONICS

Though non-linear propagation of ultrasound through tissue occurs to some extent, the production of superharmonics is microbubble specific phenomenon. While very low pressure imaging schemes are frequently used in contrast specific pulse sequences (such as pulse inversion and amplitude modulation) in order to minimize tissue artifacts and microbubble destruction, the production of superharmonics requires somewhat higher (moderate) pressures. Kruse and Ferrara attribute the production of wideband superharmonics to "high bubble wall velocity and acceleration achieved when a microbubble collapses", a theory supported by bubble modeling using the Rayleigh-Plesset equation, or to the alternate theory that shell rupture releases free gas into the fluid, resulting in "stronger oscillation of a free gas bubble compared to the damped oscillation of an encapsulated bubble" [139]. They reported that for 10 cycle pulses, pressures of 100-200 kPa were necessary to induce the production of wideband, superharmonic, transient echoes, and that higher harmonic content increased with increasing pressure. Transmitting at 0.8 MHz, Bouakaz imaged myocardial contrast at MI close to 0.4 in *in vivo* experiments in pig hearts, and related the contrast-to-tissue number to the harmonic number [135]. They reported 40 dB higher CTR than second harmonic imaging. Hu et al. used a 5.4 MHz array flanked by two 1.5 MHz arrays to compare dual-frequency imaging to fundamental [141]. They found that when transmitting and receiving at 7 MHz, the CTR did not vary with pressure, but increased significantly when transmitting at 1.5 MHz and receiving at 7 MHz. In the transmit-low/receive-high imaging scheme, the CTR increased from less than to 10 dB at 60 kPa to over 30 dB at 330 kPa. The combined findings of these studies indicated that CTR of dual-frequency imaging is dependent upon transmit pressure and that low frequency and higher pressure transmit increase the higher order harmonic echoes from microbubbles.

Lindsey et al. performed detailed experiments in order to understand the relationships between frequency (both transmitted and received), pressure, and microbubble diameter on the resulting images, specifically the CTR and resolution. He found that the resolution is primarily dictated by the receiving frequency, thus high frequency receiving transducers should be selected for imaging microvascular morphology. As reported in previous studies, the transmitted pressure influenced CTR, with CTR increasing with pressure until a threshold was reached, though the specific pressure at which this occurs varies with other factors such as frequency, microbubble attributes, and *in vitro* versus *in vivo* conditions [159]. In a subsequent publication, they reported that production of superharmonics does not rely on complete microbubble destruction, but can also be produced by gradual dissolution of a microbubble over several pulses. However the magnitude of the superharmonic signals produced by gradual dissolution (microbubble shrinking) is much weaker than that produced by microbubble destruction.

The size and composition of the microbubble contrast agents also influence the production of superharmonic echoes. Existing superharmonic imaging studies have utilized lipid shelled microbubbles (SonoVue, Definity, and similar agents), though Kruse and Ferrara report transient-like echoes from the destruction of other contrast, including rigid shelled agents [139]. However, shell rigidity should be minimized to optimize superharmonic imaging, in order to maximize the non-linear behavior of the microbubble. Rigid-shelled microbubbles are less scattering and do not exhibit nonlinear behavior, whereas unencapsulated microbubbles, on the other hand, react nonlinearly at lower pressures than encapsulated bubbles which damp the compression and expansion [132, 160].

CHAPTER 3

MATERIALS AND METHODS

3.1 ANIMAL MODELS

The majority of this project utilized a genetically engineered mouse model of breast cancer. The tumor-bearing animals were female C3(1)/Tag mice, which develop tumors spontaneously in the mammary pads. C3(1)/Tag mice are a model of basal breasts cancer in which oncogenesis is driven by the inactivation of the p53 and retinoblastoma (Rb) oncogenes by the siminan virus 40 (SV40) large T-antigen [161, 162]. Mammary carcinomas develop by 16 weeks, with abnormal ductal hyperplasia occuring earlier, mimicking the progression of breast cancer in humans. Female FVB/NJ littermates not carrying the transgene served as controls. Mice were bred and obtained from the Mouse Phase 1 Unit at the University of North Carolina at Chapel Hill, which is supported in part by the University Cancer Research Fund. For imaging, mice were anesthetized with 1-2% aerosolized isoflurane in oxygen for imaging, and hair on the ventral side was removed with clippers followed by chemical depilation to allow visualization of the caudal mammary pads. With assistance of the Animal Studies Core, a 27 gauge catheter was placed in a tail vein for injection of the contrast agent. The Animal Studies Core is supported in part by an NCI Center Core Support Grant to the UNC Lineberger Comprehensive Cancer Center.

Additional studies used a fibrosarcoma tumor model in rats. Fibrosarcoma tumors were implanted subcutaneously in the flank of Fischer 344 rats from a 1 mm piece of

fresh tissue while animals were anesthetized. Tumor material was obtained from the Dewhirst laboratory at Duke University, Durham, NC, who received their tumor tissue from the Bull laboratory at the Univeristy of Texas M.D. Anderson Cancer Center, Houston, TX. They remark that the tumor was "originally isolated from the subcutis of rats that were given the carcinogen methylcholanthrene and was maintained by serial transplantation" [163, 164]. Anesthesia was induced with 5% aerosolized isoflurane in oxygen and reduced to approximately 2% during imaging. The imaging region was depilated with clippers and chemical depilation, and a 24 gauge catheter in the tail vein provided vascular access for contrast agent injection.

Animals were supported by a heated stage to maintain body temperature during all imaging studies, and ultrasound gel was used to couple the transducer to the skin surface. All studies involving animals were reviewed and approved by the Institutional Animal Care and Use Committee at the University of North Carolina at Chapel Hill.

3.2 MICROBUBBLE CONTRAST AGENTS

Untargeted, lipid-shelled microbubbles were produced in house using a 9:1 molar mixture of DSPC (1,2-distearoyl- sn-glycero-3-phosphocholine) and DSPE-PEG2000 (1,2-distearoyl-sn- glycero-3-phosphoethanolamine- polyethylene-glycol-2000) (Avanti Polar Lipids, Alabaster, AL, USA), with 80% phosphate-buffered saline, 15% propylene glycol, and 5% glycerol. Aliquots of 1.5 ml of the lipid solution were transferred to 3 ml glass bottles, which were then sealed and capped. Headspace in the vials was replaced with decafluorobutane (Fluoromed, Round Rock, TX) and microbubbles were created via mechanical agitation with a Vialmix (Lantheus Medical Imaging, N. Billerica, MA). Microbubble size and concentration was measured with an AccuSizer 780 Single Particle Optical Sizing System (Particle Sizing Systems, Port Richey, FL). For most studies, microbubbles were diluted with sterile saline to a concentration of $5x10^9$ and infused at

a rate of 30 μL per minute using a syringe pump (Harvard Apparatus, Holliston, MA) during contrast-mode *in vivo* imaging.

3.3 IMAGE ACQUISITION

B-mode and dual-frequency images were acquired with a VisualSonics Vevo 770 system (FUJIFILM VisualSonics, Toronto, ON, Canada) using a modified RMV707 (30 MHz center frequency) or RMV710 (25 MHz center frequency) transducer. A 4 MHz annular element was added confocal to the high frequency element, with the focus at 12.7 mm (RMV707) or 15 mm (RMV710), as shown in figure 3.1. For dual-frequency superharmonic imaging, the high frequency element was disabled, and the trigger from the Vevo 770 scanner was synchronized with an arbitrary waveform generator (AFG3101 or AWG2021, Tektronix, Beaverton, OR) used to produce a single-cycle, windowed, sinusoidal waveform which was then amplified (ENI, Rochester, NY) before exciting the low frequency element [147]. Transducer output was calibrated using a needle hydrophone (HNA400, Onda, Sunnvale, CA), acquisition board (Signtec PDA14, Corona, CA), and motion stage (Newport XPS, Irvine CA) programmed in LabView (National Instruments, Austin, TX).

Typical transmit pressure used for *in vivo* imaging in this work was a peak negative pressure (PNP) of 1.2 MPa at 4 MHz, resulting in a mechanical index of 0.6. This is within the 0.8 limit listed for safe clinical use of Definity [165]. Higher harmonic echoes from microbubbles were received on the Vevo 770 system with the high frequency element, and a 15 MHz, 7th order Chebyshev high pass filter was added to the receive line (TTE, Los Angeles, CA) to further eliminate any contamination by tissue signal in the lower range of the transducer's bandwidth. The confocal elements are swept to acquire a 2-D frame, and the transducer is translated with a linear motion stage to acquire a 3-D volume. B-mode and contrast images were taken with an inter-frame

step size of 100 m and a frame rate of 4 frames per second, unless otherwise specified. In dual-frequency contrast mode, frame smoothing was used to average 2 acquisitions together to form each frame. The field of view was 2.5 by 2.5 cm in the axial and lateral dimensions, and determined by the user in the elevational direction.

Figure 3.1: This photograph shows the center high frequency element (25 MHz) surrounded by the low frequency annular element (4MHz). Both elements have curved lenses to focus them to a depth of 15 mm.

3.4 IMAGE PROCESSING

Tumor dimensions and regions of interested were determined using high-frequency B-mode images. Tumor dimensions were determined by measuring 3 orthogonal axes of the tumor in B-mode, and using the geometric mean of the axes to approximate the tumor diameter. Tumors were followed with imaging for several weeks, then removed, fixed, and embedded for histological confirmation. Therefore, accurate determination of tumor status was based on tissue imaging with high-frequency B-mode ultrasound, and tumor margins and dimensions were subjective measurements with no "gold standard" reference available. Additionally, genotype data for each mouse verified which animals were carrying the transgene and which were wild type. All transgenic animals

developed tumors over the course of the study. B-mode measurements were selected for determining tumor dimensions instead of caliper measurements due to the higher precision. Caliper measurements tended to vary by as much as a millimeter or more, possibly due to different amounts of tissue compression. Measurements from B-mode images depended on image quality and definition of the boundary based on image echogenicity, but were superior to physical measurements made with calipers.

Raw images were exported from the scanner and converted to metaheader format (.mhd/.mha) and linearly interpolated in the elevation direction to produce isotropic voxels, approximately 50 μm, for segmentation using multiscale ridge regression [166]. Using the interface designed by Drs. Bullitt and Aylward, the user is able to interactively select seed points, run the segmentation algorithm, and subsequently visualize the resulting segmentation. Segmentations were exported as text files containing the centerline of each vessel, identified by the x, y, z points in space occupied by the vessel and the radius at each point. Segmented vessel centerlines were used to calculate tortuosity in one of two ways. One way tortuosity was calculated was using Dr. Bullitt's algorithms developed for tortuosity analysis of cerebral vessels in clinical MRI angiography images [83]. This analysis has been effective at observing differences in normal vasculature and tumors in acoustic angiography imaging [144], but it includes unspecified smoothing and scaling of the vessel centerlines before calculating tortuosity. The tortuosity metrics derived from this approach were used for characterization of tumor regions of interest and spatial analysis of the extent of tortuosity around tumors, which are described in chapter 4. The second approach computes tortuosity using the same definitions of the distance metric and sum of angles metric, but by first resampling the vessel centerlines to match the image sampling (approximately 50 μm) and omitting any additional smoothing before computing the distance metric and sum of angles metric in Matlab (The Mathworks, Natick, MA), and this approach was used in chapter

6.

The distance metric is a ratio of the path length of a vessel to the Euclidean distance between vessel endpoints, and is one of the most common quantifications of "tortuosity" in the literature. The sum of angles metric is calculated by taking the sum of the angle (in radians) between 3 points along the centerline of the vessel and normalizing by path length (in mm). Thus the units of the sum of angles metric are radians per unit distance. The distance metric, on the other hand, is a dimensionless quantity that is the ratio of two lengths. For analysis of specific regions of images, such as tumors, regions of interest were segmented manually by interactively drawing polygons (using roipoly in Matlab) on individual slices of the grayscale ultrasound images and concatenating the 2D regions into a 3D segmented volume or ROI. See chapter 1, section 1.5.2 for more detailed discussion and definition of the tortuosity metrics.

3.5 STATISTICAL ANALYSIS

Data plotting was done in R, Matlab, and Microsoft Excel, but unless otherwise stated, statistical analyses were performed in R [167], and a level of $\alpha = 0.05$ was used for significance testing. Chapter 5 also includes statistical analyses and plots generated in STATA/SE 14.2 for ROC regression. Both parametric and non-parametric tests were used for significance testing, with bootstrapping in R used to estimate non-parametric distribution values when necessary. The most frequently used tests were T-test, Wilcoxon Rank-Sum, ANOVA, and Tukey Honest Significant Difference tests, and linear and logistic regression were also completed in R. Receiver operating characteristic (ROC) curves and analysis of the classification performance were performed with the pROC, ROCR, and OptimalCutpoints packages [168–170]. Clustering analysis was performed using the Density Based Statistical Clustering of Applications with Noise (DBSCAN) algorithm in R [171]. Clusters were plotted using the rgl package [172].

CHAPTER 4

CHARACTERIZING VASCULATURE IN TUMOR REGIONS

4.1 OVERVIEW

As discussed in chapter 1, tumors are known to produce abnormal vascular structures. Therefore, an imaging technique which is capable of resolving vasculature with clarity could provide useful information about tissue for characterization, detection, and diagnosis of tumors. The current ultrasound acoustic angiography technology is capable of producing high-contrast images of vasculature as small as 100-150 μm in diameter, to a depth of approximately 2 cm. This can be accomplished safely, as ultrasound does not expose the subject to any ionizing radiation and clinically approved contrast agents have a strong safety profile. This chapter is devoted to characterizing differences between tumor and normal vascular patterns that are detectable in acoustic angiography images. We will explore how tortuosity and vascular density compare in regions of tumor and healthy vasculature, as well as analyzing how the vasculature in tissue surrounding a tumor is affected by the presence of the tumor.

Previous work in the Dayton lab compared tortuosity in large fibrosarcoma tumors implanted subcutaneously to healthy vasculature in the hind limb of a rat [144]. While that work showed significant differences in tortuosity between tumors and normal hind limb vasculature using acoustic angiography for the first time, the subcutaneous fibrosarcoma is not the most clinically relevant or translatable model of tumor growth

since soft tissue sarcomas are heterogeneous and represent less than 1% of malignancies in the United States [173]. Therefore, the majority of the experiments in this work utilized a spontaneous mouse model of breast cancer, the C3(1)/Tag.

The benefit of a model in which tumors develop spontaneously (in this case driven by the inactivation of the p53 and Rb tumor suppressor genes) is that any tortuosity observed can be attributed to the tumor development process and not a wound healing response due to tumor implantation, which was one of the limitations of earlier studies. Additionally, the progression of mammary carcinomas that develop in female C3(1)/Tag mice is very similar to the stages observed in human breast neoplasms [162], making it an excellent model for the characterization of early-stage lesions. Finally, the mouse model of basal breast cancer is clinically significant because breast cancer has widespread incidence and the hormone receptor negative tumor types do not have targeted therapies and suffer from a worse prognosis. Additionally, breast cancer represents a tumor type that is somewhat superficial, which may enable the translation of acoustic angiography imaging to the clinic. Ultrasound already plays an important role in the diagnosis of breast lesions, making the development of technologies with improved diagnostic information extremely relevant.

This chapter examines the vascular morphology of tumors by using regions of interest (ROIs) to isolate tumor vasculature for comparison with normal vessels. ROIs are then expanded to explore the tortuosity of vasculature in tissue immediately surrounding a tumor. The hypotheses addressed in this chapter are:

1. Tumor vasculature is significantly more tortuous than that of normal, healthy tissue.

2. The density of vasculature within tumors is higher than in surrounding tissues.

3. The prevalence and magnitude of tortuous vasculature must decrease outside of

tumors to approach the values seen in normal tissue.

Figure 4.1 illustrates the difference between conventional B-mode imaging at a single center frequency, and the dual frequency contrast imaging technique, acoustic angiography.

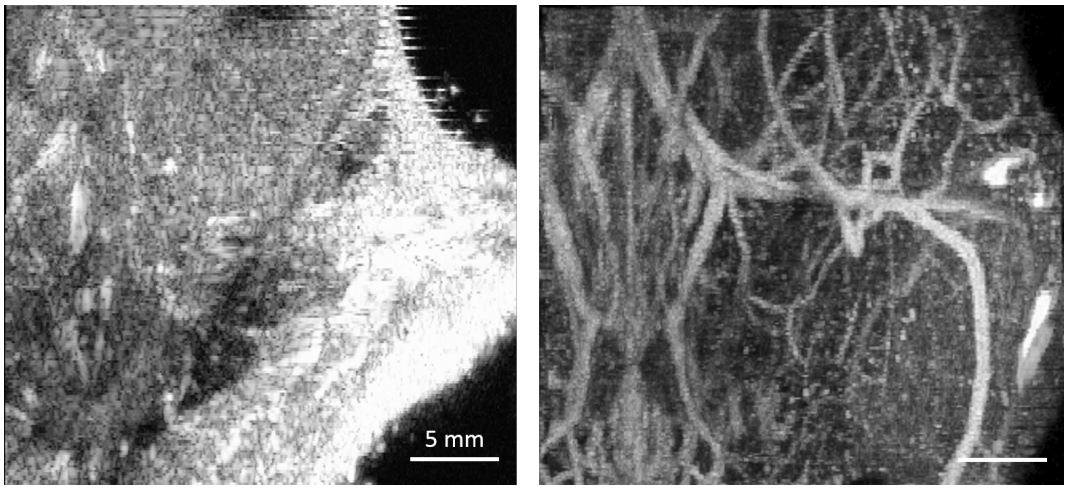

Figure 4.1: Conventional B-mode image (25 MHz) reconstructed in the coronal plane from images acquired 100 μm apart axially and the co-registered maximum intensity projection of the dual frequency vascular image acquired during microbubble infusion by transmitting at 4 MHz and receiving at 25 MHz.

Examination of the images reveals subjectively and intuitively that these hypotheses must be true, but numerical comparisons are needed in order to quantify the degree of difference between healthy and diseased vasculature and to assess the performance of the imaging technology. A few respresentative images of control and tumor images are shown in figure 4.2. These images use maximum intensity projections of the 3-D data in order to display the information in 2 dimensions. Figure 4.2 shows 2 control images and 3 tumor images, reconstructed in the coronal plane, which was orthogonal to the acquisition plane (axial). Images of the abdominal vasculature were acquired with the mice in the supine position, and the vertical axis of the images is oriented in the cranial-caudal direction, while the projected dimension is in the ventral-dorsal direction. The two control images (top row) show vessel morphology that is mostly

linear or smoothly curved. The tumor images (bottom row) show tortuosity in the vessels supplying and penetrating the tumors. The middle tumor has clearly higher vascular density that the surrounding tissue, evident by the bright contrast signal in the tumor region coming from both resolvable and sub-resolution vasculature.

The following analyses will quantify the differences in tortuosity and vascular density between controls (normal, healthy) and that of tumors in this spontaneous model of breast cancer, as well as incorporating preliminary correlations between tumor size and vascular differences, a topic which will be analyzed and discussed in more depth in chapters 5 and 6.

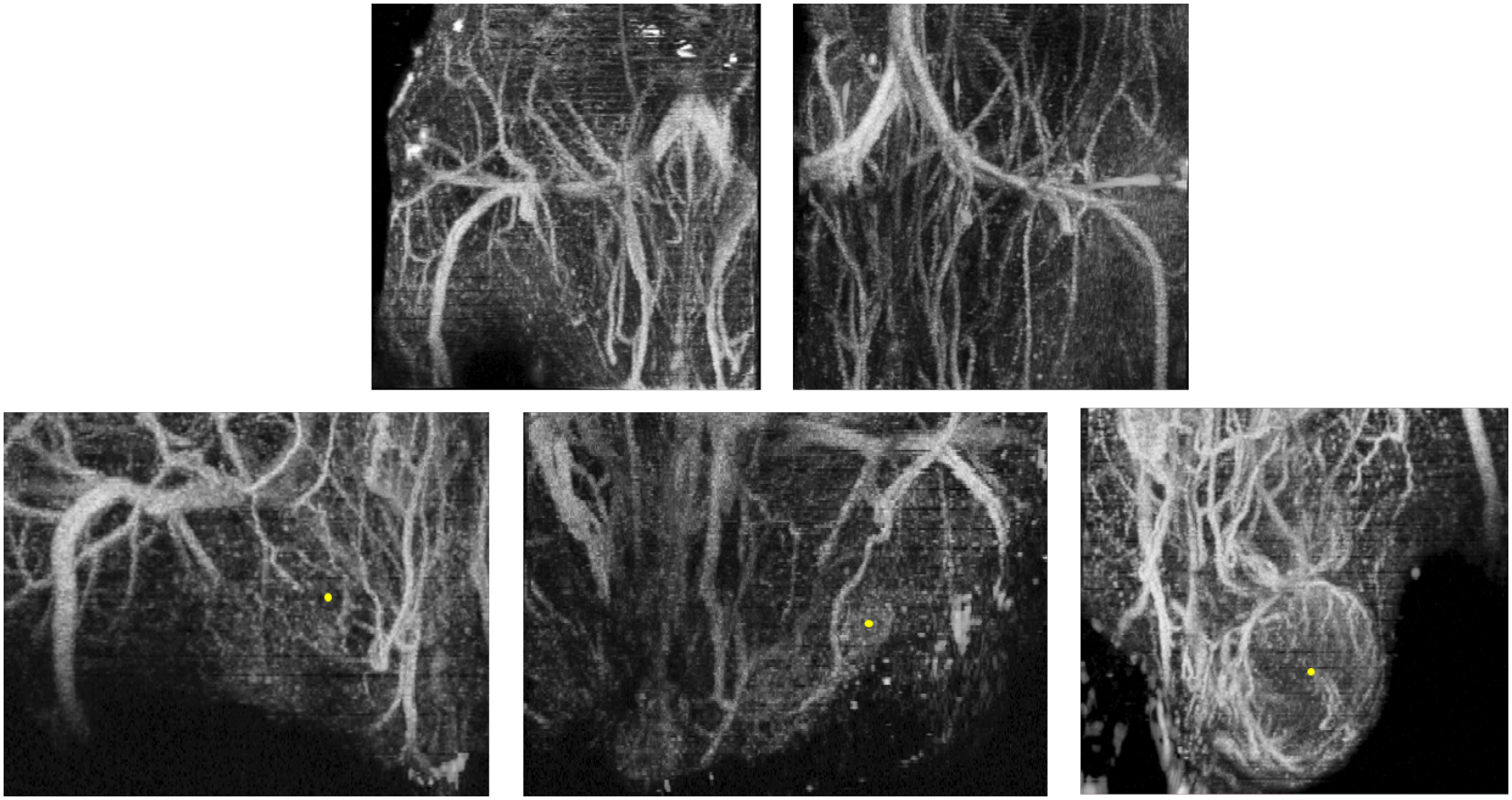

Figure 4.2: Maximum intensity projections of 3D acoustic angiography data reconstructed in the coronal plane. The top row shows two typical examples of controls, and the bottom row shows tumors with a range of sizes. The yellow dot indicates the location of each tumor, which have diameters of 1.7, 4.5, and 8.2 mm, from left to right.

4.2 TORTUOSITY ANALYSIS

The tortuosity metrics used in this chapter are the distance metric and sum of angles metric, computed using Bullitt's algorithm, and described in sections 1.5.2 and 3.4. The distance metric is the ratio of path length to distance between endpoints of a vessel and the sum of angles metric is the sum of the angles between points along the centerline and normalized by path length. The distance metric effectively captures the tortuosity of arching vessels with low spatial frequency and high amplitude oscillations, whereas the sum of angles is more sensitive to curves that vary at a high spatial frequency, but a low amplitude. Such curves appear sinusoidal or spiraling, and the local curvature along the vessel can be high without increasing the overall length of the vessel substantially. Both types of tortuosity are seen in tumor vasculature, and chapter 6 will discuss them in combination, but this chapter examines each metric independently by comparing vessels contained within tumor regions to healthy abdominal vasculature in control mice.

4.2.1 TUMOR REGIONS OF INTEREST

The vascular tortuosity of 24 tumors ranging 2.02-6.93 mm in diameter was measured using the distance metric (DM) and sum of angles metric (SOAM). The mean and standard deviation of tumor diameter was 3.74 ± 1.43 mm. Twenty control images came from the left and right sides of 10 female control mice (type FVB/NJ) that were the same age and size as the tumor-bearing mice. No ROIs were selected in the control images, so all the vasculature within the imaging field of view was segmented. Image volumes were linearly interpolated to reduce the sampling in the elevation direction from 100 μm to 50 μm. Individual vessels were segmented using Aylward's multiscale intensity ridge traversal algorithm [166], and tortuosity was calculated as described in chapters 1 and 3, using Bullitt's algorithm [83].

Vessels from the tumor ROIs and control images were pooled, and a two-sided t-test was used to test for a difference in means for each metric. Pooling vessels from every image together resulted in a total of 1,556 control vessels and 746 tumor vessels. The lower number of tumor vessels is due to the smaller total volume analyzed because tumor images were masked to include the tumor ROIs and exclude surrounding tissue in this analysis. The mean and standard deviation of the DM was 1.255 ± 0.371 for controls versus 1.431 ± 0.596 for the tumor ROIs, with $p<0.01$ for the difference between groups. The SOAM exhibited an even larger difference in means with control images having a mean value of 22.51 ± 9.45 versus 35.92 ± 13.49 for the tumor ROIs ($p<0.01$).

As an alternative to pooling the vessels from all images together, we can take the mean value of a tortuosity metric for each image or ROI, and use this mean values to represent an volume. With a single value per metric for each image or ROI, we can visualize the separation between tumors and controls. Figure 4.3 is a scatter plot of data points representing each tumor ROI or control image, with the 2 tortuosity metrics (SOAM than the DM) as the axes. This plot represents control data points with orange squares and tumor data points with blue diamonds in order to visually assess their separation. We can notice that there is some separation along the horizontal axis, representing the distance metric, but that there is much more separation between the two groups along the vertical axis, representing the sum of angles metric. This plot reveals that the magnitude of difference and class separation between tumor ROIs and controls is superior for the sum of angles metric than for the distance metric.

The mean and standard deviation of the average metrics for tumors and controls are 1.43 ± 0.11 versus 1.28 ± 0.072 for the DM and 35.68 ± 4.85 versus 21.64 ± 2.75 for the SOAM, also listed in table 4.1. The average metric is significantly higher in the tumor class for both metrics using a two-sided t-test, with $p = 9.7 \times 10^{-6}$ for the distance

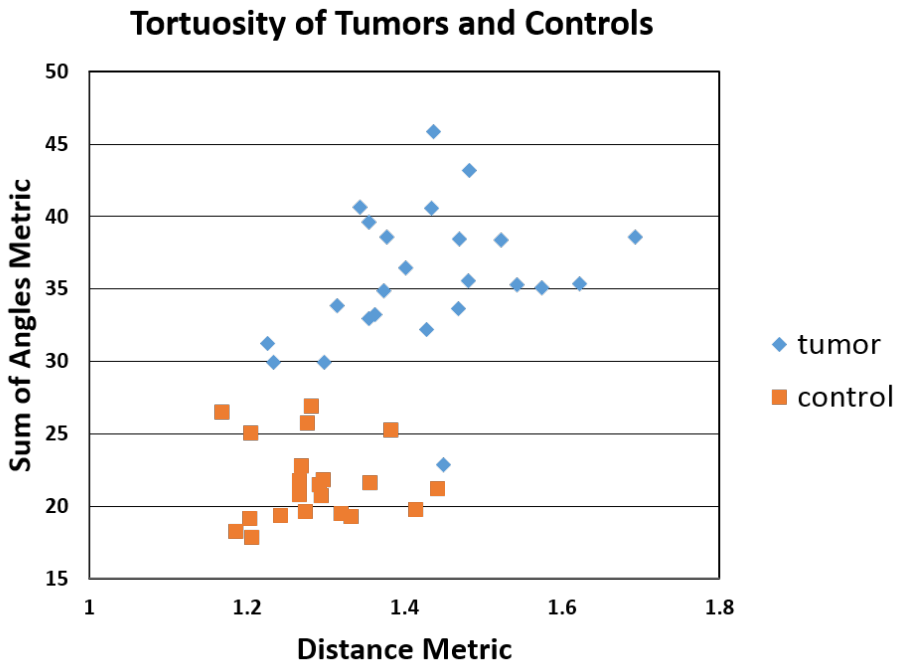

Figure 4.3: Mean distance metric and mean sum of angles metric for 24 tumor ROIs and 20 control images.

Table 4.1: Mean and standard deviation of means for the distance metric and sum of angles metric.

	DM	SOAM
Tumors	1.43 ± 0.11	35.68 ± 4.85
Controls	1.28 ± 0.072	21.64 ± 2.75

metric and $p = 1.7 \times 10^{-14}$ for the sum of angles metric. In order to compare the value of the sum of angles metric and distance metric for their power to discriminate between the tumor and control classes, we can plot receive operator characteristic (ROC) curves and compare the area under the curve (AUC) in figure 4.4.

While the mean and standard deviation for each metric show a greater difference between tumors and controls for the sum of angles metric than the distance metric, and the scatterplot in figure 4.3 also shows greater separation for the SOAM than the DM, figure 4.4 allows us to quantify the difference between the two metrics for separating tumor ROIs and controls. The area under the ROC curve indicates how well two

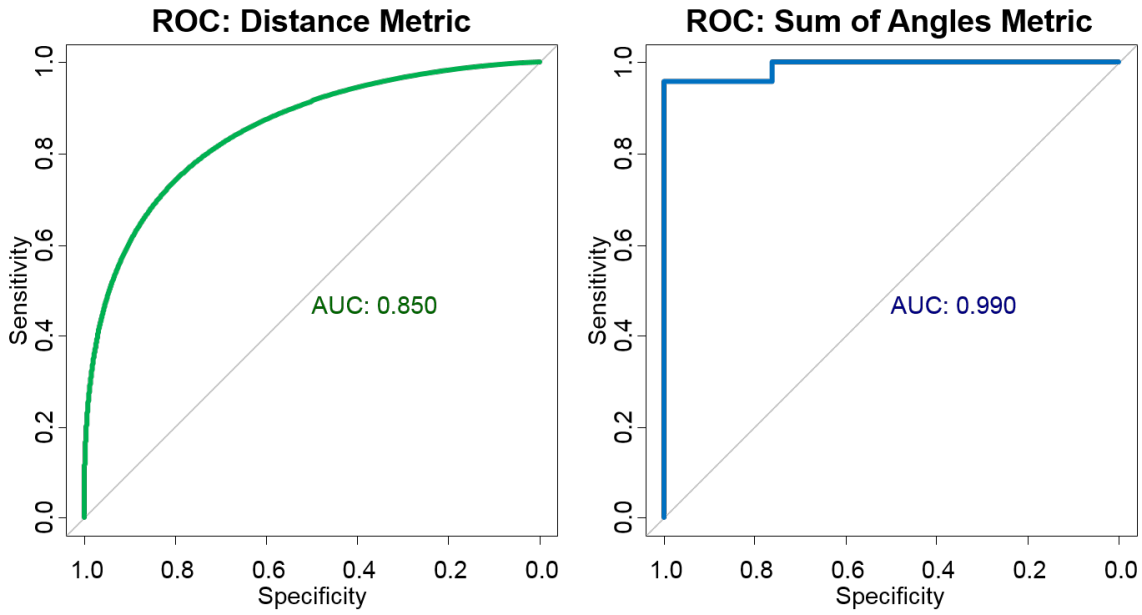

Figure 4.4: ROC curves for the distance metric (left, in green) and the sum of angles metric (right, in blue) using the mean value of each image for classification.

groups are separated using a numerical parameter. Perfect separation results in an area under the curve of 1.0 and unseparated data results in an area under the curve of 0.5, representing random guessing between the two classes. The distance metric results in an area under the curve of 0.85, indicating moderate separation between tumors and controls, but the sum of angles metric has an area under the curve of 0.99, which indicates excellent separation between tumors and controls. Weighing sensitivity and specificity equally, the optimal threshold for the distance metric is 1.34, which results in a sensitivity of 0.83 and a specificity of 0.81. For the sum of angles metric, the optimal threshold is 29.93, which results in a sensitivity of 0.96 and a specificity of 1.0. These results indicate that the sum of angles metric is a superior metric for distinguishing tumor vascular tortuosity in acoustic angiography images.

4.2.2 TORTUOSITY AND TUMOR SIZE

Though images of tumors of different sizes visually reveal that more tortuous vessels are apparent in larger tumors compared to smaller tumors (see figure 4.2), linear regression resulted in weak correlation with tumor size for both the DM and SOAM, with only the DM resulting in a statistically significant trend ($R^2 = 0.26$, $p = 0.01$), shown in figure 4.5. Linear regression between tumor diameter and the sum of angles metric resulted in $R^2 = 0.07$ and $p = 0.19$.

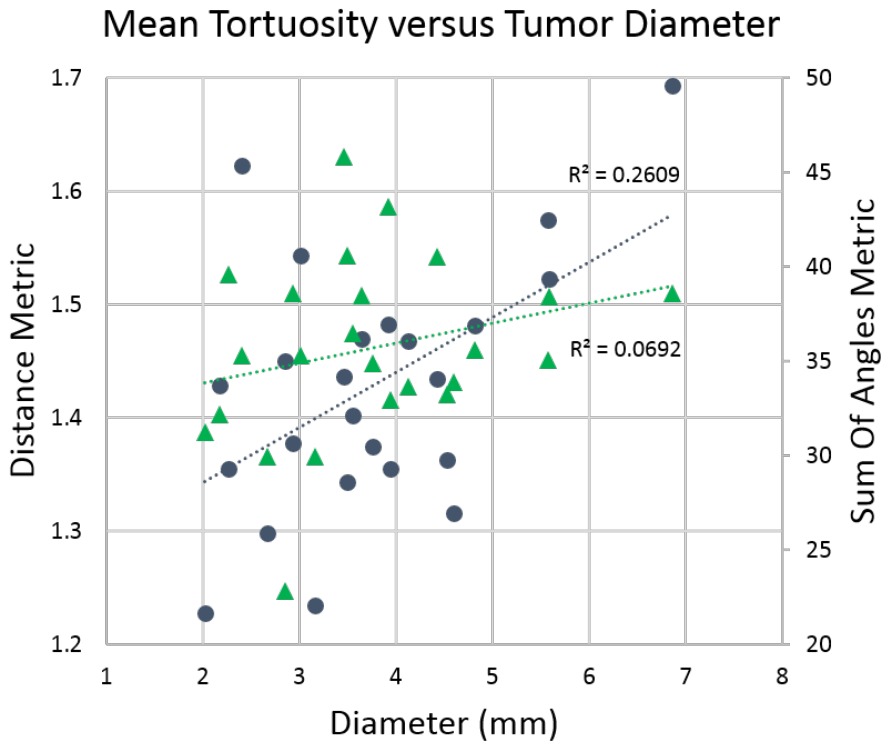

Figure 4.5: Scatterplot of the mean DM and SOAM tortuosity of 24 tumors versus the maximum tumor diameter in millimeters. The distance metric is indicated with blue circles, and the sum of angles metric is indicated with green triangles.

We can also analyze the relationship between tumor size and tortuosity by grouping the tumor data into subsets based on diameter. Tumors were classified into 1 of 3 groups based on the their largest cross section, and the resulting groups were 2-3 mm, 3-4

mm, and 4-7mm in diameter. Boxplots of tortuosity for the controls and the 3 tumor size classes show a trend of tortuosity increasing slightly with tumor size, despite poor correlation using linear regression in figure 4.5. Figure 4.6 shows the results for diameter subsets of pooled vessels and figure 4.7 shows the same data using image means instead of pooled vessels.

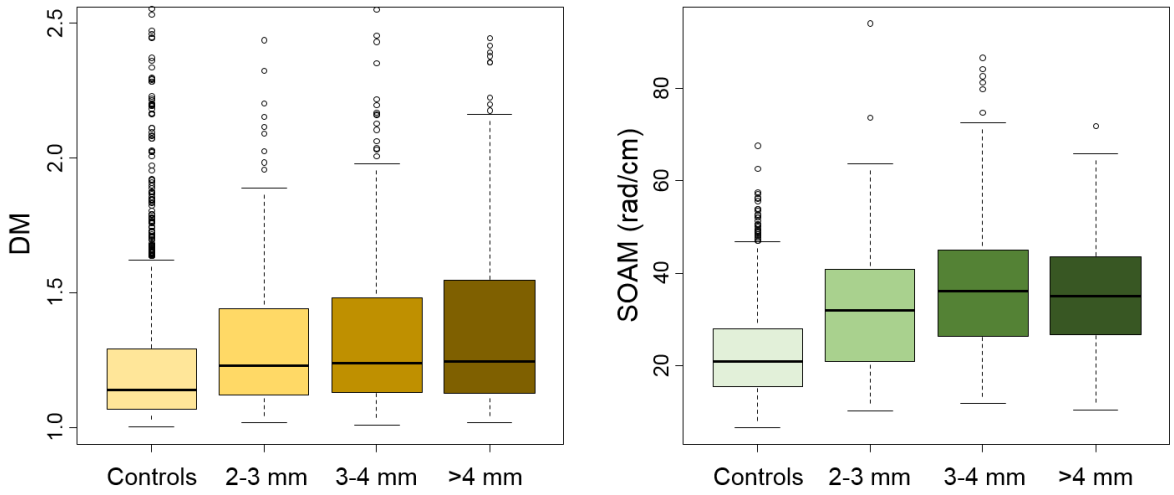

Figure 4.6: Boxplots of controls and 3 size classes of tumors showing differences in pooled vessel statistics for the distance metric (left) and sum of angles metric (right). Adapted and reprinted from Ultrasound in Medicine & Biology, Volume 41, Issue 7, Sarah E. Shelton, Yueh Z. Lee, Mike Lee, Emmanuel Cherin, F. Stuart Foster, Stephen R. Aylward, Paul A. Dayton, Quantification of Microvascular Tortuosity during Tumor Evolution Using Acoustic Angiography, Pages 1896-1904, ©2015, with permission from Elsevier.

Though the boxplots of image means in figure 4.7 show larger differences between tumor diameter sub-classes, these differences are not significant using ANOVA and Tukey Honest Significant difference tests. However, significant differences are found when making comparison to the controls. When the subset of the smallest tumors, ranging in size from 2-3 mm (n=7), were compared to controls (n=20) using t-tests, the difference between these tumor ROIs and the control images resulted in significant differences in the SOAM using either the pooled vessel or image mean statistics ($p < 0.01$). The distance metric only exhibited a significant difference using the pooled vessel

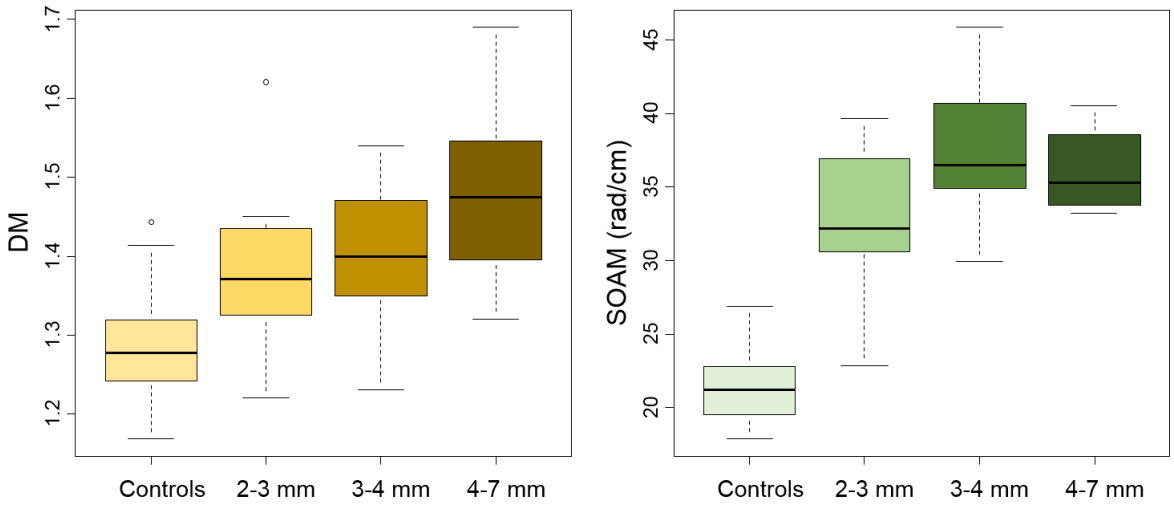

Figure 4.7: Boxplots of controls and 3 size classes of tumors showing differences in statistics of image means for the distance metric (left) and sum of angles metric (right).

vessel statistics, and the p value of the image mean statistics was low ($p = 0.07$) but not significant.

The mean and standard deviation of the DM and the SOAM for the 2-3 mm classes of tumor ROIs were 1.404 ± 0.576 and 32.89 ± 14.30, respectively using pooled vessels, and 1.39 ± 0.13 and 32.82 ± 5.7 using image means. These significantly elevated tortuosity metrics in the smallest palpable tumors only 2-3 mm in diameter lead to the question of whether smaller tumors would also be distinguishable from controls. However, the smaller tumors do not contain very many vessels for statistical analysis, and it becomes increasingly difficult to define ROIs and extract a sufficient number of vessels for meaningful statistics in tumors as the diameter decreases. Therefore, alternate approaches will be used to analyze smaller tumors without defining a ROI, detailed in chapter 6. The following section will expand the ROIs used for analysis in this section in order to explore the impact of a tumor on surrounding vasculature.

4.2.3 TORTUOSITY BEYOND THE TUMOR MARGIN

Acoustic angiography images and the analysis in the previous section have shown that blood vessels within a tumor are more tortuous than normal vasculature, but some images also show tortuous vessels outside of tumors, but they tend to be nearby and often connecting the tumor vasculature to other vascular beds. Figure 4.8 shows examples of 3 tumors with clearly tortuous vessels outside the tumor margin. This observation leads to the question of whether vascular tortuosity outside a tumor is related to proximity to the boundary.

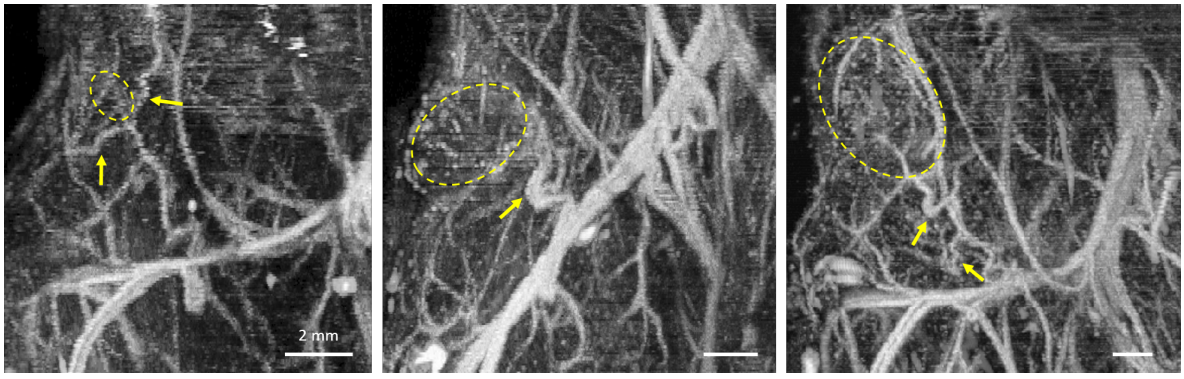

Figure 4.8: These maximum intensity projections in the coronal plane illustrate three tumors with tortuous vasculature outside of the tumor margin. The tumor locations are roughly indicated by the dashed yellow lines and the tortuous vessels that can be seen supplying these tumors are indicated by the yellow arrows. Scale bars represent 2 mm.

In order to quantify tortuosity in regions surrounding tumors and determine whether the prevalence and magnitude of tortuous vessels is related to distance from the tumor, expanding ROIs were used to capture increasing volumes of tissue around each tumor analyzed. ROIs of 10 tumors were defined by manually delineating the tumor border on each B-mode image to create a mask which was applied to the dual-frequency contrast image. In order to relate tortuosity to proximity to a tumor, the tumor ROI masks were enlarged using morphological dilation 2 mm at a time. Figure 4.9 shows renderings of vessels from increasingly large ROIs around a small tumor to illustrate the method of

ROI evolution and vessel segmentation. Each dilation of the ROI increased the radius by 2 mm, but the ROIs were not required to be spherical, so the "radius" of dilation is approximate and determined by morphological dilation on the binary ROI mask.

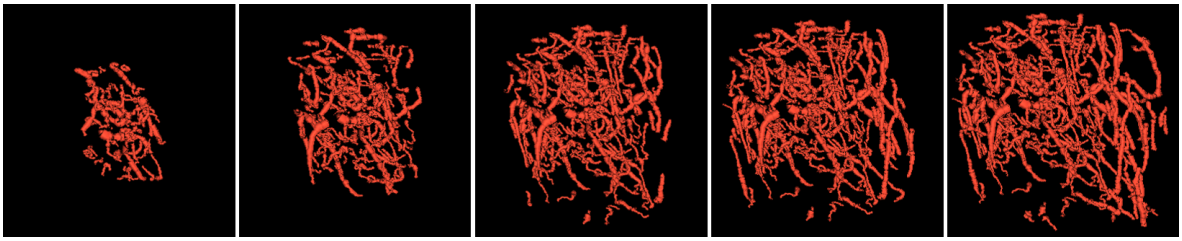

Figure 4.9: Renderings of vasculature within and surrounding a small tumor. The smallest ROI in the first panel contains the tumor and a margin of 2 mm. Then, from left to right each panel shows the result as the mask was successively enlarged by 2 mm, incorporating more of the surrounding vasculature with each subsequent dilation.

The smallest ROI in figure 4.9 contains the tumor vasculature and vessels from a margin of 2 mm around the tumor. The mean tortuosity of each ROI was regressed against distance from the tumor margin using least-squares linear regression, and the sum of angles metric was used due to its greater sensitivity to differences between tumors and controls. The analysis was also repeated for the distance metric, and the resulting trends were the same, but statistical significance and differences between groups were lower. The slope of the regression line of tortuosity and distance from the tumor margin was recorded for each image and a one sample t-test was used to verify that the mean slope was not equal to zero. Results indicated a negative correlation between distance from the tumor boundary and tortuosity (using the SOAM) with a mean slope of -0.59 and a fit of $R^2 = 0.63$ ($p = 0.002$).

Furthermore, we also compared tumor tortuosity to peri-tumoral tortuosity in adjacent tissue separated from the tumor by margin of several millimeters. The tumor group included vasculature from the manually-defined ROIs dilated by 2 mm to ensure that all vasculature on the tumor margin was included. The distal tissue group was made up of vessels contained in a concentric shell encompassing a region 6-10 mm from

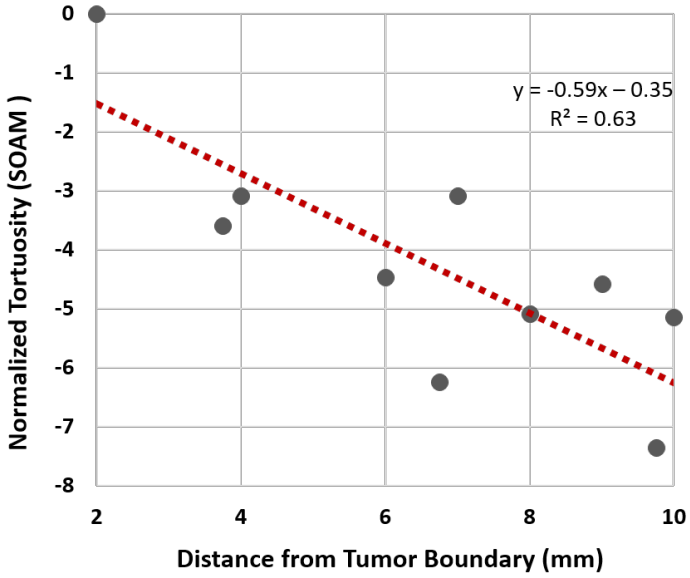

Figure 4.10: Change in the mean sum of angles tortuosity versus distance from the tumor margin.
Adapted and reprinted, with permission, from SR Rao*, SE Shelton*, PA Dayton, The 'fingerprint' of cancer extends beyond solid tumor boundaries: assessment with a novel ultrasound imaging approach, IEEE Transactions on Biomedical Engineering, Vol. 63, No. 5, p. 1082-1086 (2016).

the tumor margin. Thus, the tumor and distal regions were separated by a 4 mm buffer around the tumor. The DM and SOAM data for each group are summarized in table 4.2 and in figure 4.11.

Table 4.2: Mean and standard deviation of tortuosity in tumor, distal, and control vasculature.

	SOAM	DM
Tumor	45.49 ± 3.48	1.345 ± 0.048
Distal	39.07 ± 4.92	1.293 ± 0.042
Control	21.68 ± 2.70	1.259 ± 0.066

As expected, the tumor region possessed higher average tortuosity than the distal region and the control animals using the sum of angles metric. The mean SOAM value of the tumor group was 45.49 ± 3.48 versus 30.07 ± 4.92 in distal tissue and

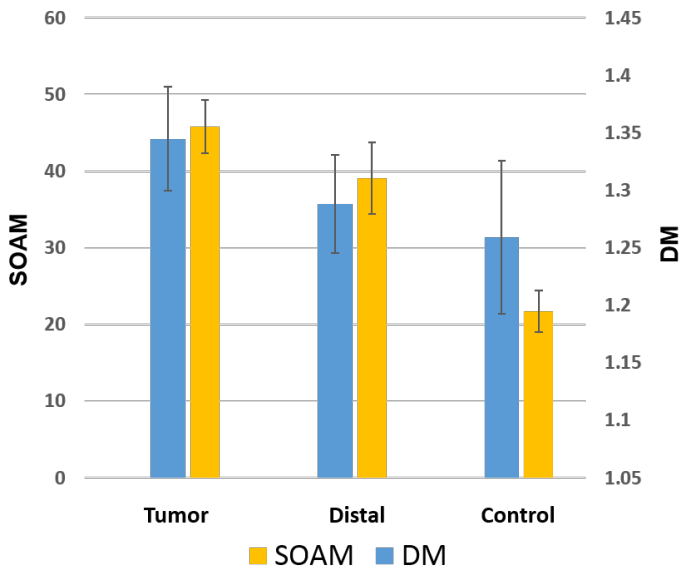

Figure 4.11: Bar plots show the mean sum of angles metric and distance metric in tumors, distal tissue surrounding tumors, and in control animals.

21.64 ± 2.75 in the control images. However, analysis using ANOVA and Tukey post-hoc tests, indicates that there are significant differences between all pairings of the 3 groups using the sum of angles metric, with $p<0.05$, and no significant differences between distal tissue and tumors or controls were observed using the distance metric. These results indicate that not only is tumor tortuosity higher than distal and control tortuosity, but the tortuosity of vasculature in tissue distal to a tumor, separated by at least 4 mm from the tumor margin, is significantly elevated relative to the tortuosity of normal vasculature in control animals. Thus, this data shows that the impact of a tumor on blood vessel morphology extends well beyond the margin of the tumor, into the surrounding tissue.

4.3 VASCULAR DENSITY

Apart from tortuosity, dense microvasculature is another prominent tumor feature that is visible in contrast imaging, including acoustic angiography. The closely-packed

neovasculature, stimulated by tumor angiogenesis, produces strong enhancement in contrast-enhanced vascular images, such as figure 4.12. This figure of a tumor almost 2 mm in diameter (visible as a hypoechoic mass indicated by the cyan marker in the B-mode image) shows closely packed vessels in the corresponding dual-frequency contrast images. In the enlarged, cropped image on the right, we see that the dense vasculature includes both resolvable vessel cross sections, as well as sub-resolution vasculature (such as capillaries) which appears as blurry regions of contrast that do not form resolvable vessel structures. Figure 4.13 shows another example of a tumor with vascular density

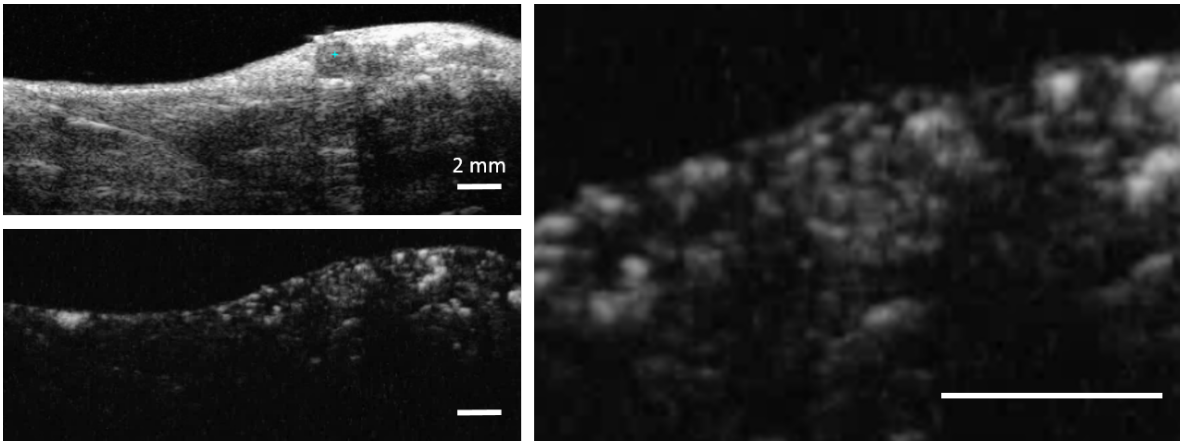

Figure 4.12: B-mode image showing a hypoechoic tumor approximately 1.8 mm in diameter and the corresponding contrast image image (2D) below with clear vascular density in the tumor region evident. The panel on the right shows an enlarged view of the tumor region with densely packed resolvable and sub-resolution vasculature apparent. All scale bars represent 2 mm.

clearly visible in the frames of acoustic angiography data. This figure shows a single tumor, indicated by the yellow crosshairs, reconstructed in the axial, saggital, and coronal planes.

Vascular density was quantified as the percent of pixels containing contrast signal, using a threshold based approach to binarize the 2D dual-frequency acoustic angiography contrast intensity images. First, a standardized threshold of 0.27, on a scale of 0 to 1, was set to eliminate low intensity voxels from noise, and to keep higher intensity

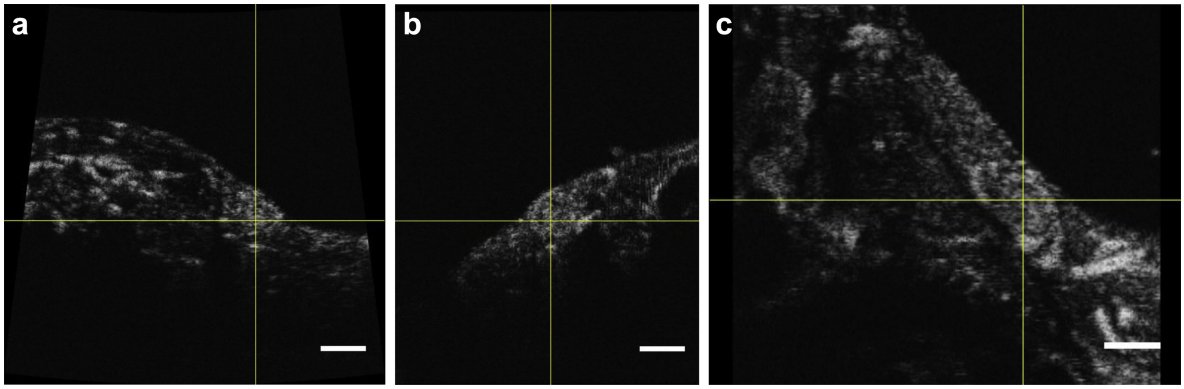

Figure 4.13: Orthogonal views (single slice) of a representative tumor in acoustic angiography: (a) axial view, (b) sagittal view, (c) coronal view (rotated 90 counterclockwise). Bars = 3 mm.
Reprinted from Ultrasound in Medicine & Biology, Volume 41, Issue 7, Sarah E. Shelton, Yueh Z. Lee, Mike Lee, Emmanuel Cherin, F. Stuart Foster, Stephen R. Aylward, Paul A. Dayton, Quantification of Microvascular Tortuosity during Tumor Evolution Using Acoustic Angiography, Pages 1896-1904, ©2015, with permission from Elsevier.

voxels, which were considered to contain contrast signal (and thus containing vasculature as well). Then the contrast images were converted to binary images based on this threshold, with contrast pixels represented by 1's and the background represented by 0's. The vascular density was calculated by taking the ratio of the number of white pixels in the binarized ROI to the total number of pixels within the ROI, and repeated for all the 2D images across the image volume. Control regions in adjacent tissue were selected by translating the tumor ROI laterally by 1.5 times the tumor diameter to a region of non-tumor tissue. The vascular density of the tumor regions was significantly higher than that of normal regions, with means of 43.8 ± 21.5 versus 19.5 ± 18.0, respectively (also listed in table 4.3). Significance testing was done using a paired t-test to compare tumor and normal regions in each animal, resulting in $p < 0.01$.

Table 4.3: Mean and standard deviations of vascular density of tumor and adjacent regions.

	Vascular Density
Tumor	43.8 ± 21.5
Adjacent	19.5 ± 18.8

4.4 DISCUSSION

This project rests on the hypothesis that the vasculature in tumors is substantially different from normal normal tissue, and that this difference can be imaged and quantified using acoustic angiography contrast-enhanced ultrasound imaging. Support for this hypothesis stems from previous work by UNC neurosurgeon Elizabeth Bullitt and work done in Dr. Paul Dayton's laboratory. Dr. Bullitt's work in MRA used the same implementation of the distance metric and sum of angles metric that has been presented in this chapter, and her work showed that glioblastoma multiforme (GBM) tumors had more tortuous vasculature than healthy the brain vasculature of healthy individuals [13,84]. The work by Bullitt and Aylward to produce efficient segmentation of tube-like objects, define 3D tortuosity metrics, and characterize tumor and normal tortuosity in the brain were invaluable for informing the design and implementation of this project. Additionally, previous work in the Dayton laboratory and collaboration with Dr. Stuart Foster's laboratory at the Sunnybrook Health Science Centre (Toronto, ON, Canada) led to the development of the confocal, dual-element transducers that were used in this work, and they also showed that superharmonic contrast imaging (acoustic angiography) could be used to measure higher average tortuosity for large, subcutaneous fibrosarcoma tumors in rats using the same metrics [143, 144]. These preceding studies have enabled the work in this thesis, which is the first demonstration of serial vascular imaging in a spontaneous tumor model (the C3(1)/Tag) and delves deeper into understanding and characterizing vascular morphology in small tumors.

Two to three millimeters is generally considered to be the limiting size for a tumor to remain avascular [32], so it is a encouraging finding that the 2-3 mm tumors imaged in this study did indeed possess significantly higher than normal tortuosity using both tortuosity metrics. Angiogenesis begins at the capillary scale, as sprouting is typically initiated in capillaries and small, post-capillary venules [174]. Acoustic angiography,

like most non-invasive, *in vivo* imaging techniques cannot resolve vasculature at this scale ($< 30\mu$m) [175, 176]. Therefore, the result that 2-3 mm tumors have elevated tortuosity compared to controls in acoustic angiography images is significant because it indicates that substantial vascular remodeling in vessels larger than 100 μm has occurred by the time tumors are 2-3 mm in diameter. Angiogenesis at the capillary scale can be inferred due to the enhanced contrast signal originating in these sub-resolution vessels (and was quantified as vascular density), but the structure of individual vessels is unknown below the resolution limit. Therefore, the results presented in this chapter reinforce the fact that cancer angiogenesis produces vascular remodeling and abnormal morphology across a wide range of scales, and is not only restricted to the capillary scale.

This chapter has described the first step toward characterizing small tumors with acoustic angiography by using ROIs to delineate different tissue of interest (tumor, adjacent, distal, etc.). The use of growing ROIs for spatial analysis revealed that abnormal tortuosity extends beyond the border of the tumor itself, into the surrounding tissue located several millimeters from the boundary of a tumor. Thus, the extent of vasculature affected by a tumor is larger than the tumor itself. The implication of this finding is that if we consider abnormal vascular structure as the target we are trying to identify in order to identify a tumor, the region of abnormal vasculature is likely to be larger than the underlying tumor, giving us a larger "target" to identify. Figure 4.14, below, shows rendered vasculature from one of the tumors included in the preceding analysis with 2 different color-maps applied. The image on the left, in blue, shows distance from the tumor, where the tumor vasculature is shown by the lightest vessels and vessels in brighter shades of blue are located further from the tumor. This colormap required selection of a tumor ROI in order to define the tumor location and measure distances relative to the tumor. Therefore, while the image clearly shows the location

of the tumor and the surrounding vasculature, it requires an individual to define the tumor location and boundary. On the other hand, the image on the right is a color map indicating each vessel's sum of angles metric tortuosity value. Vessels shown in yellow have the lowest tortuosity and brighter red vessels have higher sum of angles tortuosity. Since each vessel is color-coded based on its tortuosity metric, no user input is required beyond vessel segmentation. Despite the fact that the tumor location has not been defined in any way, the tumor is highlighted by a predominance of bright red, tortuous vasculature occurring in and around this tumor. Therefore, tortuosity may be valuable for detecting tumors, in addition to the characterizing their structure as was described in this chapter.

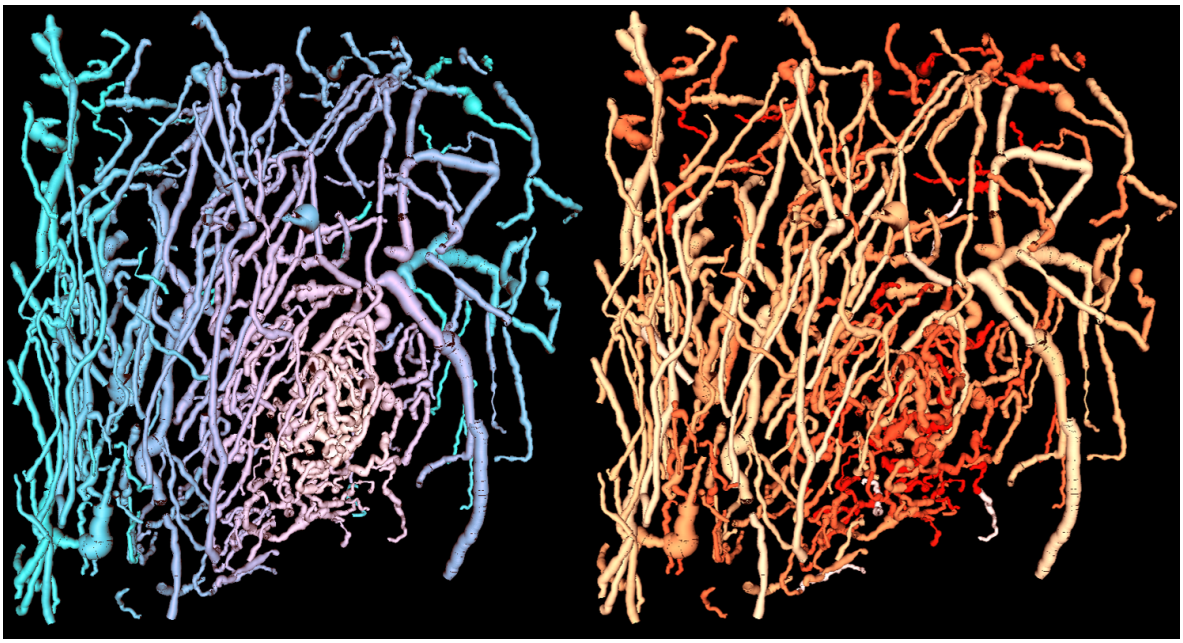

Figure 4.14: Segmented vessels are rendered and displayed in a color-map showing distance from the tumor margin (blue) and sum of angles tortuosity (red).
The panel on the right is reprinted, with permission, from SR Rao*, SE Shelton*, PA Dayton. The fingerprint of cancer extends beyond solid tumor boundaries: assessment with a novel ultrasound imaging approach. IEEE Transactions on Biomedical Engineering, Vol. 63, No. 5, p. 1082-1086 (2016).

The following chapters will build upon these findings to try to classify images as

tumor or normal without first defining a tumor location or region of interest. Instead, classification will be based upon on only the vascular structure of the tumor and surrounding tissue. Chapter 5 uses a reader study approach to test visual classification, and chapter 6 combines the tortuosity metrics described in this chapter with vascular density using a clustering approach.

CHAPTER 5

QUALITATIVE ANALYSIS OF IMAGES: A READER STUDY APPROACH

5.1 OVERVIEW

After considering the tortuosity results generated from analysis on tumor ROIs and the spatial analysis of tissue surrounding tumors described in the previous chapter 4, the remaining question is whether an entire image can be classified as containing a tumor or as a normal image from a wild-type mouse. This goal of tumor detection or binary classification is distinct from previous analysis as its goal is predictive in nature. Given an angiography image, can we determine if it contains a tumor? This is a more challenging objective than statistical descriptions and comparisons between tumor ROIs and controls because we must develop an algorithm to allow us to label an image rather than comparing two pre-labeled groups. Therefore, this classification problem was approached in two ways, using visual assessment by trained readers, and using quantitative metrics derived from the vessel segmentations. The visual assessment includes a reader study completed by 7 readers who ranked the likelihood of belonging to the tumor class on a 1-6 scale. The quantitative analysis uses clustering analysis to integrate spatial information with multiple metrics of tortuosity and is described in chapter 6. Regardless of the approach, the image classification problem is much more akin to clinical detection and diagnosis of disease. For imaging technology to become clinically relevant, it must provide useful *predicitve* information, and not be restricted

to *post hoc* comparisons between groups.

5.2 READER STUDY DESIGN

A cohort of 48 mice were used in the reader study as well as for training the quantitative classification model, a topic to be described in the following chapter (chapter 6). Tumor images came from 31 C3(1)/Tag mice and control images came from 17 FVB/NJ littermates. The animal model and imaging protocol are described more thoroughly in chapter 3. A wide range of tumor sizes was selected in order to test the hypothesis that detection is dependent on tumor size. Tumors were measured in high-frequency B-mode images and ranged in diameter from 0.78 to 8.23 mm, with a mean and standard deviation of 3.14 $\pm$ 2.16 mm. Control images came from healthy animals in the same age and weight range as the tumor-bearing animals and were randomly distributed between images of the left and right mammary pads.

Seven readers participated in the study, with variable levels of experience with contrast ultrasound imaging, from less than 1 year to over 5 years. Each of the 48 images were presented the readers in random order, from a user interface developed using Matlab (The Mathworks, Natick, MA). Readers were able to scroll through approximately 300-400 individual frames in the axial and coronal planes, and also viewed a maximum intensity projection of the image volume in the coronal plane. Each image had a red circle to direct the readers attention for making their assessment. In tumor images, the point of interest was located roughly in the center of the tumor. In control images, the point of interest was placed randomly in within the mammary pad. Placement of the red points were determined using the co-aligned B-mode images during preparation of the reader study. This methodology was adopted to recreate the anticipated clinical workflow in which a suspicious lesion might be identified via mammography and that region would then be subjected to follow-up imaging for diagnosis.

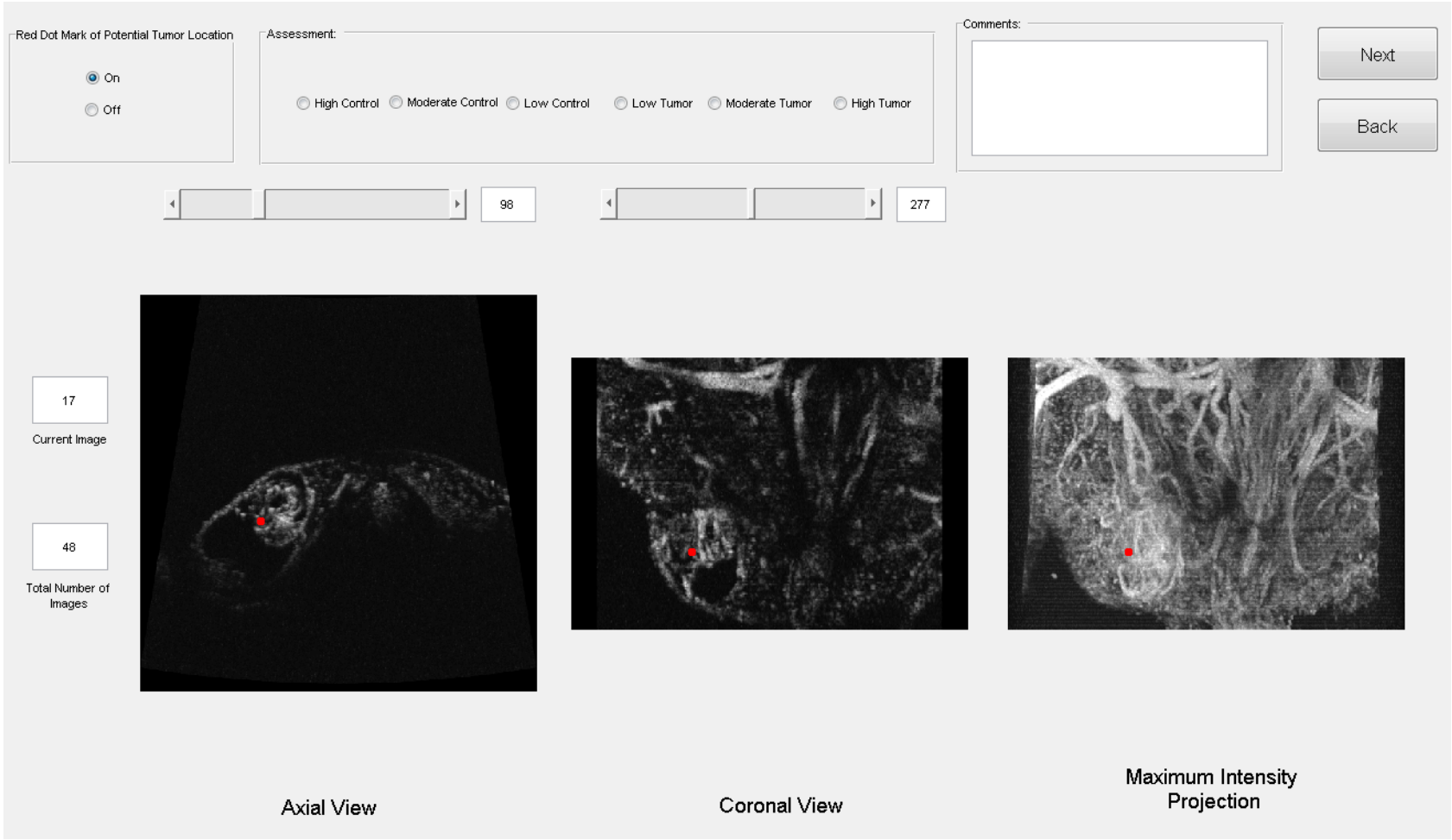

Figure 5.1: User interface for the reader study created in MATLAB. Two figures show 2D frames of the image volume and the third shows a maximum intensity projection. Readers have access to buttons for entering their assessment, navigating through the data, and showing or hiding the red dot indicating the location of interest.

Assessments were recorded as the readers progressed through the images, and most readers reported spending approximately 1.5 to 2 hours to complete their assessments for all 48 images. Image classification was based on a ordinal scale indicating the perceived image type (control or tumor) and the level of confidence (low, moderate, or high). Thus, each reader rated every image as 1 of the following 6 choices (from most likely to be normal to most likely to be a tumor):

1. high confidence of control
2. moderate confidence of control
3. low confidence of control
4. low confidence of tumor
5. moderate confidence of tumor
6. high confidence of tumor

Analysis in STATA/SE 14.2 included receiver operating characteristic (ROC) curves, area under the curve (AUC), optimal thresholds, and sensitivity, and specificity. Additionally, regression analysis was completed to determine whether tumor size influenced the sensitivity of detection as well as overall performance.

5.3 RESULTS

The area under the curve for the overall assessment of the 7 readers, considering assessments as ordinal variables, is 0.7981 with a 95% confidence interval of 0.7020-0.8941, and 0.8494 (0.8072-0.8885) if we treat the assessments as numerical rather than ordinal. The optimal cutoff is 3, with a sensitivity of 0.65 and specificity of 0.86 at this threshold, for the ordinal case. Figure 5.2; shows the overall ROC curve determined from the combined results of all 7 readers, modeling assessments as ordinals. Kendall's

coefficient of concordance takes a value of 0.778, indicating strong agreement among readers.

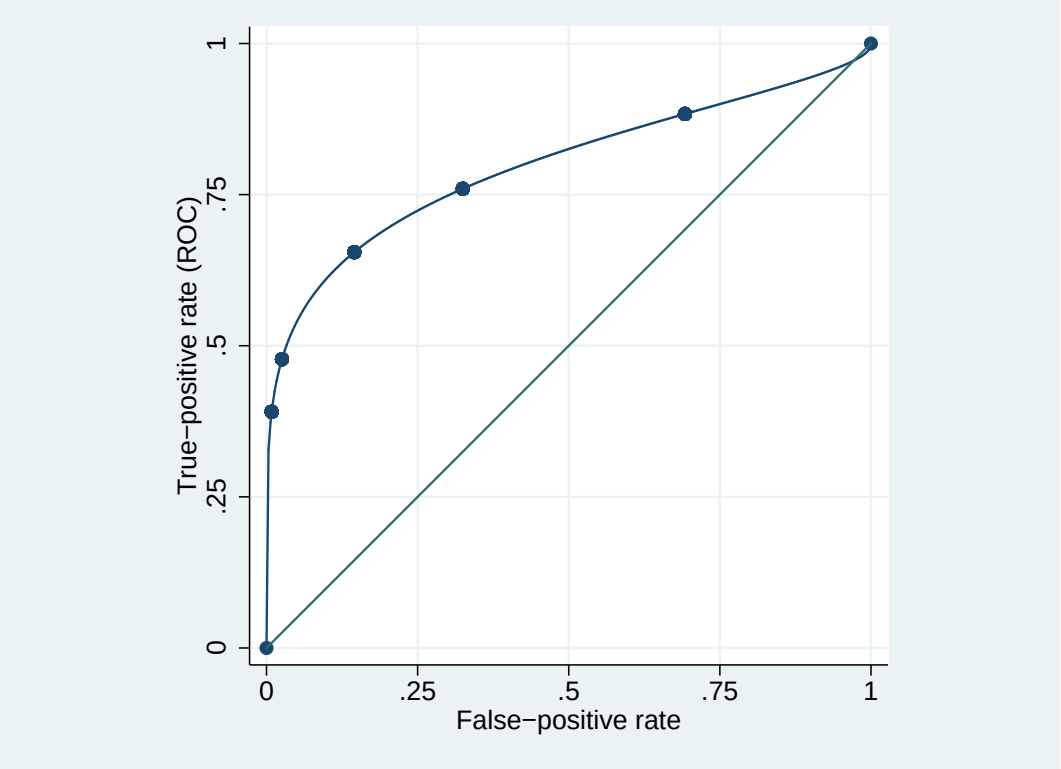

Figure 5.2: Reader study ROC curve for all 7 readers, treating assessments as ordinal variables. The resulting area under the curve is approximately 0.8.

The influence of tumor size was evaluated using ordinal ROC regression using the following regression equation [177].

$$ROC_z(p) = \Phi\left\{\sum_{k=1}^{K} R_k\alpha_{0k} + \alpha_1 \sum_{k=1}^{K} R_k\widehat{F_{0,k}^{-1}}(p) + \beta x\right\} \tag{5.1}$$

Where $\widehat{F_{0,k}^{-1}}$ is the empirical survival function with control covariates for each reader k and β is the covariate for tumor diameter.

The regression analysis using the rocreg fuction in STATA showed that there was no significant difference between reader effects, but that the tumor size parameter, β, significantly affect the ROC function, with a coefficient of 0.343 and p = 0.018. Detection

was more accurate for larger tumors, with a larger area under the ROC curve expected. Figure 5.3 show the results of the regression, in which expected ROC curves are plotted for different tumor diameters. The illustrative tumor diameters were selected based on the quartiles of the data in the reader study. The first, second (median), and third quartiles of the diameter of the 31 tumors included were 1.37 mm, 2.32 mm, and 5.09 mm. The ROC curves expected for these 3 tumor diameters are shown in figure 5.3, resulting in AUCs and 95% confidence intervals (in parentheses) of 0.67 (0.593,0.766), 0.777 (0.723, 0.860), and 0.956 (0.907, 0.997), respectively. Confidence intervals were determined using 1000 bootstrap replicates.

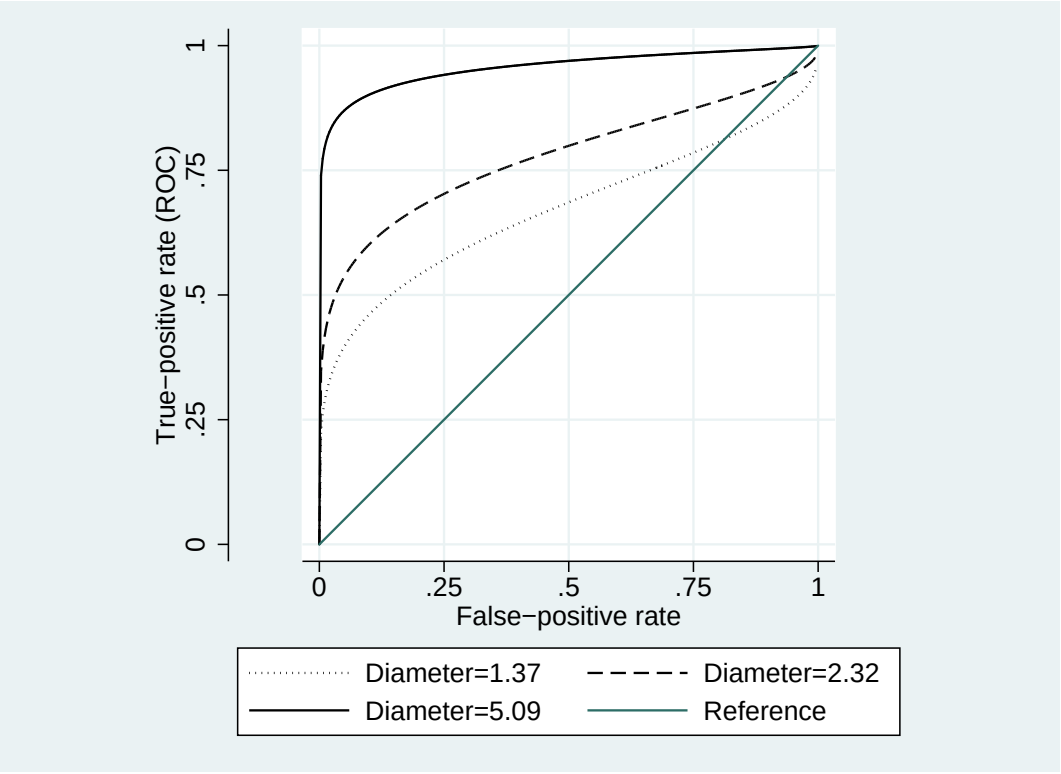

Figure 5.3: Ordinal regression of tumor diameter against ROC function resulting in a significant influence of tumor diameter on detection.

The results of regression analysis are shown in table 5.1 below, for 3 tumor sizes selected from the quartiles of the data.

For each of the 3 tumor diameter quartiles, the sensitivity values are 0.461 (0.299,

Table 5.1: Regression results for tumor size quartiles. Includes expected area under the curve, confidence intervals (CI), and sensitivity at a specificity of 0.9.

Diameter (mm)	AUC	AUC CI	Sensitivity	Sensitivity CI
1.4	0.67	(0.59-0.77)	0.46	(0.30-0.57)
2.3	0.78	(0.72-0.86)	0.60	(0.45-0.70)
5.1	0.96	(0.97-1.0)	0.90	(0.78-0.99)

0.574), 0.601 (0.454, 0.704), and 0.902 (0.776, 0.993) to achieve a fixed specificity of 0.900. We can also visualize the dependence of the reader's tumor detection on tumor diameter by plotting the average score assigned to each tumor by every reader, against the tumor diameter (figure 5.4). This figure shows that the readers' ability to detect tumors and their confidence in their assessments increased greatly for the smallest tumors to tumors up to approximately 2 mm in diameter. For tumors over 1 mm in diameter, the average reader score was over 3, and was above 3.5 for tumors larger than 2 mm in diameter. Once tumors reached 3 to 4 mm in diameter they were detected very consistently with high confidence (except for one tumor which will be examined in the discussion).

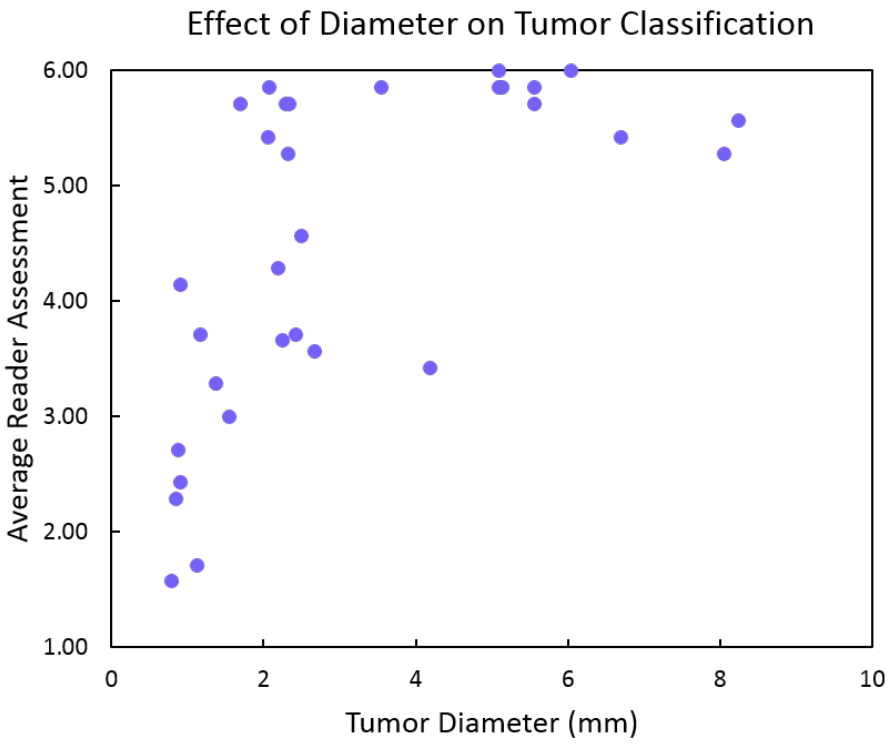

Figure 5.4: This scatterplot shows the average of all 7 readers' assessments for each tumor image plotted against the tumor diameter to show that larger tumors were detected more frequently with higher confidence.

5.4 DISCUSSION

Analysis of tumor detection using a reader study approach demonstrates the utility of qualitative visual assessment of vascular images produced with acoustic angiography superharmonic contrast imaging. Agreement between readers on an image-by-image basis was fairly high, with a concordance of W=0.778 (Kendall's coefficient of concordance). Regression analysis did not observe a statistically significant difference between readers, but the individuals with the highest accuracy tended to be those with the most experience, suggesting that increased training could improve the results of the reader study. Since acoustic angiography images are unlike other types of ultrasound or contrast images, familiarity with the modality could provide an additional advantage for

tumor detection based the images. The results of the combined assessments of all 7 readers produced an area under the ROC curve of 0.8 indicating moderately high sensitivity and specificity for the study.

Most importantly, perhaps, is the dependence of these classification outcome metrics on the size of the tumor, which was assessed in a sample of 31 tumors ranging from 0.8 mm to over 8 mm, an order of magnitude difference in diameter. Figures 5.5 and 5.6 show examples of maximum intensity projections from 3 control images and 3 tumors of different sizes. Specificity, or the true negative rate, is expected to be independent of tumor size because tumors make up the positive class. However, sensitivity (the true positive rate), or the rate at which tumors are correctly identified, was shown to be significantly dependent upon tumor size. The sensitivity and area under the ROC curve both increased with tumor diameter, according to the regression analysis described in section 5.3. For 5 mm tumors, the sensitivity and specificity were both approximately 0.9 and the area under the curve was 0.96, indicating very good discrimination between tumor and healthy. Therefore, we can expect excellent detection and discrimination of tumors 5 mm in diameter and larger using visual analysis of acoustic angiography images.

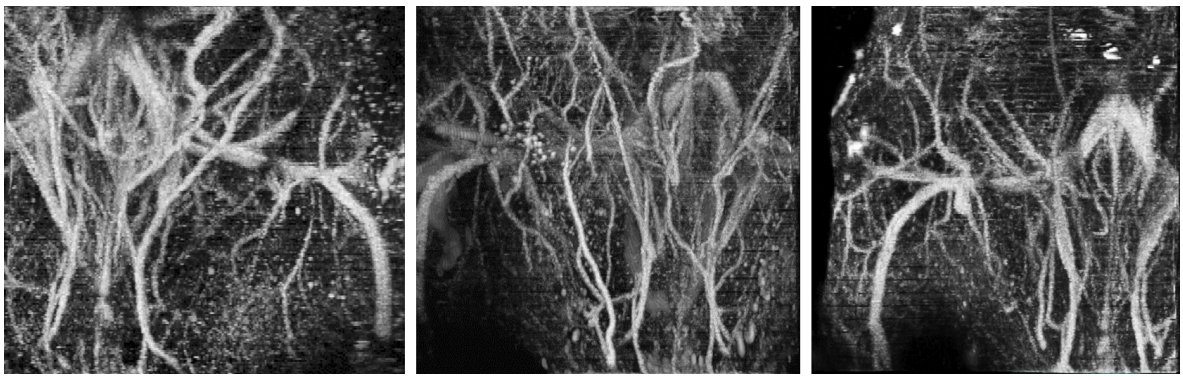

Figure 5.5: Maximum intensity projections of 3 control images, in the coronal plane.

Closer examination of figure 5.4 reveals that while there was a trend of increasing scores assigned by readers as tumor size increases, there was much more variation

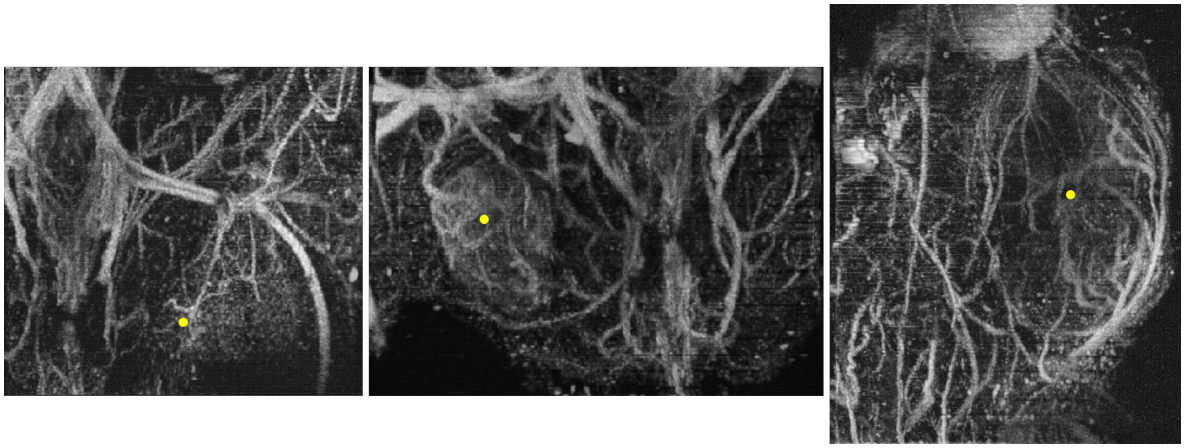

Figure 5.6: Maximum intensity projections of tumor images, in the coronal plane. From left to right, the tumors (indicated by the yellow dots) are 1.7, 5.5, and over 8 mm in diamter.

between the scores of small tumors than for larger tumors. The greatest variation in average reader assessment score occurred for tumors less than 2 mm in diameter. The average assessment ranged from 1.5 to 5.7 for these 10 tumors smaller than 2 mm. The average score for tumors less than 1 mm in diameter was 2.6, indicating that these tumors were predominately identified as controls (cases of false negatives). On the other hand, the average score of tumors only 1-2 mm in diameter jumped to 3.5, indicating much better detection and classification as tumors. Tumors 2-3 mm in diameter had an average assessment of 4.8, approaching the "moderate" confidence of tumor detection level. For tumors larger than 3 mm in diameter, the average assessment was above 5.5, indicating that the majority of these tumors were detected with high confidence.

However, there were individual tumors that did not follow the trends, making further study of them worthwhile. One example was a very small tumor with a diameter of 0.89 mm that had a high average assessment of 4.14, much higher than the other tumors smaller than 1 mm. This tumor, seen in figure 5.7, had high vascular density that made it easy to identify, especially combined with tissue distortion due to the superficiality of this tumor. Therefore, while not all small tumors were successfully identified as such,

some small tumors might be classified with high sensitivity if they exhibit markedly elevated vascular density. Throughout the study, vascular density proved to be a valuable predictive feature of tumors across all sizes, with more vascularized tumors being assessed as tumors with higher confidence overall.

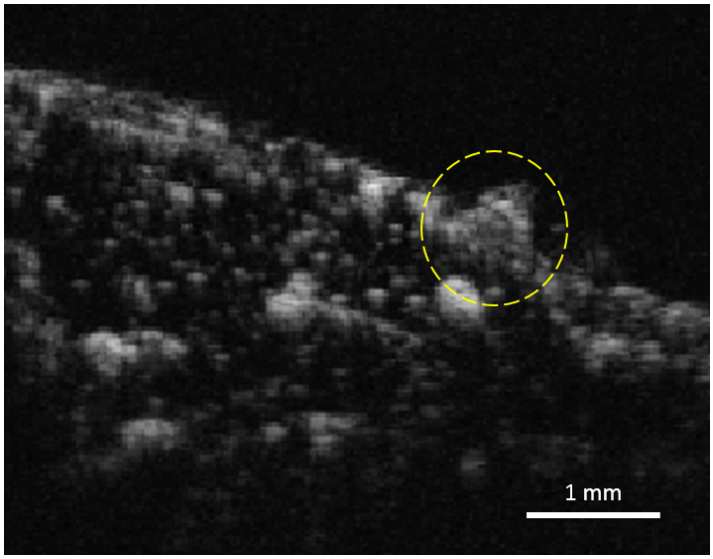

Figure 5.7: This 0.9 mm tumor had relatively high assessments for its small size, likely due to high vascular density and its superficial nature.

Readers also indicated high confidence of tumor presence when they observed tortuosity, though each reader's subjective determination of normal versus abnormal tortuosity was variable, indicating that the quantitative metrics described in chapters 1 and 4 are likely to provide additional information, and potentially more consistent classification. Imaging tortuosity in tumors requires 3D imaging to capture vascular morphology in a tissue volume, but displaying the 3D data is a challenge. This reader study used a combination of stacks of 2D image frames and interactive scrolling through the frames, alongside a maximum intensity projection of the vascular imaging data. Tortuosity can be visualized in either image format, but neither is ideal for visualizing the tortuosity of small vasculature which is common in tumors. In the maximum intensity projections large vessels are readily visible, but small vessels can often be obscured by the

amount of data that is projected through the image depth. Therefore, individual slices can make tortuous vessels more apparent if they lie within the imaging plane. Vessels oriented out of plane can be tracked visually to determine tortuosity, though this is likely to require more training and skill from the readers. Therefore, we hypothesize that including quantifications of tortuosity or 3D renderings of the vasculature will aid in the detection and diagnosis of tumors in angiography images. Chapter 6 discusses quantitative classification in detail and compares a density based statistical clustering method to the results of the reader study described in this chapter.

CHAPTER 6

QUANTITATIVE IMAGE ANALYSIS: DENSITY-BASED TORTUOSITY CLUSTERING

6.1 OVERVIEW

The goal of quantitative analysis of acoustic angiography images can be described most simply as binary classification. For each image, we want to know: "Is it a tumor?", and there two possible answers, yes or no. The objective is to use information derived from an image in order to determine which class it belongs to, based on some pre-defined rule or algorithm. The following sections will describe the use of summary statistics of tortuosity for classification, discuss their limitations, and present the justification for more sophisticated classification methods. A few examples of classification are compared, and the best performing method (clustering) will be presented in more detail.

Sections 6.3 through 6.4.3 describe quantitative analyses performed on the set of 48 images that were included in the reader study (chapter 5). This includes 17 controls and 31 tumors ranging in size from 0.78 to 8.23 mm. This data set including 48 different mice was selected as a test group, both to make comparisons to the results of the reader study and due to the wide range of tumor sizes which will enable correlations between tumor size and classifier performance. Calculations of the mean radius of each vessel, the distance metric, and sum of angles metric were performed in Matlab after resampling vessel centerlines to match the image sampling, as described in chapter 3. Additionally, the center point of each vessel was estimated in order to measure distance

between vessels in the clustering analysis.

Every image contains tens to hundreds of resolvable vessels, but each image can be summarized by taking the mean of a metric of interest. Previous studies have shown that the distance metric and sum of angles metric are higher in tumor than controls, when a region of interest (ROI) is selected, as described in chapter 4 [144,148]. However, the aim of this chapter is to explore image classification without selecting a tumor ROI that includes only a subset of vessels from the image. By eliminating *a priori* judgment of tumor presence, we can classify an image based on all the resolvable vessels without having to visually identify a tumor before analysis. The advantage of this approach is twofold. First, we eliminate the need for subjective interpretation of the location and boundary of a potential lesion, making whole-image analysis more robust than regional analysis. Second, detection of smaller tumors and determination of the detection limit will be facilitated by removing ROIs from the analysis. Very small ROIs are more difficult to define and do not contain enough vessels for reliable statistical comparison, so classification based on entire images is preferable if a method sensitive to these small tumors can be developed.

However, there are challenges inherent to using entire images for image classification, primarily due to the fraction of the image volume occupied by the tumor. Tumors do not occupy 100% of the volume of an acoustic angiography image. The population of vessels extracted from a image containing a tumor must include abnormal tumor vasculature, normal healthy vasculature from surrounding tissue, as well as a transition zone between the tumor and normal vasculature. Therefore, an image from a larger tumor will contain proportionately more "tumor vasculature" than an image with a small tumor. Furthermore, for the very small tumors we are interested in detecting (less than 2 mm), the number of vessels within a small tumor of that size is relatively few compared to the total number of vessels in the image. Thus, the mean becomes progressively less

effective at capturing tumor tortuosity in images of smaller and smaller tumors, and we expect classification based on summary statistics to be ineffective at detecting small tumors.

6.2 CLASSIFICATION USING SUMMARY STATISTICS

I calculated the mean of the distance metric, sum of angles metric, and vessel radius from all the segmented vessels in each image in the training data set. The mean and standard deviation of these image means are as follows, separated by tumor or control class, and also listed in table 6.1. Distance metric: control = 2.20 ± 2.72, tumor = 8.89 ± 22.24. Sum of angles metric: control = 3.09 ± 0.57, tumor = 3.61 ± 0.38. Radius: control = 131 ± 17 mm, tumor = 131 ± 11 mm. These metrics do not fit the normal distribution, so the non-parametric Wilcoxon rank sum test was used to test the null hypothesis that the tumor and control groups come from the same population. There is no significant difference between the average vessel radii of the two groups ($p = 0.88$), but a significant difference was observed between the 2 groups for the distance metric ($p = 0.03$) and the sum of angles metric ($p = 5.5 \times 10^{-5}$). As was discussed in the chapter describing the reader study (5), classification results are only representative of the sample of images included because sensitivity depends on the sizes of the tumors included in the sample. The results would be expected to vary if different size tumors were selected. A sample of smaller tumors would show less difference from controls, while a sample of larger tumors would show a greater difference from controls.

Table 6.1: Mean and standard deviation of tortuosity and vessel radius in tumor and control images

	DM	SOAM (rad/mm)	Average Radius (mm)
Tumor	8.89 ± 22.24	3.61 ± 0.38	131 ± 11
Control	2.20 ± 2.27	3.09 ± 0.57	131 ± 17

If we look at the performance of the mean value as a simple classifier, the area

under the receiver operating characteristic (ROC) curve with binormal smoothing is 0.682 for the distance metric and 0.824 for the sum of angles metric, as seen in figure 6.1. These values indicate that using a mean tortuosity value to represent an entire image is somewhat effective for classifying images, but perhaps could be improved by combining metrics or using data other than mean data for each image.

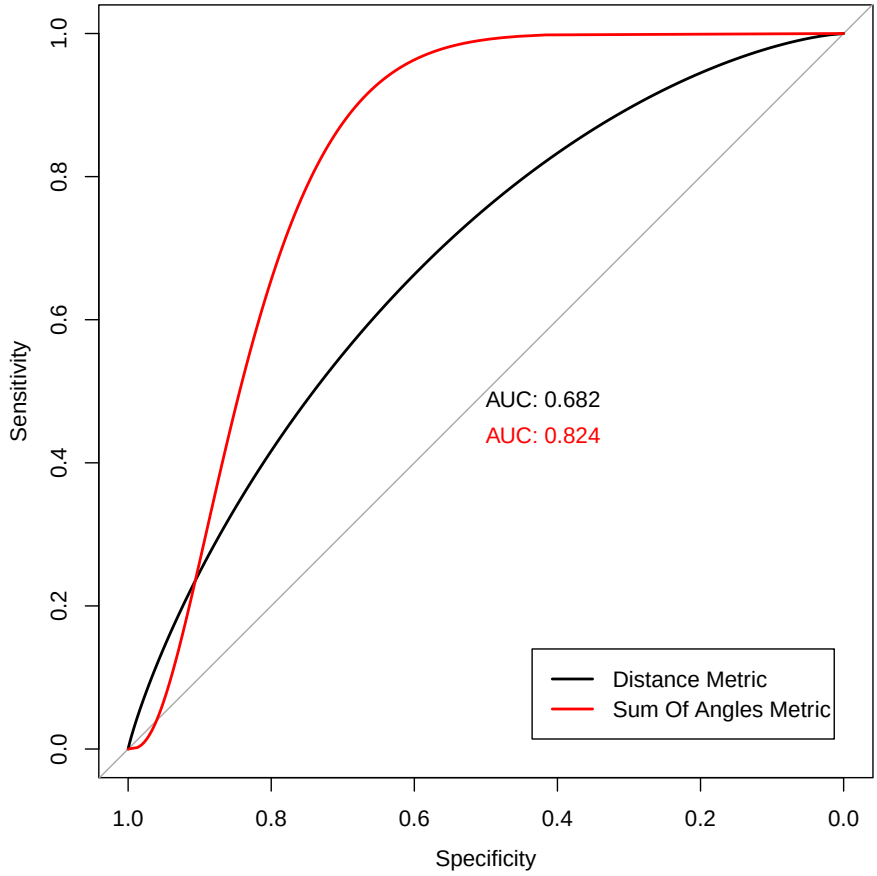

Figure 6.1: Receiver operating characteristic (ROC) curves for classifying images based on the mean distance metric or sum of angles metric.

Individual metrics are loosely correlated with one another. Tortuous tumor vessels often appear to be small caliber vessels, and indeed, the sum of angles metric is negatively correlated to vessel radius, though the correlation is weak ($R^2 = 0.1446$ and $p = 2.2 \times 10^{-16}$). Figure 6.2 shows a scatter plot of vessel radius versus the sum of

angles metric value for every vessel in the test data set. The distance metric is not significantly correlated to the vessel radius or the sum of angles metric.

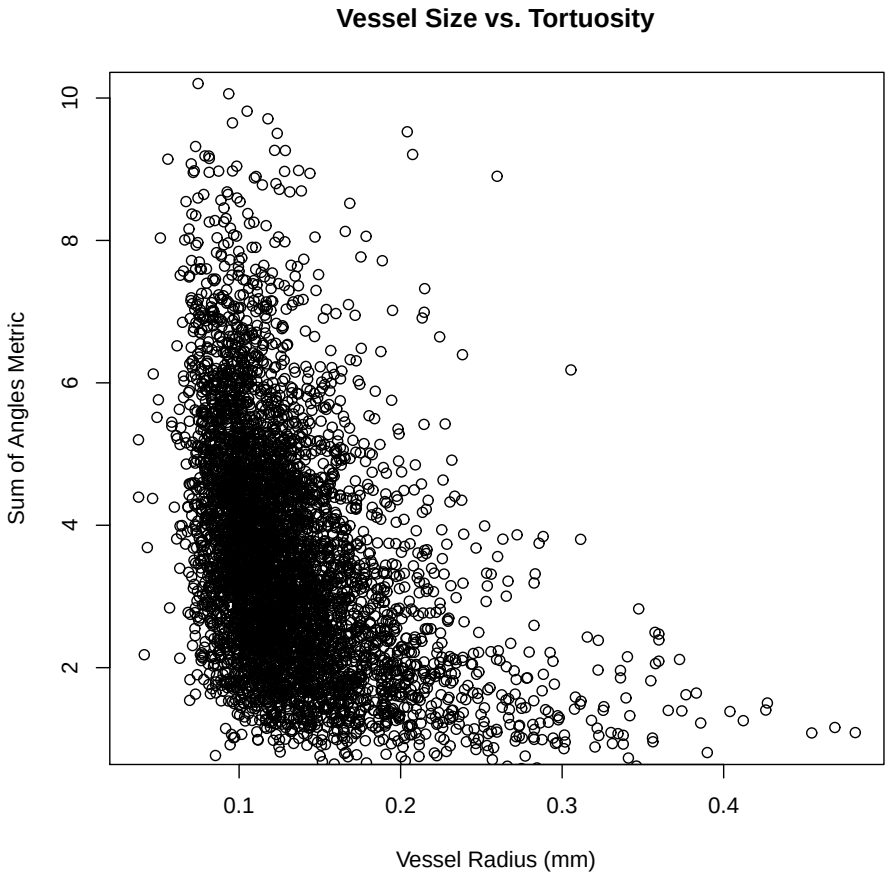

Figure 6.2: Scatter plot of average vessel radius (mm) and the sum of angles metric (radians/mm) showing a weak ($R^2 = 0.1446$) but significant correlation ($p = 2.2 \times 10^{-16}$).

6.3 MULTIVARIATE CLASSIFICATION

In order to improve upon classification based on the mean of one of the tortuosity metrics, we may be able to improve prediction by combining these metrics since they offer independent information about the images. One approach to combine the sum of angles metric, distance metric, and vessel diameter into a single metric to classify images

is a logistic regression model. Logistic regression is an extremely common method of binary classification [178]. It allows a binary dependent variable and any number of continuous, quantitative independent variables to be expressed as log-odds ratios and fitted with standard linear regression. Unlike other related techniques, logistic regression does not include the assumption of normality. Using the mean value of the sum of angles metric, distance metric, and vessel diameter for each image, a logistic regression model was fit in R. Classification using the logistic regression model resulted in an area under the ROC curve of 0.865, shown in figure 6.3. This area under the curve for the combination of sum of angles metric, distance metric, and vessel radius is superior to the performance of each individual metric, but there is little improvement in the AUC of the multivariate logistic regression (0.865) to the AUC of the best individual metric, the SOAM (0.824).

6.3.1 LIMITATIONS TO CLASSIFIERS BASED ON THE MEAN

There are two major limitations of using the mean of these metrics to represent an entire image, whether considering univariate or multivariate classification approaches. First, the distribution of these metrics are not normal. Instead all 3 parameters derived from individual vessels are right-skewed to various degrees, due to limits on the minimum value (1 for the DM, 0 for the SOAM, and approximately 0.05 mm for the radius), but effectively no limit on the maximum value. The distance metric is the most skewed of the 3 parameters, and also subject to very large outliers. These outliers can occur when a vessel segment has a loop or hook that results in the two endpoints of the vessel being very close together. Since Euclidean distance between endpoints is the denominator of the DM calculation, these types of vessels or artifacts can create influential outliers in the distance metric. Traditional outlier removal relies on interquartile ranges or standard deviation, but these are not very effective on skewed distributions

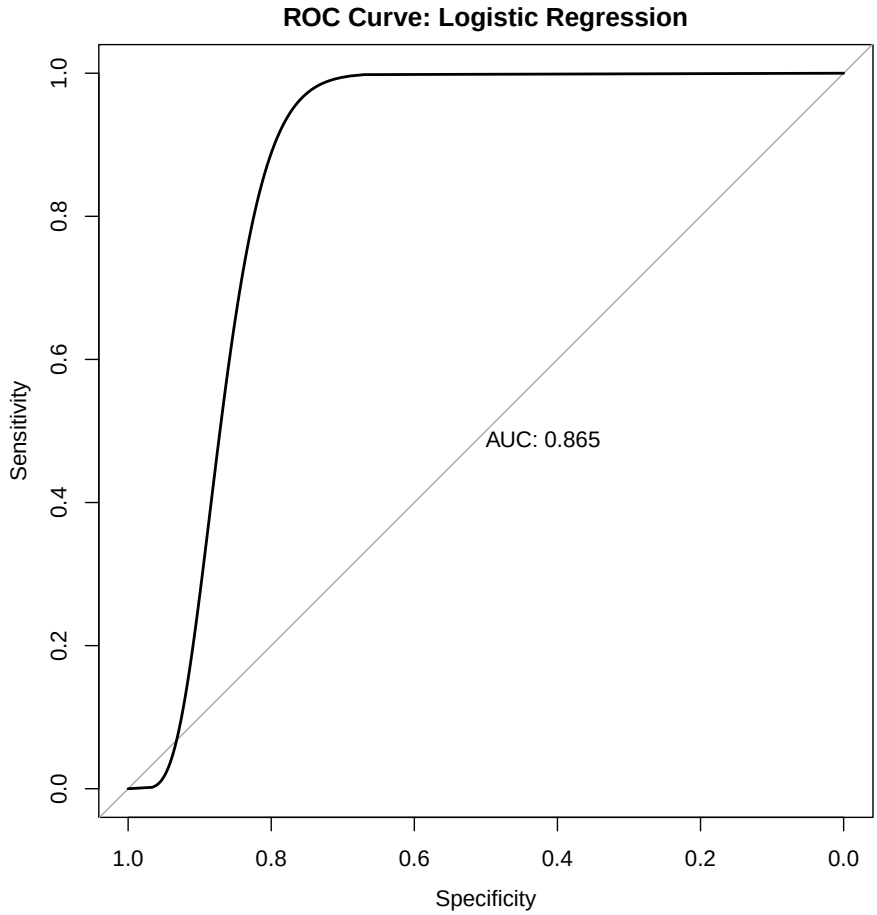

Figure 6.3: Receiver operating characteristic (ROC) curve for classifying images based on a logistic regression model incorporating the mean distance metric, sum of angles metric, and average vessel radius.

such as the distance metric. Furthermore, it is desirable for outlier removal to be based on some fixed value so that newly acquired images can be subjected to the same thresholds, rather than iteratively updating a threshold value determined by the statistical distribution of a parameter. Therefore, in previous work, we set an empirical threshold to eliminate outliers that were influencing the mean [149]. However, outlier removal also risks removing truly high tortuosity values from real tumor vessels and introduces an additional step in the analysis. Therefore, more robust classification methods that are insensitive to outliers would be beneficial. The clustering analysis described later

in this chapter was developed, in part, to avoid filtering the tortuosity data to remove outliers and to avoid statistical techniques that are sensitive to the leverage of extreme data points.

The second limitation of using the mean to represent an image is the role of tumor size, as mentioned previously in this chapter. Simply put, larger tumors will contribute a larger number of (tortuous) vessels to the total population of vessels within an image, thus pushing the image mean closer to the mean of the tumor vessels. Therefore, we seek a classification method that is sensitive to variations in tortuosity *within* an image. One approach might be to imagine each tumor image as containing 2 population of vessels, normal and tumor, which we seek to separate. However, previous work demonstrated that the vasculature outside a tumor is affected by the presence of the tumor, and the transition between "tumor" vasculature and "normal" is much more gradual rather than a sharp boundary [149]. Furthermore, it is unclear what groups would be identifiable in a normal image that lacks the "tumor" class. Any classification method that specifies the number of groups (such as k-means clustering) is likely to form arbitrary groups of vessels in a control image. Additionally, using intra-image inhomogeneity metrics or class-separation will require subsequent optimization to characterize what level of variation in the tortuosity distribution is normal and what level is indicative of disease.

The ideal image classification model is a method that allows multivariate analysis (to combine tortuosity metrics) and analyzes these parameters at the individual vessel-level rather than using statistical summaries of an entire image. Furthermore, it should be insensitive to extreme values so that outlier removal is not necessary. Another practical consideration is that the classification algorithm should use data from the full segmented image rather than requiring subdivision of the raw image followed by segmentation because segmentation is the most time-consuming step in the image analysis process.

Finally, another level of information available to us that has not been captured by

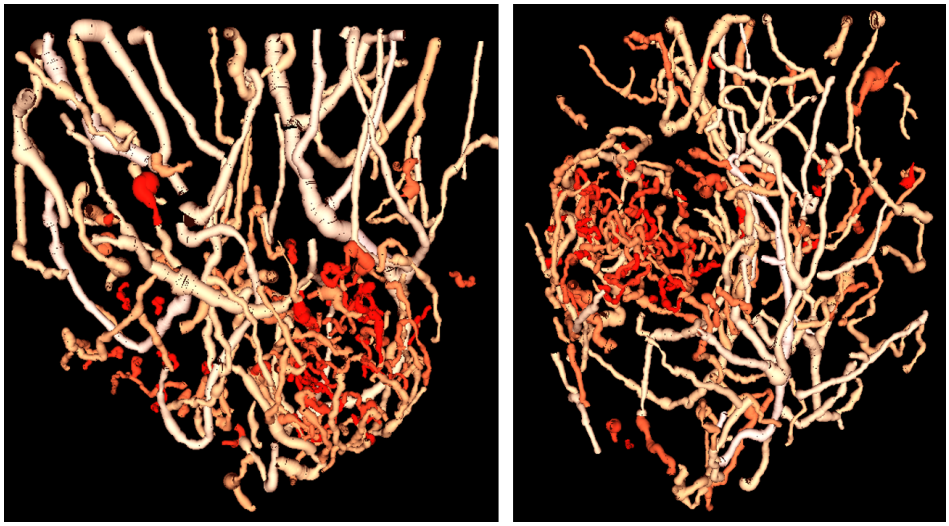

Figure 6.4: Vasculature rendered and color coded by sum of angles tortuosity metric. Brighter red indicates higher tortuosity, and the most tortuous vessels are found clustered in the tumor regions.

the single-parameter or logistic analysis is spatial relationships between vessels. Not only can we extract tortuosity and caliber from individual vessels, but also their *locations* and proximity to one another. Therefore, one approach for tumor detection and localization might be the application of a sliding window to an image in order to identify a region where the subset of vessels included in the analysis window have elevated tortuosity. However this method would be sensitive to kernel size, and thus detection will be dependent on tumor size and require iterative or adaptive changes to kernel size. Such a method will be computationally expensive, and not straightforward to implement. Furthermore, secondary classification methods will be required to determine how sub-region tortuosity values will be combined or compared in order to classify an image as normal or tumor.

Instead, a method utilizing statistical, density-based, spatial clustering is proposed. The clustering algorithm will be applied to identify groups of similarly tortuous vessels that are also located in close spatial proximity within an image. Thus, this algorithm is used to look for a closely grouped collection of unusual objects, mimicking what a

human viewer would do naturally, but using quantitative, statistical methods. The clustering method used for this analysis is called Density Based Statistical Clustering in Applications with Noise or DBSCAN [179, 180].

6.4 CLUSTERING

Clustering is a classification technique in which related observations are grouped together based on a pre-defined similarity metric. Partitional methods, such as k-means clustering, require a known number of clusters and group observations in such a way to maximize the distance between clusters [181]. Other methods base clusters on similarity rules, thus the number of clusters formed depends on the underlying data. Examples of such clustering algorithms that do not require a pre-defined number of clusters include hierarchical clustering, and the density-based clustering utilized in this work.

6.4.1 BACKGROUND

The Density Based Statistical Clustering of Applications with Noise (DBSCAN) algorithm forms clusters based on 2 parameters: the neighborhood size (eps or ϵ) and the minimum number of points (minPts) per cluster [171, 179]. Cluster points can be defined as core points or border points. A core point has at least minPts observations within the neighborhood ϵ distance from the core point. A border point is within the neighborhood ϵ of a core point, but does not have the minimum number of points within its own neighborhood. In the case of a border point that could belong to 2 different clusters, it is assigned to the first cluster formed in the data. Therefore, the DBSCAN algorithm is not deterministic and the classification of border points depends on the organization of the data set. Points that do not fit either of these criteria are classified as noise and not included in any cluster.

One major advantage of DBSCAN clustering is the insensitivity to outliers. Unlike other clustering methods that force every object to be a member of a cluster, in DBSCAN any point that is further than the pre-defined neighborhood ϵ from any cluster is labeled as noise and not grouped into a cluster. Thus, tortuosity outliers do not need to be removed in order to perform clustering classification because they will ultimately be classified as noise. This robustness in regard to outliers is an important advantage for the SOAM and DM, tortuosity metrics that tend to be right skewed instead of normally distributed, since classical outlier removal techniques based on the interquartile range or standard deviations are not appropriate.

6.4.2 CLUSTERING IMPLEMENTATION

Conventional use of clustering algorithms uses the cluster membership of a data set to derive information about the data or to compare clusters to each other [180]. Such uses may include image segmentation, where different clusters represent individual objects, or genetic and transcriptional clustering where clusters of genes may identify a disease or a molecular pathway [182–187]. However, my use of the DBSCAN algorithm is not to compare clusters within an image, but instead to produce a single metric which can be used for image classification (maximum cluster size).

The hypothesis of this approach is that control images have heterogeneous vessel patterns with any tortuous vessels that occur being distributed randomly across the image. On the other hand, images containing tumors are likely to contain a subpopulation of tortuous vessels in close proximity to one another that will be joined into a cluster. DBSCAN is a multidimensional data analysis tool, and the parameters included in this analysis were the distance metric, sum of angles metric, average radius, and the spatial location (x, y, and z coordinates) of each vessel. Thus, by setting the neighborhood parameter, ϵ appropriately, groups of tortuous vessels in tumor regions

are likely to form clusters. After performing DBSCAN clustering on all images with a fixed minimum number of points and neighborhood size, the size of the largest cluster generated for the image was used as the predictive classifier to define an individual image as a tumor or control.

Though this is an unusual use of DBSCAN classification, other researchers have used clustering results for secondary classification. Celebi et al. used DBSCAN to classify lesions and healthy skin in color images (a conventional application of clustering), but went a step farther to correlate the number of clusters generated with readers' interpretations of lesion pigment heterogeneity [188]. Thus, number of clusters was used as a secondary predictive feature in their analysis model.

DBSCAN has also been frequently used for "anomaly detection", using the noise class resulting from the classification algorithm. For example, Ren et al. used noise points (observations that do not fit into a cluster) as a method for identifying unusual network activity to guard against cyber attacks, and reported a lower false-alarm rate than another common method [189]. Another example of anomaly detection using DBSCAN clustering is by Celik et al. who used DBSCAN to detect temperature anomalies within a month of monitoring data [190]. The tortuosity clustering implementation in this project is distinct from the traditional anomaly detection approach because we make the assumption that data from healthy controls are not sufficiently similar in tortuosity across space to coalesce into clusters, and are thus classified as noise in the algorithm. Tumors, on the other hand, may have a spatially dense group of tortuous neovasculature that generate clusters in DBSCAN. This utilization, with noise considered "normal" and clusters generated indicating features of interest, may be considered the inverse of existing anomaly detection uses in which noise points are considered abnormal.

The DBSCAN algorithm requires 2 input parameters: the clustering neighborhood

Table 6.2: Maximum cluster size statistics for training data (N=31 tumors, N=17 controls).

	Mean	Standard Deviation	Minimum	Maximum
Tumor	33.84	32.76	5	135
Control	5.41	1.42	4	9

(eps) and minimum number of points per cluster (minPts). MinPts was set at 4, as suggested by Ester et al. in their paper describing the DBSCAN algorithm [179]. By setting minPts as a low value, the cluster size is dependent on the eps parameter, which I have selected by optimizing the area under the ROC curve for the training data described here. In general, the smaller the neighborhood parameter, the fewer points are included in clusters, and the more points are classified as noise. DBSCAN clustering was performed on the 48 training images with minPts = 4 and a range of values of eps tested, from 20 to 40. The best discrimination between tumors and controls (as measured by the ROC AUC) was with eps = 27, which corresponds to a neighborhood of 1.35 mm in physical space.

6.4.3 TRAINING DATA RESULTS

DBSCAN clustering with numPts=4 and eps=27 was completed on each of the 48 images in the training data set, and the number of vessels in the largest cluster generated was used as the classification parameter. The mean and standard deviation of the maximum cluster size in the tumor images was 33.84 ± 32.76, with values ranging from 5 to 135 vessels per cluster. On the other hand, the control class had a much lower mean of 5.41 ± 1.42, and a smaller range of 4 to 9 vessels per cluster. Figure 6.5 shows boxplots comparing the maximum cluster size in both image types and table 6.2 lists the mean and standard deviation. There is a signficant difference between the cluster size in these two groups using a two-sided t-test ($p = 3.8 \times 10^{-5}$).

Clustering resulted in an area under the curve of 0.95, shown in figure 6.6 with

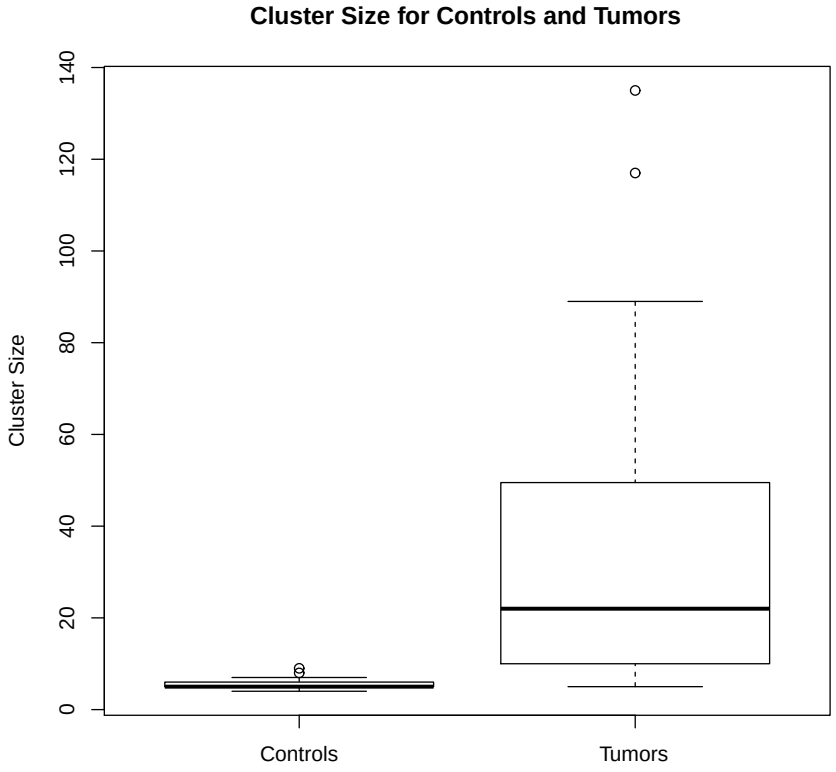

Figure 6.5: Tukey boxplots of the maximum cluster size generated with DBSCAN for control and tumor classes.

binormal smoothing applied. Weighing sensitivity and specificity equally, the optimal cutoff is a maximum cluster size of 8 vessels per cluster. This results in a sensitivity of 0.871 with a 95% confidence interval of 0.677 to 1.0 and a specificity of 0.941 with a 95% confidence interval of 0.765 to 1.0. Confidence intervals were computed using 2000 bootstrap replicates.

There were a significantly higher number of vessels segmented from tumor images than from control images, with $p = 9.9 \times 10^{-5}$). Therefore, one potential confounding variable is the number of vessels per image, possibly resulting in larger clusters from images with a higher number of segmented vessels. To address this concern, the number of vessels segmented was plotted against the maximum cluster size for each image type

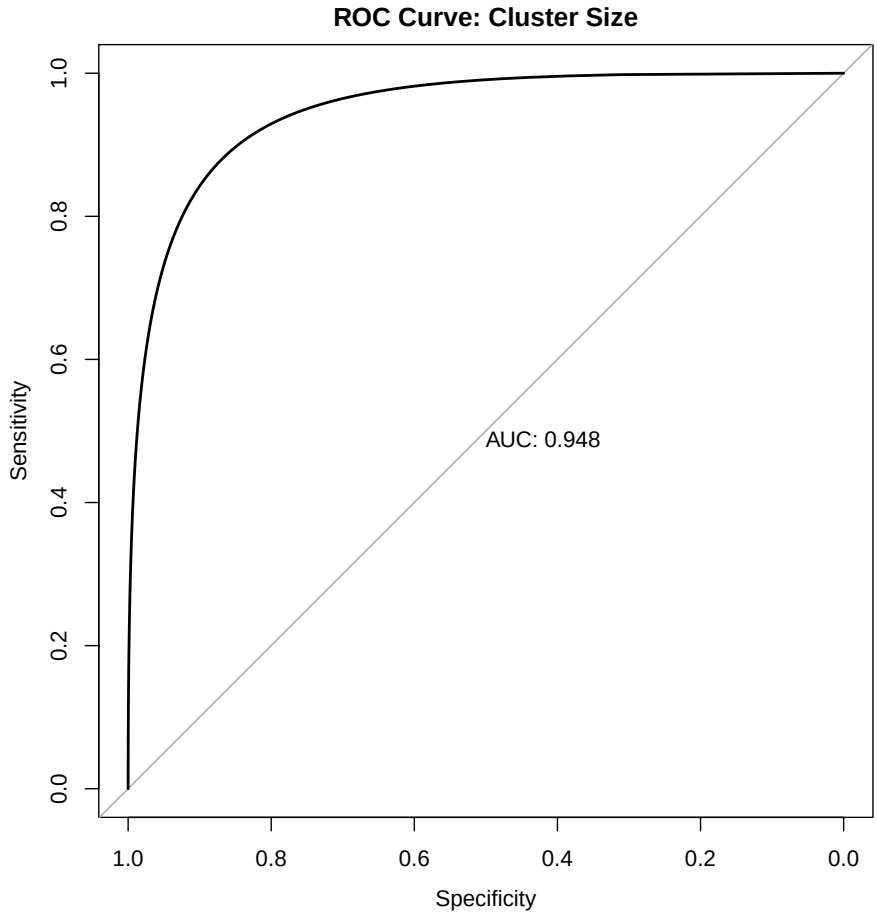

Figure 6.6: Receiver operating characteristic curve for image classification with the density based statistical clustering in applications with noise algorithm.

to see if the differences in maximum cluster size can be related to number of vessels segmented. What we notice in figure 6.7 is that while cluster size does tend to increase with the total number of vessels segmented, this phenomenon is only evident in the tumor class. The controls vary from approximately 100-180 vessels segmented per image, and show no discernible correlation between the number of vessels segmented and the maximum cluster size generated with DBSCAN. On the other hand, for the tumor class, some of the images with the largest clusters also have the highest number of vessels segmented. This suggests that the high vascular density observed in tumors positively influences cluster aggregation in the tumor regions of the tumor images.

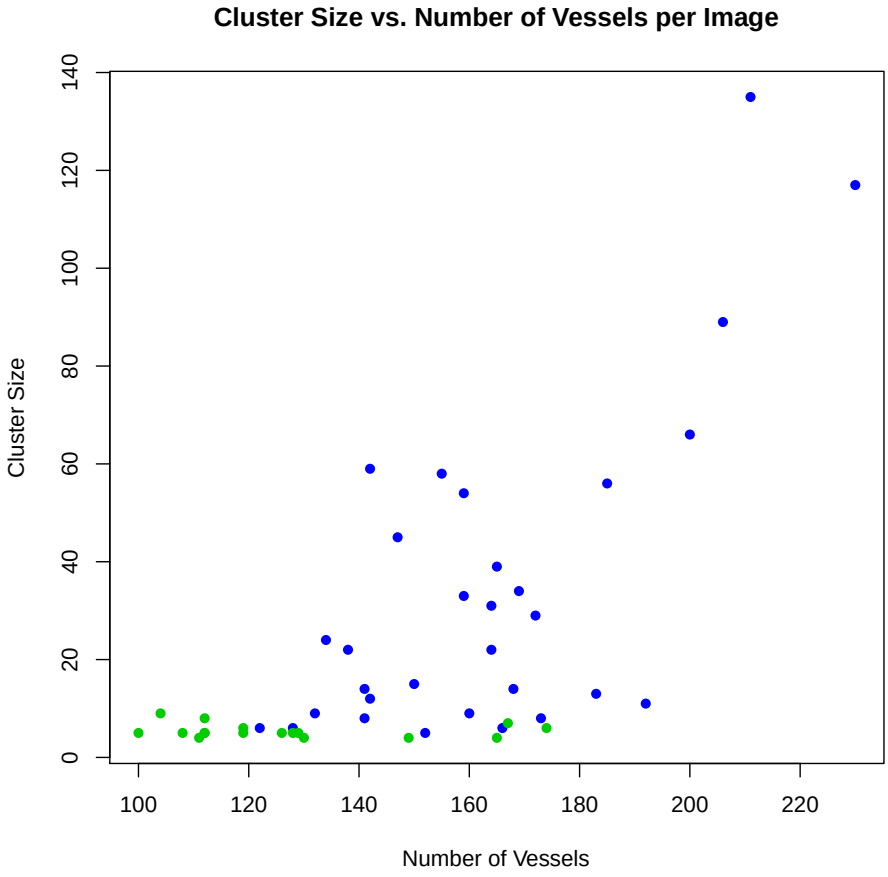

Figure 6.7: The size of the largest cluster formed with DBSCAN clustering versus the total number of vessels segmented per image. Tumors are shown in blue and controls are shown in green. Note that tumor images with more vessels tend to form large clusters, but there is no such relationship in the control images.

Larger tumors are expected to contain more numerous tortuous vessels, increasing the likelihood of the formation of clusters. Therefore, linear regression between tumor diameter and maximum cluster size generated with DBSCAN was used to test the hypothesis that larger tumors form larger clusters. The results of the linear regression revealed a significant correlation between the two variables, with a R^2 value of 0.3798, and $p = 0.0001$. The scatter plot and the line of best fit are plotted in figure 6.8.

Since tumor diameter and cluster size are correlated, we expect the overall performance to vary based on the sampling of tumor diameters included in the analysis

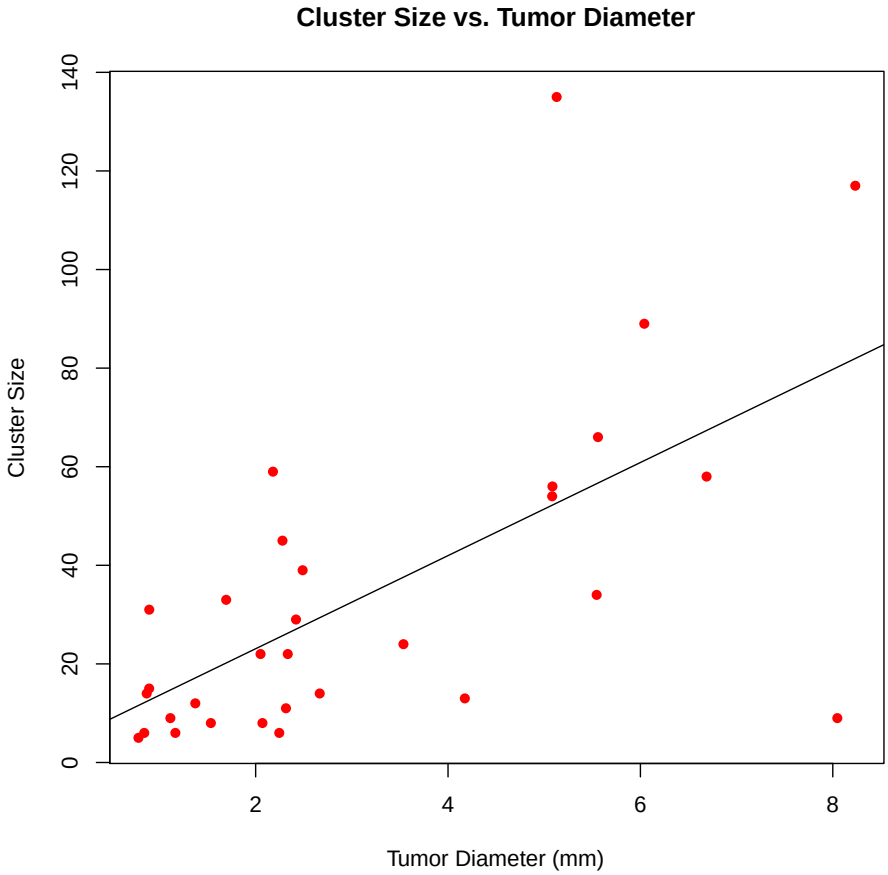

Figure 6.8: Size of the largest cluster formed with DBSCAN clustering versus tumor diameter. There is a significant positive correlation using linear regression with $R^2 = 0.38$ and $p = 1 \times 10^{-4}$.

when cluster size is used as the classification parameter. To test this assumption, ROC curves of the clustering results were computed on subsets of the images using different thresholds for the minimum tumor diameter included in the data sample. Figure 6.9 shows a scatter plot of area under the ROC curve versus the minimum tumor size. For data subsets with minimum tumor diameters of at least 2.2 mm and above, the average area under the curve is 0.9974 ± 0.0008.

The area under the ROC curve depends on sensitivity and specificity of the classifier, and specificity refers to the rate at which negative cases (controls) are correctly

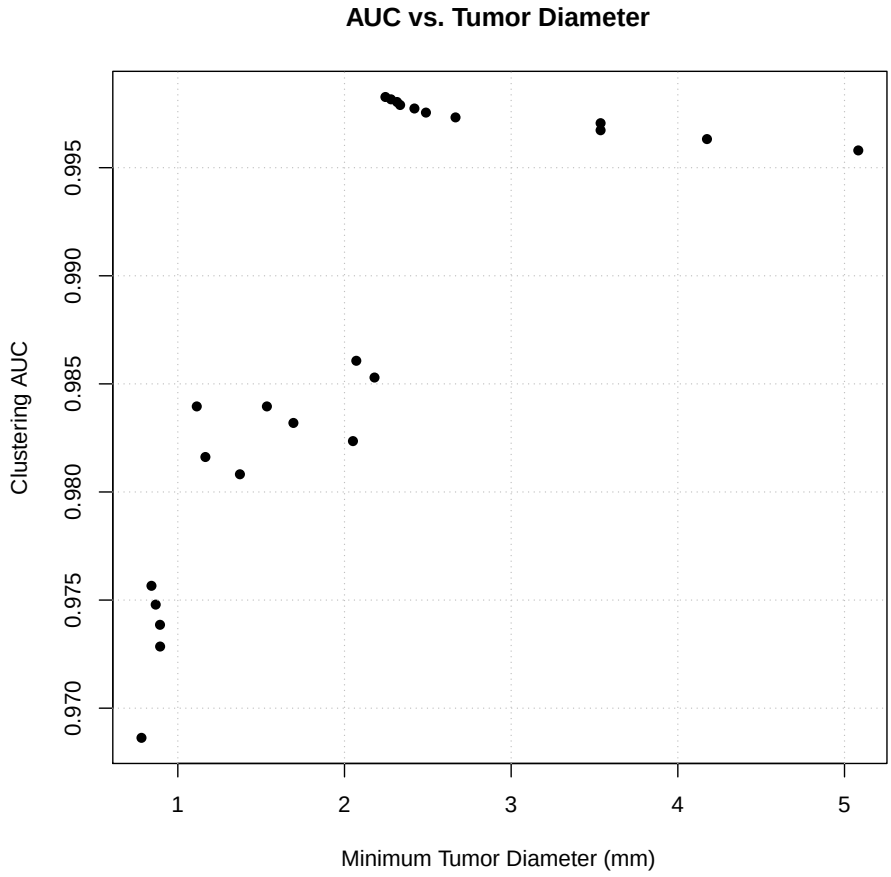

Figure 6.9: Area under the ROC curve for DBSCAN using maximum cluster size as influenced by increasing the cutoff of the minimum tumor diameter included in the sample. For tumors larger than approximately 2.2 mm the AUC is above 0.995.

identified. Therefore, because specificity is calculated based on the classification of controls (true negatives vs false positives), tumor size has no influence on this statistic. Sensitivity, on the other hand, is directly related to the rate at which positive cases (tumors) are correctly identified, and thus is tied to tumor diameter due to its correlation with cluster size. Figure 6.10 shows a scatter plot of sensitivity vs minimum tumor diameter, similar to the AUC plot shown in figure 6.9. Using a threshold of 8, sensitivity is 1 and specificity is 0.8824 for tumors larger than 2.2 mm.

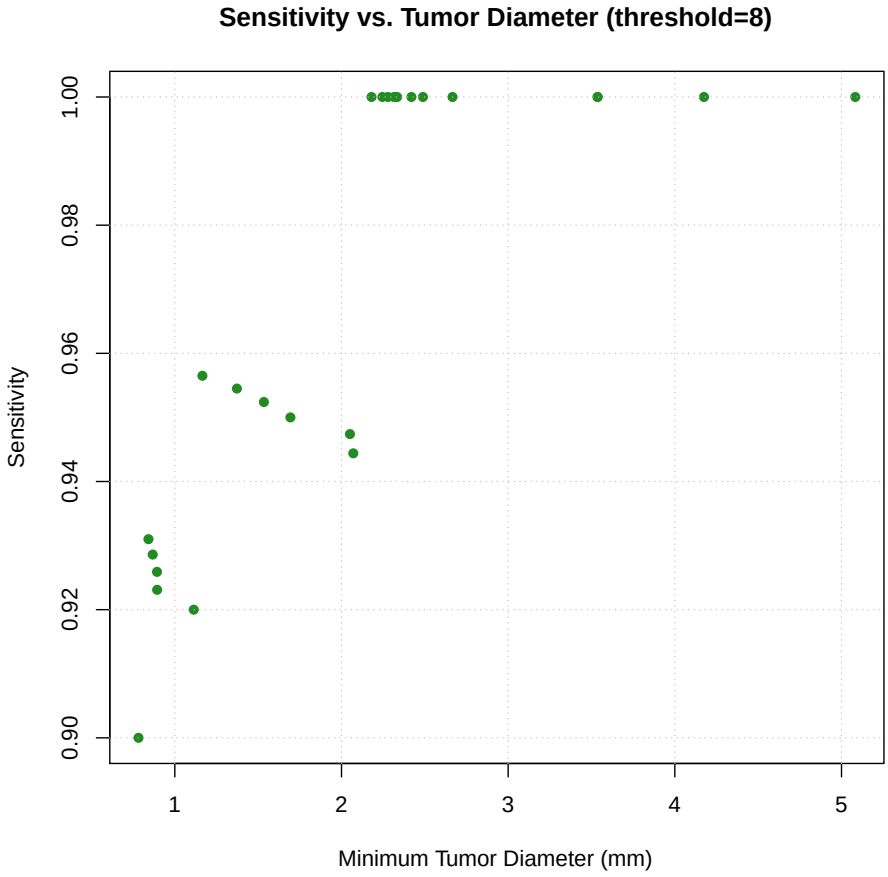

Figure 6.10: Sensitivity of tumor detection using maximum cluster size with a threshold of 8, as a function of minimum tumor diameter. For tumors larger than about 2.2 mm the sensitivity equals 1.

The excellent results obtained on the training data suggest that density based clustering is a very effective method for combining tortuosity metrics with spatial information for image classification. Therefore this approach was applied to a larger data set to test its validity on new data and ensure that the model is not overfit. Since the training data showed sensitivity to be dependent on tumor size, the test data set includes many small tumors in order to determine the approximate limit of detection using this methodology.

6.5 TEST DATA RESULTS

The data set used for testing the clustering algorithm consists of 77 image volumes, including 43 tumor images and 34 controls images, acquired from 34 different mice. Multiple images from a single animal may consist of opposite sides of the mammary pads or from images acquired in tumors weeks apart (at least 1 week) to capture different stages and sizes of tumor growth. Each image is assumed to represent an independent data point in this analysis. The distribution of tumor sizes, shown in table 6.3, included several tumors smaller than 1 mm in diameter, and ranged from 0.32 to 3.86 mm. The mean and standard deviation of the tumor diameter was 1.3 $\pm$ 0.85, with a median of 0.915 mm.

Table 6.3: Statistics of tumor diameter (in mm) from the 43 tumors in the test data set.

Mean	1.3
Median	0.92
Standard deviation	0.85
Minimum	0.32
Maximum	3.86

Several results seen in the training data were recapitulated in the test data set. The area under the ROC curve is not significantly different, with an AUC of 0.964 and a 95% confidence interval of 0.898-0.984. Figure 6.11 shows the smoothed ROC curve for the test data set.

Furthermore, the optimal cutoff of the test data set is equal to 8 (vessels per cluster), the same threshold found in the training data. At this threshold, the sensitivity and specificity of classification are both above 90%, with a sensitivity of 0.907 and a specificity of 0.912. Sensitivity, specificity, and their 95% confidence intervals were computed with the pROC package in R [168], and are listed in table 6.4.

We can also adjust the threshold if higher sensitivity (lower threshold) or specificity

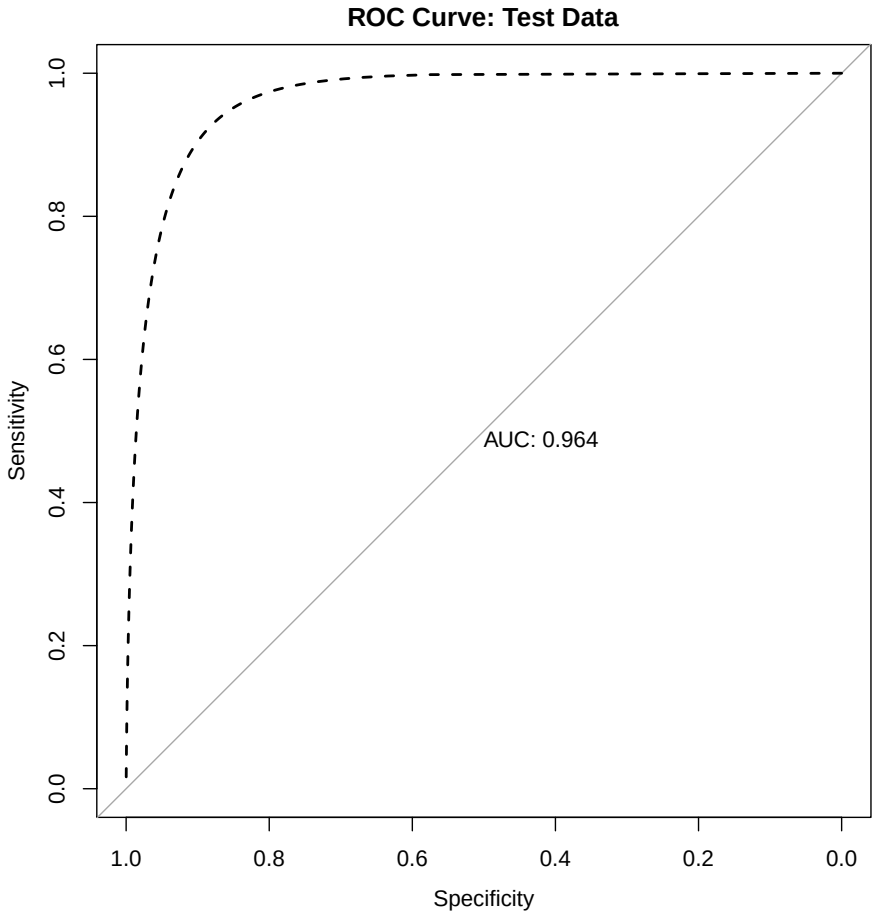

Figure 6.11: Smoothed ROC curve for classification using maximum cluster size derived from DBSACN clustering with eps=27 and minPts=4.

(higher threshold) are desired. A higher sensitivity identifies more true cases of disease, at the expense of a greater number of false positives. On the other hand, higher specificity reduces the number of false positives, but may miss additional cases of disease. We can adjust the classification threshold to favor either of these approaches or to weigh sensitivity and specificity equally. Table 6.5, below, lists the sensitivity and specificity achieved for thresholds between 6 and 21. At a cutoff of 6, the test has perfect sensitivity (1), meaning that all cases of disease are correctly identified. At this level of sensitivity, the specificity is 0.706, which means that there is a false positive rate of 29.4%. At the other end of the spectrum, a threshold of 21 ensures that there

Table 6.4: Sensitivity and Specificity values for classification of the test data set with a cutoff threshold of 8. Median values and confidence intervals were computed using 2000 stratified bootstrap replicates.

	Median	95% CI
Sensitivity	0.907	(0.814-0.977)
Specificity	0.912	(0.824-1)

are no false positives (a specificity of 1), but the sensitivity falls to 0.535.

Table 6.5: Median sensitivity and specificity calculated for several thresholds.

Threshold	Sensitivity	Specificity
6	1.0	0.706
7	0.930	0.794
8	0.907	0.912
9	0.837	0.941
10	0.814	0.941
11	0.791	0.971
21	0.535	1.0

We can also apply the same analyses to the test data as we completed on the training data in order to compare the trends and improve our confidence in the model. The plot of maximum cluster size versus total number of vessels per image shows a similar trend as the training data, shown in figure 6.13. Using linear regression, neither the tumor nor control images have a significant correlation between cluster size and number of vessels, indicating that the number of vessels segmented from an image is not a confounding factor in the clustering analysis.

Comparison of the maximum cluster size to the diameter of each tumor indicated a positive linear correlation with $p = 1.23 \times 10^{-5}$ and $R^2 = 0.37$. This data is seen in figure 6.13 with the line of best fit plotted, and the optimal threshold of 8 indicated with a dashed gray line. The trend is similar to that of the training data, which was shown in figure 6.8. One way to assess the minimum detectable tumor size is to use the regression line of best fit to extrapolate and predict at what tumor diameter the expected maximum cluster size drops below 8 (the optimal cutoff). However, the line of

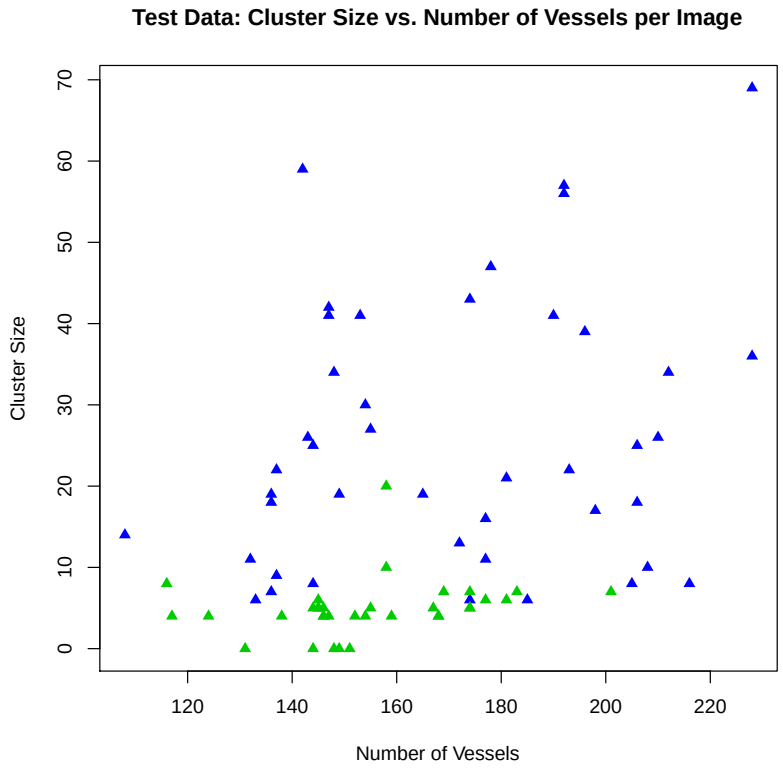

Figure 6.12: Maximum cluster size plotted versus the total number of vessels segmented from each image in the training data. Tumors are shown in blue and controls are indicated in green.

best fit calculated with linear regression has an intercept of 10.5, so we cannot estimate the minimum diameter using this method. Alternatively, we can set the intercept at zero for the regression, which is analogous to assuming that no clusters form when no tumor present. This was our hypothesis for the control cases at the initiation of clustering analysis, so it may be a more appropriate restriction for using the existing data to extrapolate. The slope of the regression line with 0 intercept is 17.4 $\pm$ 1.4. From this value, we can estimate the size of the smallest detectable tumor by setting y to our desired threshold (8) and calculating x. With a cutoff of 8, the estimated detection limit for tumor diameter is 0.46, with a range of 0.42-0.5. However, due to variability in the model, we see that a couple of tumors smaller than 0.5 mm were

detected with more than 8 vessels per cluster, and a handful of tumors between 0.5 and 1 mm in diameter did not meet the cutoff for detection, so this estimate of the detection limit is approximate.

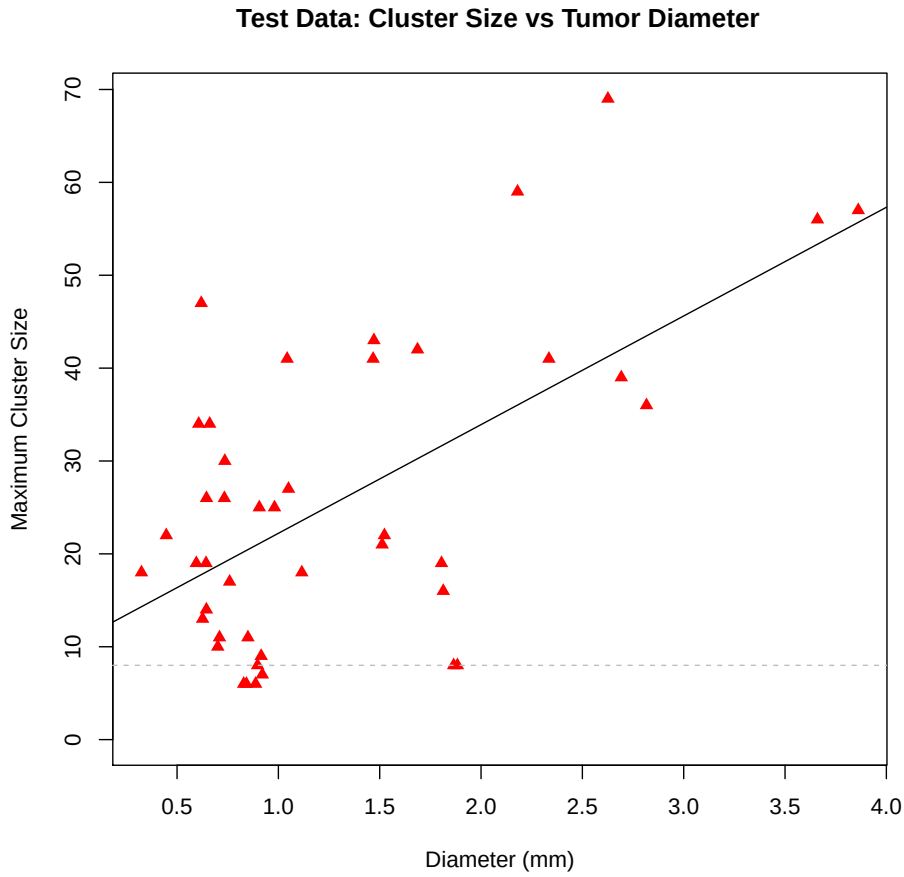

Figure 6.13: Maximum cluster size plotted versus tumor diameter with the line of best fit and the optimal threshold of 8 indicated with a dashed gray line.

In addition to the maximum cluster size, which was used for classification, other clustering parameters were significantly different between the tumor and control classes. The number of clusters generated per image was significantly higher in tumor images than in controls using a two sided t-test ($p = 6.4 \times 10^{-7}$). The control class had an average of 2.8 $\pm$2.3 clusters per image, while the tumor class had 5.7 $\pm$2.4 clusters per image. However, this parameter has considerably more overlap than the maximum

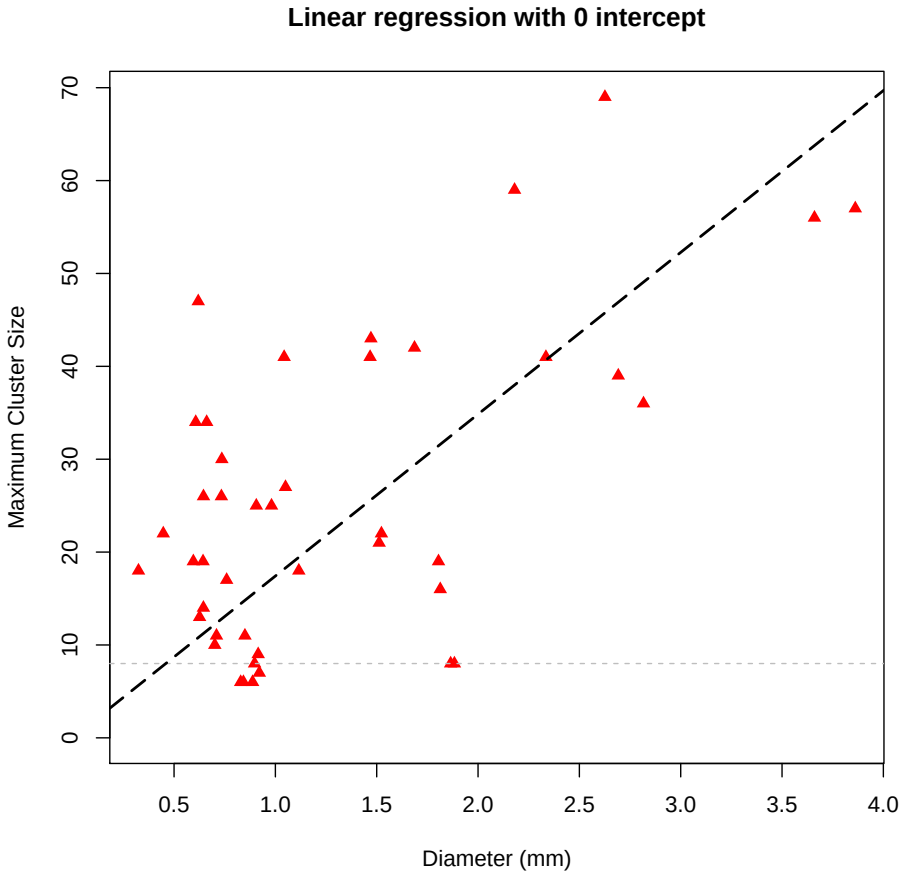

Figure 6.14: Linear regression of maximum cluster size versus tumor diameter with a fixed intercept of (0,0) to establish the detection limit. The estimated detection point is where the regression line and the horizontal line indicating the threshold cross, at a diameter of 0.459.

cluster size and resulted in an area under the curve of 0.818 (0.71-0.92). Total number of vessels clustered was also significantly higher in tumors than in controls ($p = 9.0 \times 10^{-14}$). Tumor images had approximately 4 times as many vessels included in clusters than in control images, with 13.4 $\pm$ 12.8 vessels clustered in control images versus 53.5 $\pm$ 24.1 in tumor images. The area under the curve for total number of vessels clustered was 0.93 with a 95% confidence interval of 0.89-0.97. Of these 3 criteria derived from density based clustering, maximum cluster size had the best performance for classifying tumor images from controls with the highest area under the ROC curve (0.96).

The mean sum of angles metric for each image was also higher in the tumor class (3.79 $\pm$0.34) than the control class (3.1 $\pm$ 0.38), and the difference is significant using parametric (t-test) or non-parametric (Wilcoxon rank sum) tests, with $p < 10^{-12}$. However, mean sum of angles metric does not perform as well as maximum cluster size, and has an area under the curve of 0.91 (0.82-0.96). Furthermore, it is not significantly correlated to tumor size (see figure 6.15), so we can not estimate a minimum detection size using the SOAM. The mean distance metric was not significantly different between tumors and controls.

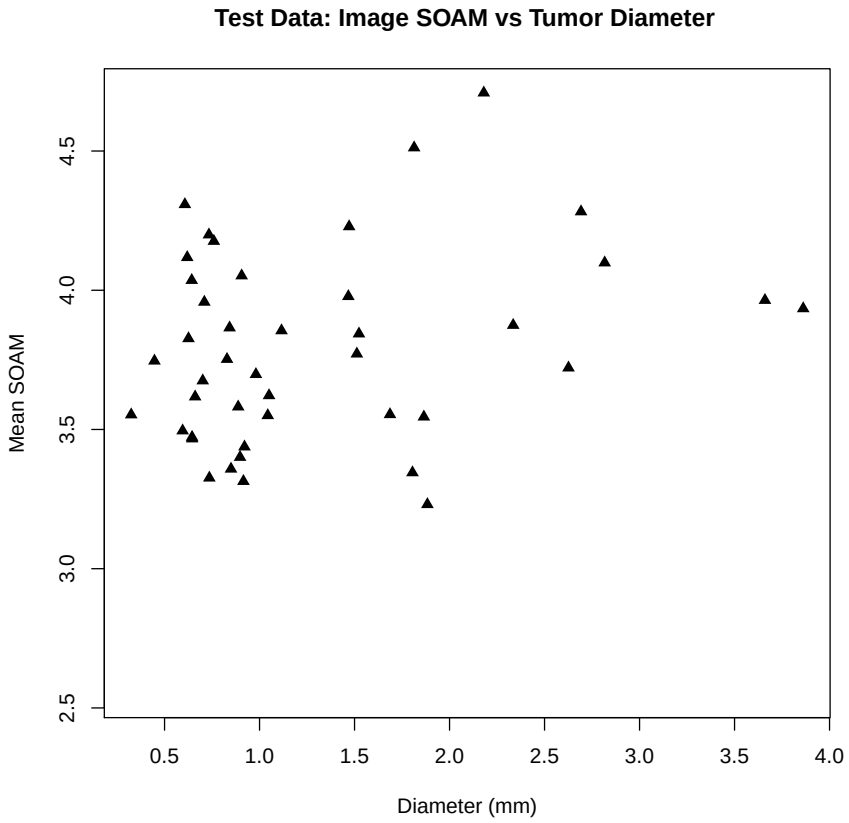

Figure 6.15: Mean sum of angles for each image plotted against tumor diameter.

6.6 DISCUSSION

The vascular density and morphological abnormalities that are associated with cancer neovasculature can make angiography imaging a particularly useful diagnostic method, especially when combined with sophisticated image analysis. Image classification based on vascular features can provide a quantitative, robust method of tumor detection by incorporating tortuosity metrics and spatial information. In this chapter we have explored several methods for binary classification of acoustic angigography images, and discussed the advantages and limitations of each method. The best classification method was the use of the Density Based Statistical Clustering in Applications with Noise (DBSCAN) algorithm to assign clusters to the vessels in each image, followed by using the maximum cluster size produced as the classfier. This approach resulted in an area under the curve of approximately 0.95 for the training data and test data sets used in the analysis.

These results indicate that quantitative, multivariate methods of tumor detection based on vascular tortuosity were more successful at discriminating between tumors and controls than visual classification using the reader study approach from chapter 5. The approximate area under the curve using visual discrimination was 0.8, compared to 0.95 for the DBSCAN clustering approach. Using regression on the ROC curves from the reader study, we estimated that tumors approximately 5.1 mm in diameter resulted in an area under the curve of 0.96, indicating that readers required larger tumors in order to match the performance of the quantitative classification described in this chapter. However, one similarity between the results of the reader study and clustering-based classification is their dependence on tumor size. Using both approaches, we observed that area under the ROC curve was significantly correlated to tumor diameter, with sensitivity improving with increasing tumor diameter.

We also compared a number of quantitative classification metrics and methods

against each other. Single-metric classification based on the mean sum of angles metric and distance metric showed moderate performance, with the sum of angles metric performing significantly better than the distance metric with an AUC of 0.82. Combining these two tortuosity metrics, along with vessel radius, resulted in a slightly improved AUC of 0.87 using logistic regression.

However, the main disadvantage to these approaches is the susceptibility to outliers inherent in using summary statistics to represent an entire image. Distributions of tortuosity data are not well represented by normal distributions and frequently contain outliers in one or more metrics that exert a strong influence on the mean. There are several well accepted methods for outlier removal, but most are based on the assumption of normality, which is broken by this data. Furthermore, extreme data points that represent real blood vessels (high tumor tortuosity) are the information that we wish to capture in order to detect tumors in angiography data, so extensive or arbitrary removal of "outlier" data is undesirable. Therefore, the main goal of this chapter was the development of a multivariate classification model that was robust and did not rely on statistical summaries of the vessels within a single image.

Density Based Statistical Clustering in Applications with Noise enabled us not only to combine multiple metrics of vessel morphology, but also to take spatial relationships between vessels into account. Maximum cluster size was the best parameter for discriminating between tumors and controls, but the total number of vessels included in all clusters (excluding vessels classified as noise) also showed excellent classification with an AUC of 0.93, slightly lower than the 0.96 AUC observed using maximum cluster size to classify images. The other feature generated by DBSCAN clustering that could be used for classification was the number of clusters generated, but this metric did not perform as well as the other metrics derived from DBSCAN clustering.

Comparisons between the training data (n = 48 images) and test data (n = 77

images) indicated that the use of maximum cluster size to perform classification was a robust method that was not overfitted to the training data. Calculation of the ROC curve for both sets of data resulted in no significant difference between the areas under the curve of the two data sets, which resulted in AUCs of 0.95 and 0.96. Furthermore, calculation of the optimal threshold for maximum cluster size resulted in a cutoff value of 8 for both sets of data weighing sensitivity and specificity equally.

This clustering approach could be applied directly to other 2D or 3D images of vasculature where tortuosity and vessel location can be identified. Additionally, the concept of spatial, density-based clustering could be extended to other applications of interest in medical image analysis. Any data set that can be divided into structures with quantitative features could be amenable to density-based clustering akin to the methodology described here.

CHAPTER 7

MOLECULAR IMAGING

7.1 OVERVIEW

Ultrasound molecular imaging utilizes microbubbles targeted to extracellular proteins expressed on endothelial cells in order to assess levels of expression of a vascular target of interest. Through the use of microbubbles which can bind to a specific receptor or protein, the signal of bound bubbles can be differentiated from freely flowing microbubbles to quantify molecular targeting. Typically this is accomplished by waiting for the majority of circulating microbubbles to clear (on the order of minutes), acquiring an image of the bound microbubbles, and calculating targeting signal by subtracting contrast intensity images acquired before and after a destructive pulse or by filtering contrast images to separate stationary (bound) microbubbles from ones in circulation (unbound). Alternatively, one can monitor the image intensity during contrast wash-in and wash-out in order to plot a time-intensity curve and compare curve-fitting parameters to those derived from monitoring the same dose of a control microbubble. Bound microbubbles produce sustained contrast signal in the wash-out phase, which does not occur for unbound microbubbles. These methods generally involve monitoring contrast intensity in real time using low mechanical index (MI) contrast-specific pulse sequences. Therefore, the implementation of superharmonic molecular imaging poses challenges due to the semi-destructive nature of the imaging method.

Previous acoustic angiography imaging studies have been carried out during a continuous infusion of microbubble contrast to ensure that the microbubbles that are destroyed during imaging are replenished via perfusion. However, molecular imaging relies on an initial bolus injection, followed by quantification of the microbubbles which bind to the vasculature, and replenishment is impossible. Furthermore, molecular imaging is a modality in which sensitivity and specificity to contrast signal are of the highest importance, given the relatively low concentration of targeted microbubbles that accumulate at sites of pathology. Therefore, maximizing CTR while ensuring sensitivity to low concentrations of contrast agent is important for effective molecular imaging.

One group demonstrated superharmonic molecular imaging using a low MI combined with interframe filtering [141]. The resulting images were similar in quality to the traditional multi-pulse imaging available on clinical ultrasound systems, and the low MI used allowed them detect some superharmonic microbubble behavior without immediately destroying microbubbles, which permitted them to perform time series imaging and interframe filtering. In a subsequent study, they reported that superharmonic molecular imaging transmitting at 2 MHz and receiving at 15 MHz resulted in spatial resolution of half that of conventional molecular imaging [142]. However, as discussed in chapter 2, previous work by our group has demonstrated that the strongest superharmonic signals occur when microbubbles are destroyed, and a significantly lower level of superharmonic behavior is also produced when bubbles are partially deflated, but not destroyed in a single cycle [146]. Since CTR is linked to microbubble destruction, and therefore transmit pressure, low MI imaging schemes do not optimize CTR and may not provide substantial benefits over conventional contrast imaging schemes. Additionally, we would like to take advantage of the improved resolution achieved by receiving at 25-30 MHz in order to combine molecular imaging and images of well-resolved vascular morphology.

Most ultrasound molecular imaging takes advantage of the sensitivity to low concentrations gained by using contrast imaging modes that rely on the second harmonic or non-linear imaging strategies in the low harmonics range. These methods have been very effective at employing ultrasound molecular imaging for studying tumors and other types of disease, but these imaging modes can suffer from strong tissue artifacts (low CTR) and poor resolution at low frequencies (especially in the case of subharmonic imaging) [191–199]. Acoustic angiography has demonstrated excellent resolution and contrast to tissue ratios in previous *in vivo* studies using infusions of microbubbles, but its performance at much lower contrast concentrations of bound microbubbles is unknown. Therefore, this chapter describes the experiments designed to test this trade off between sensitivity, CTR and resolution, in order to determine if and how molecular acoustic angiography can be performed.

As described by Lindsey et al. [146], the production of a superharmonic response relies upon microbubbles breaking or shrinking. This effect depends on the transmitted pressure and frequency, and the microbubble diameter. Smaller microbubbles are more susceptible to disruption than larger bubbles across all frequencies and pressures, and large bubbles are able to persist for longer (more pulse cycles) than smaller bubbles [146]. Also, lower transmit frequencies are more effective at producing microbubble disruption (shrinking or breaking behavior), which is reinforced by the improved CTR observed for low transmit pressures in another study by Lindsey et al. [159]. However, across all microbubble sizes and transmit frequencies, increasing pressure produces higher amplitude superharmonic responses up to the level where complete microbubble destruction occurs. Since microbubble breakage produces signals with approximately 4 times higher amplitude than shrinking microbubbles, CTR is maximized by inducing microbubble breakage while minimizing tissue response [147, 159].

The ultimate goal for superharmonic molecular imaging is to combine it with acoustic angiography images using untargeted microbubbles in order to visualize patterns of both molecular targeting and vascular morphology. This goal was approached in 3 phases: determining what conditions enable high-resolution, high-contrast superharmonic molecular imaging, comparing the performance of superharmonic molecular imaging to traditional, multi-pulse imaging, and finally, to combine molecular and vascular morphological information in order to take full advantage of molecular acoustic angiography.

7.2 *IN VITRO* EXPERIMENTS

7.2.1 *IN VITRO* METHODS

In vitro work used cellulose tubes and biotin-avidin binding to mimic molecular imaging *in vivo*. Cellulose tubes (Spectrum Labs, Rancho Dominguez, CA) were first filled with ethanol (100%) and flushed with air. Then tubes were filled with avidin (Sigma-Aldrich, St. Louis, MO) prepared at 5 mg/mL in phosphate-buffered saline (PBS, Fisher Scientific, Pittsburgh, PA) and left for 30 minutes at room temperature. Next the avidin solution was removed from the tube by flushing with PBS. The tube was then placed in a water bath for imaging and positioned at the focus of the transducer.

Biotinylated microbubbles were prepared by with equal parts DSPE-PEG2000 (1,2 - distearoyl - *sn* - glycero - 3 - phosphoethanolamine, PEG2000) and DSPE-PEG2000-Biotin. The pegylated lipids were combined with DSPC (1,2 - distearoyl - *sn* - glycero - 3 - phosphocholine) in a 1:1:18 ratio (Avanti Polar Lipids, Alabaster, AL). Microbubbles were created by replacing the headspace in 3 mL vials containing 1.5 mL of 1 mg/mL lipid solution with decafluorobutane (Fluoromed, Round Rock, TX) followed by mechanical agitation using a VialMix mixer (Lantheus Medical Imaging, N. Billerica, MA). Free lipid was removed using centrifugation. This resulted in a population

of microbubbles approximately 1.4 μm in diameter, measured using an Accusizer 780 (Particle Sizing Systems, Santa Barbara, CA).

Once the avidin-coated cellulose tubes were positioned at the focus of the transducer, microbubble targeting was achieved by infusing 300 μL of biotinylated microbubble solution (containing a total of 5 $\times 10^4$ microbubbles) through the tube at a rate of 30 μL/min, followed by 300 μL of PBS to clear unbound microbubbles. Then imaging was performed to assess the magnitude of contrast signal received for different transmit pressures and to measure the contrast signal change due to successive transmits in order to evaluate microbubble destruction. The transmit pressures were verified using a calibrated hydrophone (HNA 0400, Onda Corp., Sunnyvale, CA) in a water bath prior to the imaging experiments. A single cycle, cosine-windowed sinusoidal pulse beginning with a negative half cycle was used for the transmit in each experiment.

7.2.2 *IN VITRO* RESULTS

Optimizing CTR by maximizing microbubble breakage will result in the loss of contrast agents during molecular imaging of bound microbubbles if the low frequency transmit pulse subjects a large volume of tissue to extreme pressures. In dual-frequency imaging, the beam width of the low frequency transmit is larger than the high frequency receive, so the transmit pressure must be chosen carefully in order to avoid disturbing surrounding microbubbles with the relatively large low frequency transmit beam width. If the width of the tissue subjected to pressures high enough to cause microbubble destruction is smaller than the line spacing chosen for high resolution imaging, then bound contrast will be destroyed before it can be detected by the high frequency receive element.

The hydrophone-measured plots (below) of the pressure field induced from the low frequency transmit illustrate that while the full-width half-max beam width does not

vary with pressure, the width of the field exposed to pressures that can cause microbubble destruction is considerably different at the 3 pressures tested. Figure 7.1 shows the ultrasound pressure field in the lateral dimension at 3 different peak negative pressure (PNP) transmits at 4 MHz. We expect that pressure of approximately 200 kPa induces microbubble shrinking, and fragmentation predominates for pressures above 400 kPa when transmitting 4 MHz, for 1-2 μm bubbles, *in vitro* [146]. Therefore, horizontal lines at 200 and 400 kPa and the shaded regions of the graph indicate the pressure levels likely to induce microbubble disruption and destruction from a 4 MHz transmitted pulse. Additionally, the transducer possesses radial symmetry, so the data shown in this plot also apply to the elevation dimension.

Though the thresholds indicated for microbubble shrinkage (200 kPa) and microbubble breakage (400 kPa) are approximate and also depend on the microbubble diameter (which we have assumed to be approximately 1-2 mm here), this figure illustrates the need to balance transmitted pressure and spacing of lines and frames in order to minimize the destruction of microbubbles outside the high frequency field of view. Transmitting a 200 kPa pulse limits microbubble disruption to the center of the focus, but this comes at the expense of reduced superharmonic generation. Transmitting with higher pressures can increase the amount of superharmonic scattering generated by microbubbles, but off-axis targets experience pressures greater than 200 kPa for the transmit pulses at 350 and 500 kPa, indicating that microbubble disruption is likely to be occurring outside of the high frequency receive. Since the approximate threshold for microbubble destruction is approximately 400 kPa, for a 350 kPa transmit the off-axis disruption is likely to be mostly shrinking, but there is a likelihood of additional microbubble destruction at 500 kPa, due to the wider area subjected to pressures above 400 kPa. Therefore, the transmitted pressure should be selected to provide enough pressure to produce microbubble destruction at the focus, while minimizing disruptive

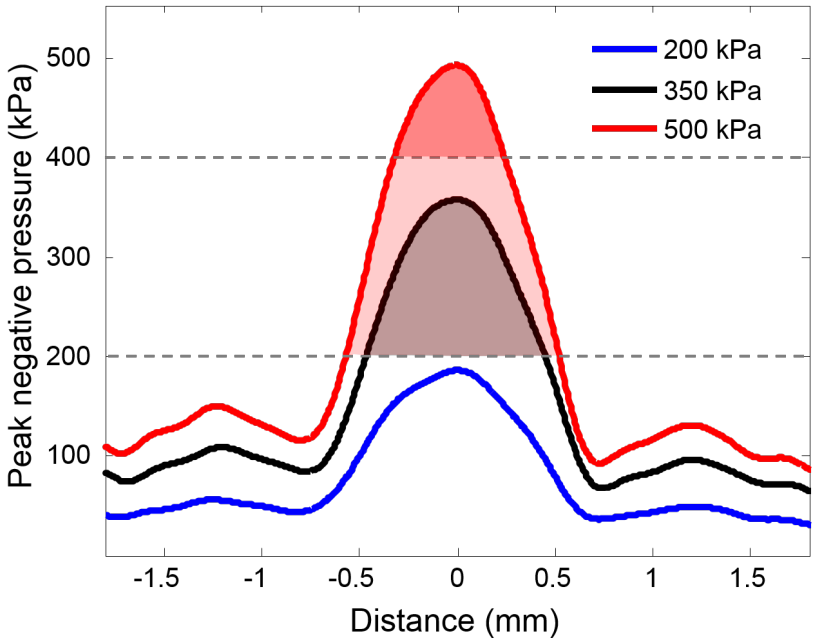

Figure 7.1: Lateral pressure field of 4 MHz transmitted pulse at 200, 350, and 500 kPa. Shaded regions indicate approximate extent of microbubble disruption, which is mostly shrinking above about 200 kPa and includes more fragmentation above for pressures higher than 400 kPa, assuming 1-2 μm diameter microbubbles.
Adapted and reprinted from Ultrasound in Medicine & Biology, Volume 42, Issue 3, Sarah E. Shelton*, Brooks D. Lindsey*, James K. Tsuruta, F. Stuart Foster, Paul A. Dayton, Molecular Acoustic Angiography: A New Technique for High-Resolution Superharmonic Ultrasound Molecular Imaging, Pages 769-781, ©2016, with permission from Elsevier.

pressures in adjacent regions.

In order to compare the effect of transmitted pressure on imaging of bound microbubbles, the backscattered contrast intensity received over 100 frames was compared for pressures between 200 and 500 kPa in the biotin-avidin *in vitro* model of molecular imaging. Results from the avidin-coated tubes in water baths revealed that initial backscattered superharmonic signal from bound biotin microbubbles increased while increasing transmit pressure from 200-500 kPa (see figure 7.2).

The initial intensity received from bound microbubbles was approximately 5 times

higher when transmitting at 500 kPa than at 200 kPa. However, at this higher pressure, there was a significant amount of microbubble fragmentation and the intensity of subsequent pulses dropped quickly as microbubbles were destroyed and the core gas dissolved into the blood. Comparing the contrast intensity at pulse 1 and pulse 100, the amount of backscattered contrast signal was lower at pulse 100 at every pressure tested (as expected), and the largest decrease was for the highest pressure transmit of 500 kPa. At 350 and 500 kPa, the intensity continued to decrease between consecutive frames across all 100 frames, but 2 the lower pressure transmit pulses showed a different pattern. At 200 and 300 kPa, contrast signal decreased over the first few frames (approximately 10), but then the contrast signal stabilized and did not continue to decrease significantly. However, the stable level of superharmonic contrast enhancement observed in frames 10-100 was very low and close to the noise floor, especially for the lowest transmit pressure tested (200 kPa).

The largest drop in contrast intensity occurred for the 500 kPa transmit pulse, and it dropped below the amplitude of contrast signal exhibited by the 350 kPa pulse within 5 frames. However, the initial signal for the 500 kPa transmit was more than double that of the 350 kPa pulse, so this suggests that one may design a transmit pressure regime either for maximum contrast signal (at higher pressures) or to provide a somewhat steady contrast signal across several frames (at moderate pressures).

These *in vitro* tests confirmed the hypothesis that transmit pressures designed to maximize CTR through focused microbubble destruction are also appropriate for molecular imaging of bound microbubbles, but that the maximal contrast signal is lost after only a few frames at these pressures. Therefore, a superharmonic molecular imaging protocol must ensure that data can be acquired with a single transmit pulse. Figure 7.3, below, shows images from the first transmit cycle applied to 2 tubes containing equal concentrations of targeted bubbles imaged with pressures of either 350 kPa or 500

kPa at the focus. These results confirm that the higher transmitted pressure provided a much clearer image of the targeted microbubbles in the tube, and the highest contrast to tissue ratio.

Additional studies were performed to translate these findings to *in vivo* imaging, which requires higher pressures than *in vitro* studies due to attenuation, blood viscosity, and the confinement effects of small diameter vasculature [200–202].

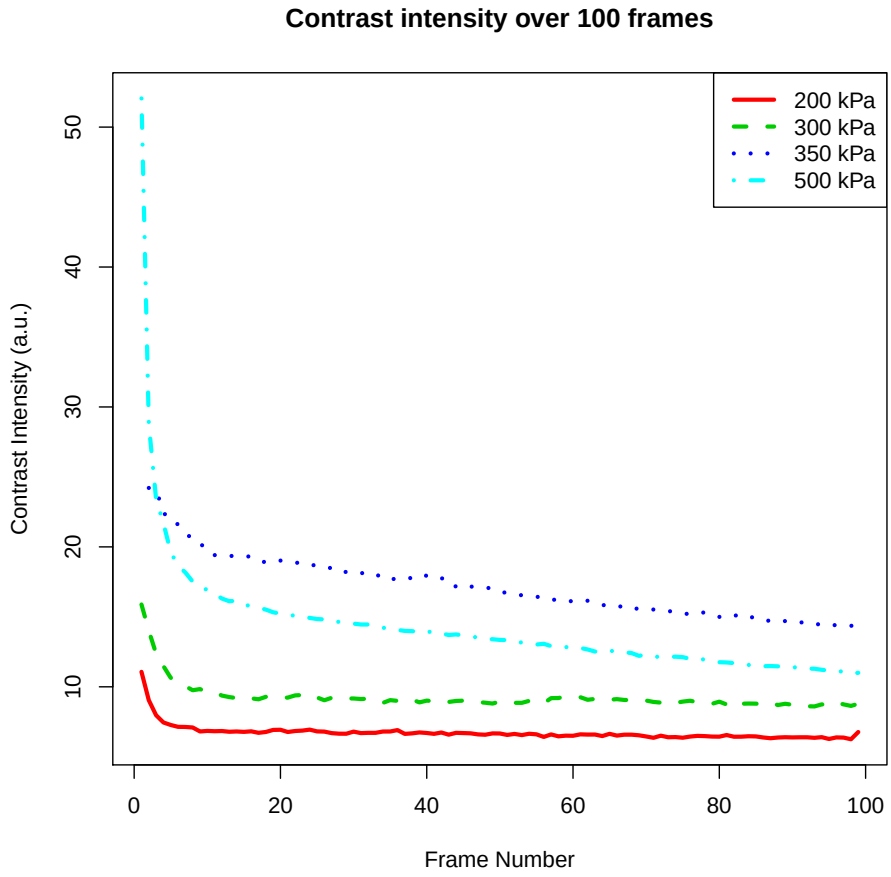

Figure 7.2: Image intensity of biotin-targeted microbubbles in avidinated tubes across 100 consecutive frames at 4 different transmit pressures.
Adapted and reprinted from Ultrasound in Medicine & Biology, Volume 42, Issue 3, Sarah E. Shelton*, Brooks D. Lindsey*, James K. Tsuruta, F. Stuart Foster, Paul A. Dayton, Molecular Acoustic Angiography: A New Technique for High-Resolution Superharmonic Ultrasound Molecular Imaging, Pages 769-781, ©2016, with permission from Elsevier.

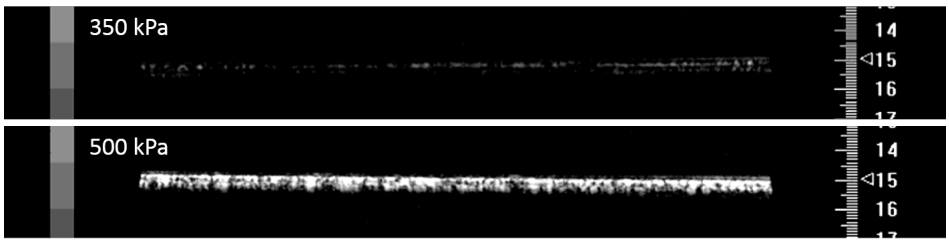

Figure 7.3: Biotinylated microbubbles targeted to avidin-coated cellulose tubes, subjected to 350 kPa (top) or 500 kPa (bottom) transmit pressures. Images are the first frame in which targeted bubbles were insonified.

7.3 *IN VIVO* IMAGING

7.3.1 *IN VIVO* METHODS

In vivo experiments used the rat fibrosarcoma model described previously in chapter 3. The targeting ligand selected is the $\alpha_v\beta_3$ integrin, which can be bound specifically by a cyclic RGD peptide (Cyclo-Arg-Gly-Asp-D-Tyr-Cys, Peptides International, Louisville, KY). Microbubbles bearing the RGD peptide were formulated using maleimide cross-linking to bind DSPE-PEG2000 and the cyclic RGD peptide. The lipid solution was a 1:1:18 molar ratio of DSPE-PEG2000 cross linked to cyclic RGD, DSPE-PEG2000, and DSPC. Microbubbles were prepared either as polydisperse size distributions with a mode of 1.4 μm, after centrifugal washing to eliminate free lipids, or were sorted via centrifugal separation to enrich a larger population of 3.8 μm microbubbles [203] for testing transmit pressures and microbubble diameter in vivo.

During imaging, tumors were first located in B-mode, and pre-contrast scans were collected in dual-frequency mode to acquire images of any tissue signal visible in the higher harmonic range within the bandwidth of the receive transducer (approximately 15-45 MHz). Microbubbles were injected through a tail-vein catheter and a waiting period of 12 minutes allowed microbubbles to circulate and clear before performing superharmonic imaging to acquire targeted images of bound microbubbles. The interval of 12 minutes was chosen for the waiting period based on a preliminary study investigating the clearance rate of untargeted microbubbles in rats (unpublished data). After 12 minutes, there were a negligible number of microbubbles still circulating at the bolus doses listed here, indicating that the contrast signal visible at 12 minutes can be attributed to microbubbles which have bound and persisted. It was also verified that no free bubbles remained after the 12 minute wait by performing a t-test to compare the pre-injection contrast scans to images acquired after the destruction of the

targeted bubbles (after molecular images were acquired), and no significant differences were found. Spacing between frames was set to 250 μm to minimize microbubble destruction in adjacent planes during molecular imaging, but reduced to 100 μm during angiography imaging.

Additionally, comparisons between the CTR of superharmonic molecular imaging with multi-pulse imaging at different contrast doses were carried out using microbubbles targeted to VEGFR2 (Visistar VEGFR2 (VS-102) Targeson, San Diego, CA), composed of a single-chain VEGF fragment. Contrast enhancement was computed by comparing the image intensity of contrast images in the tumor regions to pre-scan images acquired before microbubbles were injected. The images acquired in contrast-specific imaging mode represent tissue signal before microbubbles were injected. Regions of interest were selected around the tumor in each image, and the same ROI locations were used in the contrast image and pre-scan image in order to compute CTR. Further comparisons were made using a selectin-targeted microbubble consisting of a glycoprotein that binds to P- and E-selectin (Visistar Selectin (VS-105) Targeson, San Diego, CA).

Comparisons of superharmonic molecular imaging and conventional contrast multi-pulse molecular imaging were made by acquiring images of each tumor on both the Vevo 770 system with the prototype dual-frequency transducer, and with a Siemens Sequoia scanner using a 15L8 transducer operated in CPS (Cadence Pulse Sequence) mode. Comparisons were made transmitting at a mechanical index (MI) of 0.6 for superharmonic imaging and at 0.2 for conventional CPS contrast imaging. VEGFR2-targeted and selectin-targeted bubbles were injected sequentially to compare their relative targeting intensity and to correlate patterns of targeting to vascular tortuosity.

Vasculature was segmented, and the distance metric was calculated using VesselView (Kitware Inc., Carrboro, NC) and used as the metric of tortuosity. Vessel centerline coordinates and molecular images were imported into Matlab in order to

calculate distances between targeting sites and individual vessels. Targeting sites were identified by applying a median filter to the molecular images, followed by thresholding. Then we used a custom Matlab script to identify the center of mass of each object, and Euclidean distance between each targeting site and each vessel was calculated. The distance metric of each vessel was read as a text file generated using the VesselView program.

7.3.2 *IN VIVO* RESULTS

In vivo imaging requires higher pressures than *in vitro* conditions due to attenuation, viscous damping, and confinement effects of small diameter vessels [200–202]. Therefore, the peak negative pressures tested *in vivo* were increased to 700, 900, and 1200 kPa. Figure 7.4 shows the resulting contrast signal for each of the 3 different transmitted peak negative pressures, across 4 consecutive transmit events.

Figure 7.4 shows that the highest transmitted pressure tested (1200 kPa) resulted in the highest amplitude contrast signal from the cyclic-RGD microbubbles targeted to the $\alpha_v\beta_3$ integrin. The contrast signal from the lowest pressure transmit (700 kPa) was barely above the noise floor, and the intermediate pressure tested (900 kPa) produced approximately 20% as bright a signal as the higher pressure transmit. Each transmit pressure tested showed contrast intensity decreasing with pulse number, as microbubbles were immediately or gradually destroyed, resulting in the production of the superharmonic signals detected by the high frequency transducer. The absolute value of the slope of the line was higher for higher pressures, indicating that more microbubbles were disrupted with each transmit, as we would expect. During the fourth pulse, the contrast intensity was near zero for all 3 pressures tested. However at the first or second transmit, the contrast intensity was highest when transmitting a 1200 kPa PNP pulse, so this pressure was selected for optimal *in vivo* imaging.

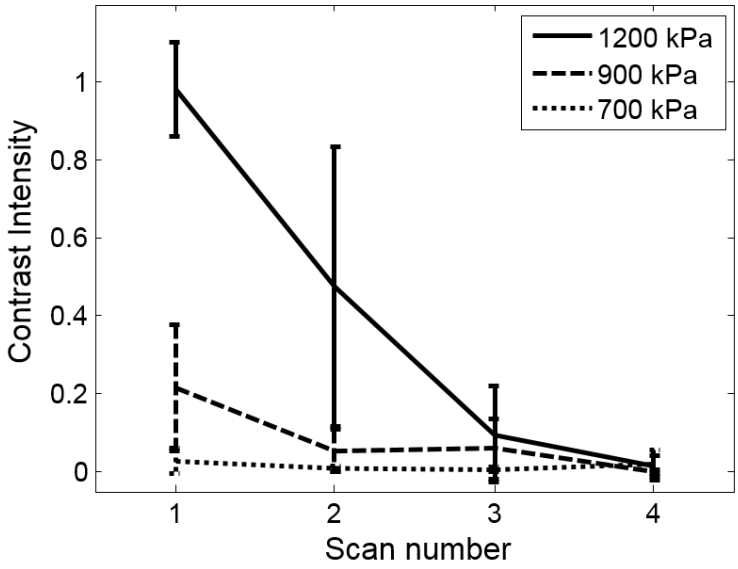

Figure 7.4: Cyclic-RGD contrast image intensity *in vivo* at 700, 900, or 1200 kPa across 4 successive transmit pulses.
Adapted and reprinted from Ultrasound in Medicine & Biology, Volume 42, Issue 3, Sarah E. Shelton*, Brooks D. Lindsey*, James K. Tsuruta, F. Stuart Foster, Paul A. Dayton, Molecular Acoustic Angiography: A New Technique for High-Resolution Superharmonic Ultrasound Molecular Imaging, Pages 769-781, Copyright 2016, with permission from Elsevier.

At 1200 kPa, we also compared the performance of larger 3.8 μm microbubbles to the polydisperse population of microbubbles (approximately 1.4 μm) used up to this point. Figure 7.5 shows the relative contrast intensity generated by equal concentrations of the microbubble distributions approximately 1 μm and 4 μm in diameter, transmitting at 1200 kPa.

When subjected to equal peak negative transmit pressures at 4 MHz, the larger bubbles produced higher intensity contrast signals, more than twice that of the smaller microbubbles. However, after the first frame, there is no significant difference between the contrast generated by the two microbubble populations, and by frame number 4,

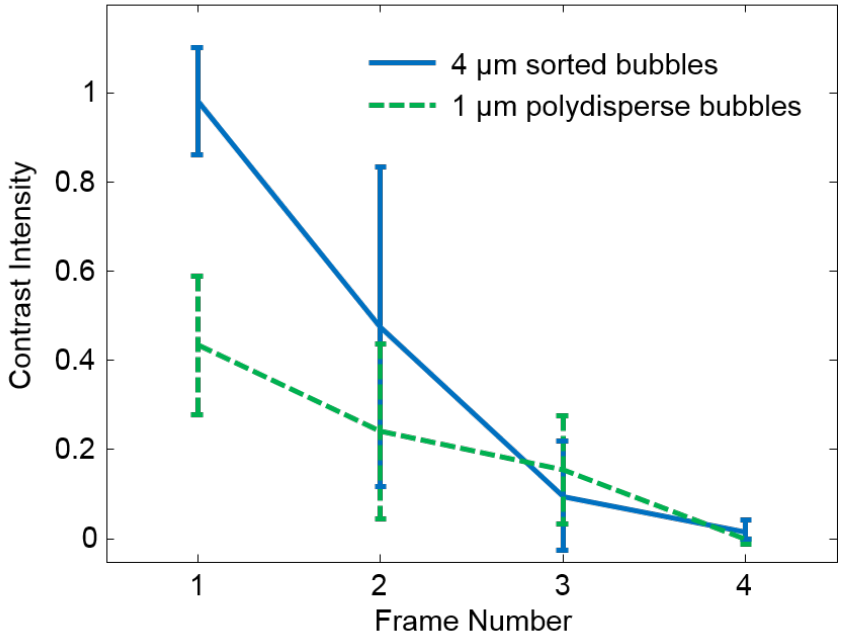

Figure 7.5: Contrast intensity across 4 consecutive transmitted pulses of 1200 kPa for microbubbles approximately 1 μm and 4 μm in diameter. N = 14 rats.
Adapted and reprinted from Ultrasound in Medicine & Biology, Volume 42, Issue 3, Sarah E. Shelton*, Brooks D. Lindsey*, James K. Tsuruta, F. Stuart Foster, Paul A. Dayton, Molecular Acoustic Angiography: A New Technique for High-Resolution Superharmonic Ultrasound Molecular Imaging, Pages 769-781, ©2016, with permission from Elsevier.

there is minimal contrast signal remaining for either diameter of microbubble. Therefore, larger bubbles can improve the contrast signal in superharmonic molecular imaging, but it did not significantly increase the number of frames that can be acquired when transmitting at 4 MHz, 1200 kPa.

We also compared the contrast to tissue ratios achieved with superharmonic imaging to traditional contrast pulse sequence imaging, and also compared the sensitivity of both techniques to low concentrations of targeted microbubbles. Despite the relatively low amplitude of high frequency superharmonic signals compared to the second harmonic, superharmonic imaging has better contrast ratios due to the superior tissue rejection [147]. Figure 7.6 illustrates the difference in contrast for conventional CPS contrast

imaging and dual frequency superharmonic imaging of VEGFR2 targeted microbubbles in the fibrosarcoma tumors across 3 microbubble doses, combined.

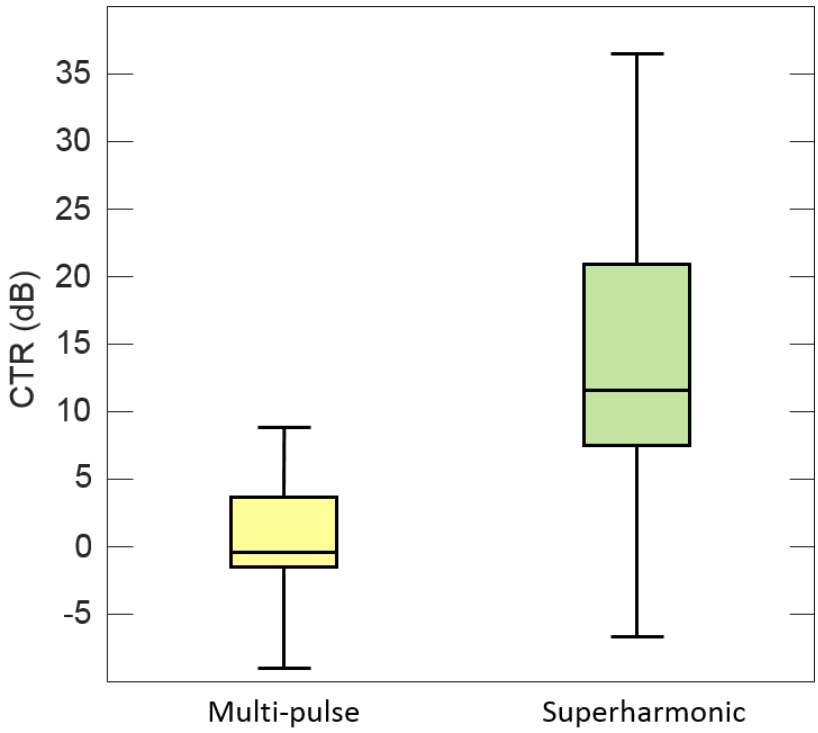

Figure 7.6: Molecular imaging of VEGFR2 targeted microbubbles in fibrosarcoma tumors using either multi-pulse imaging on a Siemens Sequoia scanner (CPS mode) or a superharmonic imaging with a dual frequency transducer to transmit at 4 MHz and receive at 30 MHz. N = 14 rats.
Adapted from Molecular Imaging and Biology, Assessment of Molecular Acoustic Angiography for Combined Microvascular and Molecular Imaging in Preclinical Tumor Models, Volume 19, Issue 2, 2016, pages 194-202, Brooks D. Lindsey*, Sarah E. Shelton*, F. Stuart Foster, Paul A. Dayton, with permission of Springer.

Superharmonic imaging produced significantly better CTR than multi-pulse imaging, with $p = 5 \times 10^{-10}$ using a paired t-test on pooled data from all microbubble doses tested. Experiments also included comparisons across 3 different bolus doses of targeted microbubbles at low concentrations. The three bolus doses tested were 7.6×10^6, 1.3×10^7, and 2.5×10^7 microbubbles, with the highest dose being comparable to numbers reported in the literature for molecular imaging with contrast-specific pulse sequences in rats (weighing approximately 200 grams). Figure 7.7 shows boxplots of

the contrast enhancement for each of the 3 contrast doses.

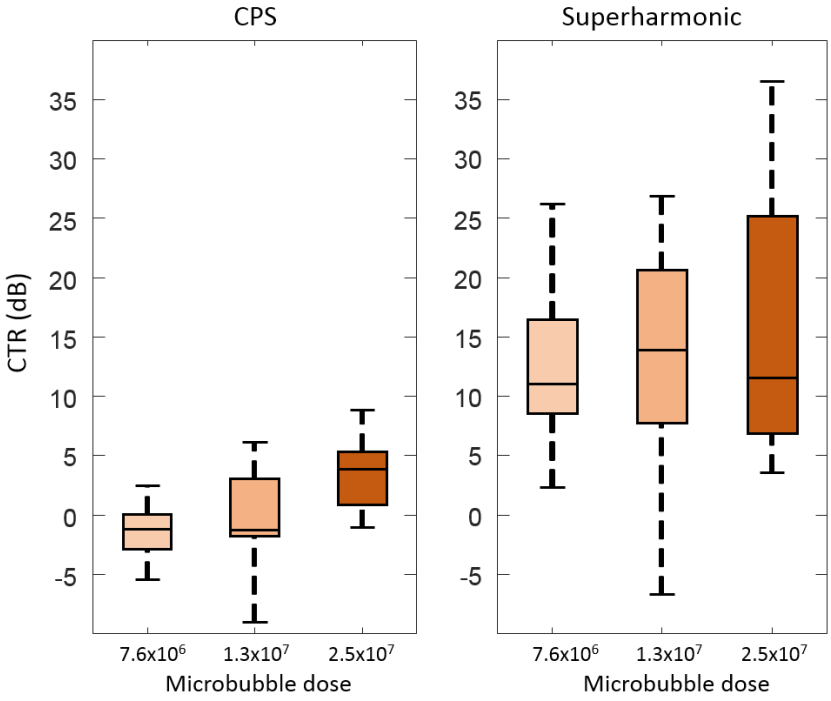

Figure 7.7: CTR at 3 different doses of microbubbles for multi-pulse contrast imaging in CPS mode (left) and superharmonic molecular imaging (right).
Adapted from Molecular Imaging and Biology, Assessment of Molecular Acoustic Angiography for Combined Microvascular and Molecular Imaging in Preclinical Tumor Models, Volume 19, Issue 2, 2016, pages 194-202, Brooks D. Lindsey*, Sarah E. Shelton*, F. Stuart Foster, Paul A. Dayton, with permission of Springer.

At each of the 3 contrast doses tested, superharmonic imaging had higher contrast enhancement than conventional multi-pulse microbubble imaging. Additonally, dose significantly influenced contrast enhancement in both imaging techniques, and ANOVA analysis rejected the null hypothesis that enhancement was equal for all contrast doses, with $p < 0.01$ for both detection techniques. Tukey Honest Significant difference post-hoc analysis was then used to compare the 3 doses for each imaging imaging method. Results indicated that there was no significant difference between the 7.6×10^6 and 1.3×10^7 doses for either multi-pulse (CPS) imaging or superharmonic imaging, but that the largest dose (2.5×10^7) resulted in significantly increased the CTR for both

techniques ($p < 0.01$).

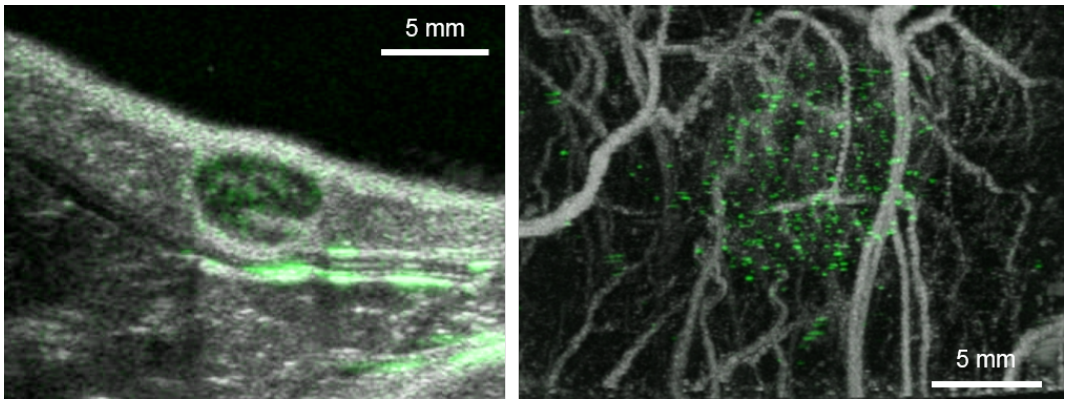

Figure 7.8: The image on the left shows a frame of B-mode and VEGFR2 molucular data (green) acquired using multi-pulse molecular imaging. The image on the right is a maximum intensity projection of the acoustic angiography vascular image and the superharmonic molecuar image (green).

The benefit of superharmonic molecular imaging is not restricted to the high contrast to tissue ratios achieved using this technique. The other benefits are the high resolution made possible due to the high frequency received signals from microbubble superharmonics and the ability to pair it with acoustic angiography images of vasculature using untargeted, freely flowing microbubbles, as shown in figure 7.8. Conventional molecular images are often overlaid on B-mode images for anatomical reference using the tissue images, and this is also possible for superharmonic molecular images by also acquiring B-mode images with the high frequency transducer before or after acquiring the molecular image. However, the molecular images can also be combined with vascular images by performing acoustic angiography imaging with untargeted microbubbles after completing the molecular imaging. Therefore, not only is anatomical reference possible, but also reference to the underlying vascular structure, resolvable to approximately 100-150 μm. Figure 7.9 shows overlaid images of molecular imaging with the

cyclic RGD microbubbles, (binding to the $\alpha_v\beta_3$ integrin) B-mode, and acoustic angiography images.

The advantage of combining molecular and vascular imaging is the ability to analyze the relationship between markers of biological processes such as angiogenesis to visible vascular morphology. Since ultrasound molecular imaging utilizes endothelial markers of disease, simultaneously observing the geometry of the vessels could provide additional information in pathologies involving the vasculature. Therefore, properties of the vascular morphology were compared with patterns in the molecular imaging.

First, vessel diameters were compared to the prevalence of targeting the distribution of distances between resolvable vessels and targeting sites. All targeting occurs within vessels because microbubbles are micron-sized, intra-vascular agents. However, the resolution limit of acoustic angiography images is approximately 100-150 μm, and targeting can occur in vessels smaller than this. We are able to detect these occurrences of targeting in sub-resolution vasculature, but are unable to resolve the structure of the individual vessels in which targeting occurred.

The majority of targeting sites (>50%) were located within 50 μm of a resolvable vessel, as seen in figure 7.10, with the trend showing progressively fewer targeting sites at larger distances from resolvable vessels. The second histogram in figure 7.10 displays the mean diameter of the vessels closest to each targeting site. The diameters shown in the histogram are the mean of the 5 vessels closest to each targeting site in order to obtain a more representative sample of the vessels located near targeting sites. Several targeting sites may be closest to a single vessel, so a small sample of the 5 closest vessels was used instead of the single closest vessel.

Images of microbubbles targeted to VEGFR2 and P- and E-selectin were used to compare targeting locations to vascular tortuosity. Distances between vessels and targeting sites were calculated and compared to the vessel tortuosity, in order to test the

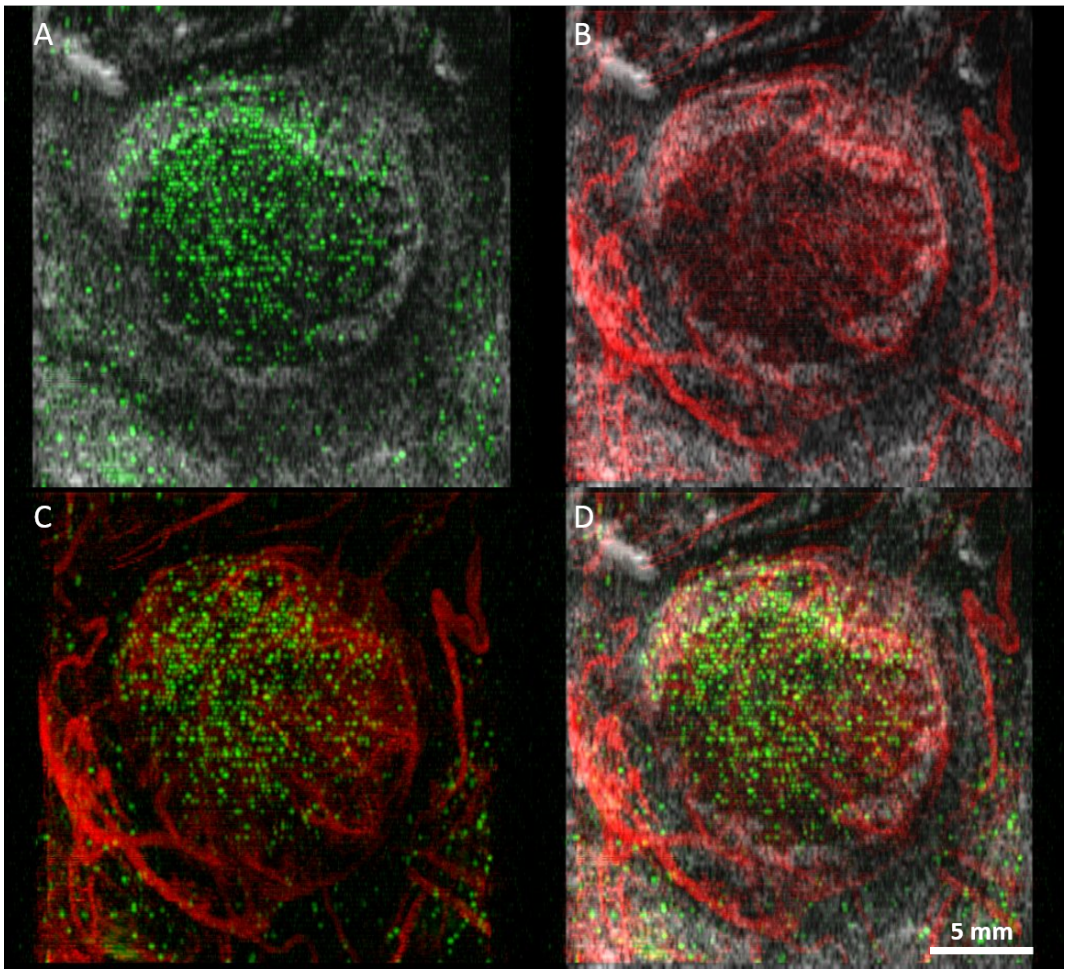

Figure 7.9: Panel A shows the maximum intensity projection of a superharmonic molecular imaging (green) overlaid on a slice of the B-mode image (gray), in the coronal plane. Panel B instead combines the B-mode frame with the maximum intensity projection of the acoustic angiography vascular image (red). Panel C combines the molecular and vascular maximum intensity projections, and panel D combines all 3 images. Molecular targeting used a microbubble targeted to the $\alpha_v\beta_3$ integrin.

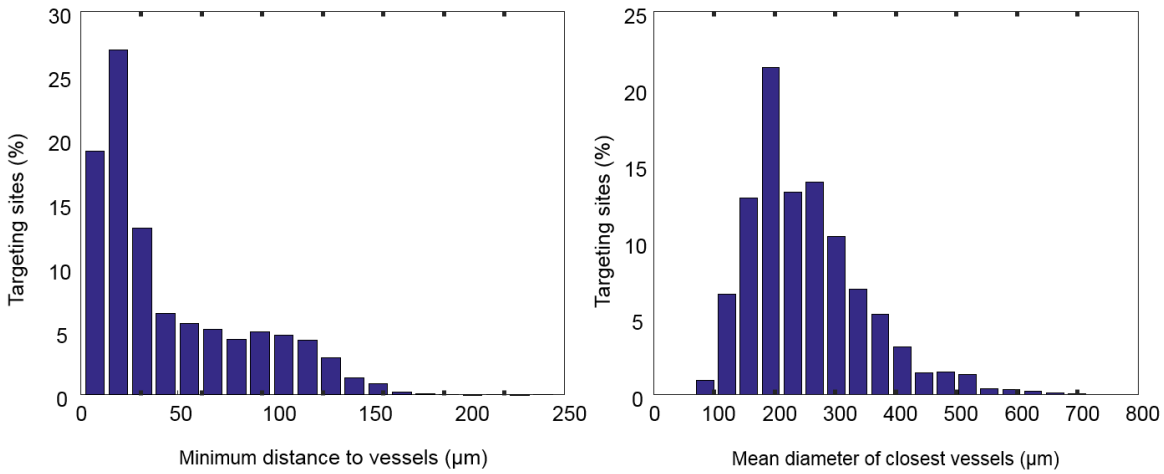

Figure 7.10: The histogram on the left shows the distances between targeting sites and the closest vessels. The histogram on the right shows the mean diameter of the 5 closest vessels to each targeting site.
Reprinted from Ultrasound in Medicine & Biology, Volume 42, Issue 3, Sarah E. Shelton*, Brooks D. Lindsey*, James K. Tsuruta, F. Stuart Foster, Paul A. Dayton, Molecular Acoustic Angiography: A New Technique for High-Resolution Superharmonic Ultrasound Molecular Imaging, Pages 769-781, ©2016, with permission from Elsevier.

hypothesis that targeting is more prevalent in tortuous vasculature. The boxplots in figure 7.11 support this hypothesis, although the difference in tortuosity between vasculature located within 50 μm of targeting sites is not much greater than that of more distant vasculature (300-400 μm away). However, the overall trend shows decreasing tortuosity with increasing distance from both VEGFR2 and selectin targeting sites.

Another study using ultrasound molecular imaging showed more targeting for selectin-targeted contrast than for VEGFR2-targeted microbubbles in a mouse model of colon adenocarcinoma [204], but we were unable to show significant differences between targeting levels of these two markers across the animals for the sample sizes used here (VEGFR2: N=14, Selectin: N=5). Figure 7.12 shows maximum intensity projections of acoustic angiography images using untargeted microbubbles (gray) with VEGFR2 (green) or selectin (red) targeted microbubbles, and the combination of all 3 images.

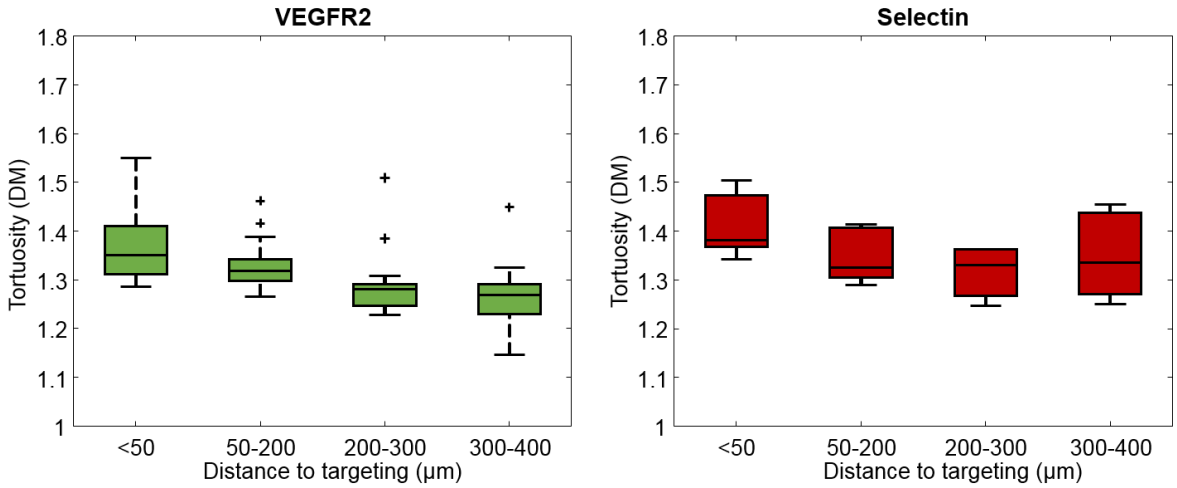

Figure 7.11: Tukey boxplots relating vascular tortuosity and distance between vessels and targeting sites: a. VEGFR2 (n = 14 animals) and b. Selectin (5 animals). Reprinted from Molecular Imaging and Biology, Assessment of Molecular Acoustic Angiography for Combined Microvascular and Molecular Imaging in Preclinical Tumor Models, Volume 19, Issue 2, 2016, pages 194-202, Brooks D. Lindsey*, Sarah E. Shelton*, F. Stuart Foster, Paul A. Dayton, with permission of Springer.

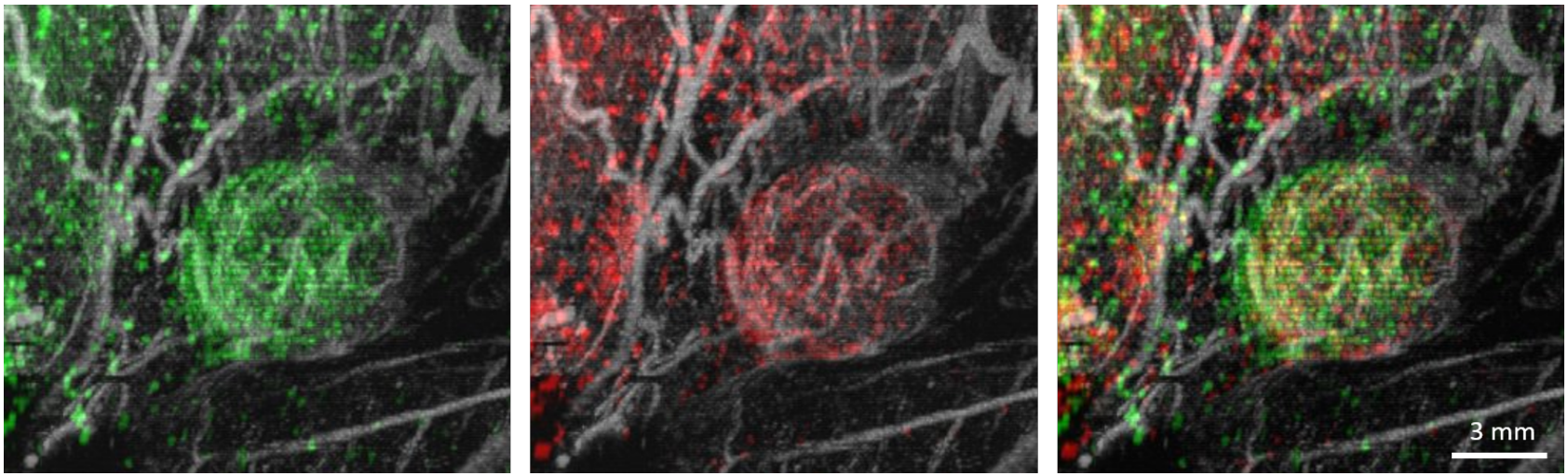

Figure 7.12: VEGFR2 targeting (shown in green) and P- and E-selectin targeting (shown in red), overlaid on maximum intensity projection of the vascular acoustic angiography image (shown in gray), acquired during infusion of untargeted microbubbles.

7.4 DISCUSSION

The combination of molecular and anatomical imaging has been shown to improve tumor diagnosis and localization in other clinical imaging modalities [205–210]. While ultrasound molecular images are often combined with B-mode images of tissue, molecular acoustic angiography allows molecular images to be overlaid on images of vasculature with high contrast and resolution. The combination of molecular and angiographic imaging allows us to relate molecular expression of endothelial markers and vascular geometry for the first time.

Before combining molecular and acoustic angiography imaging, we began by establishing the feasibility of superharmonic molecular imaging and optimizing acquisition. Because the production of superharmonic response from microbubbles requires sufficient pressures to induce shrinking or breaking, it is a semi-destructive contrast imaging technique [146]. Therefore, effective superharmonic molecular imaging required the balance of transmitting enough pressure at low frequency (4 MHz) to produce microbubble disruption, while simultaneously minimizing the amount of disruption occurring in microbubbles located outside the focus of the high frequency receive. The line spacing of the 2D imaging performed on the Vevo 770 described in this work is approximately 43 μm at the focus, which indicates that microbubbles in the focus could be disrupted and even destroyed by an adjacent, off-axis transmit event before they can be detected if too high a pressure is used. As a result, selection of the incident pressure and beam spacing is important for molecular imaging where microbubbles are stationary and no contrast replenishment is occurring.

We found that pressures of 500 kPa *in vitro* and 1200 kPa *in vivo* produced excellent contrast to tissue ratios (strong microbubble responses), without diminishing the response of adjacent lines. However, these pressures did destroy microbubbles over subsequent pulses and we observed the contrast signal decreasing over 100 frames *in*

vitro and decrease to approximately the noise floor after only 3-4 frames *in vivo*. These results also show that lower pressures can be used to preserve contrast intensity over a greater number of frames, but at the expense of contrast enhancement. Figure 7.2 suggested that while the contrast intensity of the 500 kPa transmit drops below that of the 350 kPa within the first 10 transmit pulses, the initial contrast itensity is much higher, and thus the higher pressures perform better for imaging, especially for *in vivo* imaging of very low concentrations of contrast.

As expected, larger microbubbles did increase the intensity of the superharmonic response of the microbubbles, but it did not significantly prolong the lifetime of useful contrast signal, as seen in figure 7.5. This indicates that the pressure selected for imaging *in vivo* (1200 kPa) is likely causing the majority of microbubbles within the field of view to rupture during the first transmit event. Therefore, this work reinforces the results of previous studies, which found that the highest contrast to tissue ratios occur with microbubble rupture [146].

In comparison to traditional multi-pulse molecular imaging implemented on a Siemens Sequoia in Cadence Pulse Sequence mode, molecular superharmonic imaging is at least as sensitive to low concentrations of targeted contrast agents, and produced higher contrast to tissue ratios at each of the 3 doses tested. There have been concerns that superharmonic imaging may not be as sensitive to contrast as multi-pulse non-linear imaging methods at lower frequency because the amplitude of the high frequency superharmonic signals is lower than the fundamental or first harmonic. However, there is much less tissue artifact in the higher superharmonic range than occurs for multi-pulse imaging at lower frequencies. We previously showed that transmit parameters which produce minimal tissue artifact are best for acoustic angiography imaging, and produce contrast images with much higher CTR than multi-pulse contrast imaging [147, 150].

This chapter described superharmonic molecular imaging with microbubbles targeted to the $\alpha_v\beta_3$ integrin, vascular endothelial growth factor receptor 2 (VEGFR2), and P- and E-selectin [150, 211]. We observed that the majority of targeting sites were located within vessels resolvable with acoustic angiography (at least 100 μm in diameter), or less than 50 μm from a resolvable vessel (see figure 7.10). Additionally, the targeting tended to occur in small vessels, and the histogram in figure 7.10 shows that most of the targeting occurred in the smallest resolvable vessels. It is likely that the endothlial markers tested in this study are likely to be most highly expressed in small vasculature because they are molecules associated especially with angiogenesis, and also inflammation. Sprouting occurs in small caliber vessels, so it is expected that high levels of targeting of any markers of angiogenesis would be detected in microvasculature. However, we are unable to exclude the physical factors that may also influence preferential targeting in small vessels as well. The geometry of microvasculature makes contact between micrometer sized microbubbles and the vascular wall more likely. Low blood velocity and shear may also contribute to preferential binding of targeted microbubbles in small vasculature. In the future, studies combining superharmonic molecular imaging and methods designed to estimate relative flow rates in acoustic angiography images could contribute to the relative importance of biological and physical factors in the correlation between targeting and vessel diameter [151].

Combining molecular imaging and acoustic angiography imaging also allows us to relate expression of these molecular markers to vascular tortuosity by segmenting the vasculature visible in acoustic angiography images and quantifying tortuosity. Figure 7.13 shows segmented vasculature from one of these tumors in panel a, and with a colormap expressing tortuosity using the distance metric in panel b. We can combine these representations of vascular morphology to investigate relationships between molecular targeting and tortuosity, and panels c and d show targeting data overlaid

on the tortuosity renderings, with VEGFR2 targeting shown in green in panel c and P- and E-selectin targeting in blue in panel d. The distances between these vessels and targeting locations were calculated and the tortuosity minimum distance between each vessel and targeting site was recorded. This data resulted in figure 7.11 which shows that higher tortuosity vasculature is located closer to a molecular targeting site for both VEGFR2 and selectin targeted microbubbles.

While, the association between VEGFR2 and tortuosity is expected due to the features of tumor angiogenesis discussed in chapter 1, P- and E-selectin are commonly thought of as markers of inflammation in ultrasound molecular imaging [198,212]. However, they are also related to tumor progression and metastasis through a number of biological pathways [213–218]. Additionally, selectins are also involved in angiogenesis, both through interactions with VEGF and independently [219–224]. E-selectin can induce angiogenesis in the cornea, and inhibiting E-selectin prevents angiogenesis in *in vitro* assays [219, 220]. In a P-selectin knockout mouse model, the knockout mice had lower capillary density than wild type mice, indicating that P-selectin plays a role in angiogenesis after ischemia [222]. Both E- and P-selectin are also related to VEGF through leukocytes, expression of gene regulation, and through TNF-α signaling [221, 222, 224]. While the relationships between molecular targeting and tortuosity are not strong, the data presented here suggest that vasculature appearing tortuous in acoustic angiography images is likely to have relatively higher levels of expression of VEGFR2 and P- and E-selectin. Future work should repeat these studies in mice to permit immunohistochemical (IHC) analysis of endothelial expression of these markers using validated antibodies, as IHC analysis of fixed tissue from this rat model of fibrosarcoma was unable to produce satisfactory staining of VEGFR2, E-selectin, or P-selectin.

The combination of vascular imaging, tortuosity analysis, and molecular imaging

opens the door to countless new hypotheses relating vascular morphology and targeting in disease. Further studies are required to determine if differences in targeting intensity (such as comparing VEGFR2 images to selectin images) recapitulate true differences in the expression of these proteins, or if other factors such as ligand affinity contribute to the differences observed. Several other interesting endothelial adhesion proteins could be targeted such as intercellular adhesion molecule 1 (ICAM-1), vascular cell adhesion molecule 1 (VCAM-1), and several members of the integrin family. Spatial analysis of tortuosity and molecular targeting could be useful for delineating tumor margins, or even predicting response to therapy. The experiments and results present here are only the beginning of a new way to relate endothelial biomarkers and vascular remodeling.

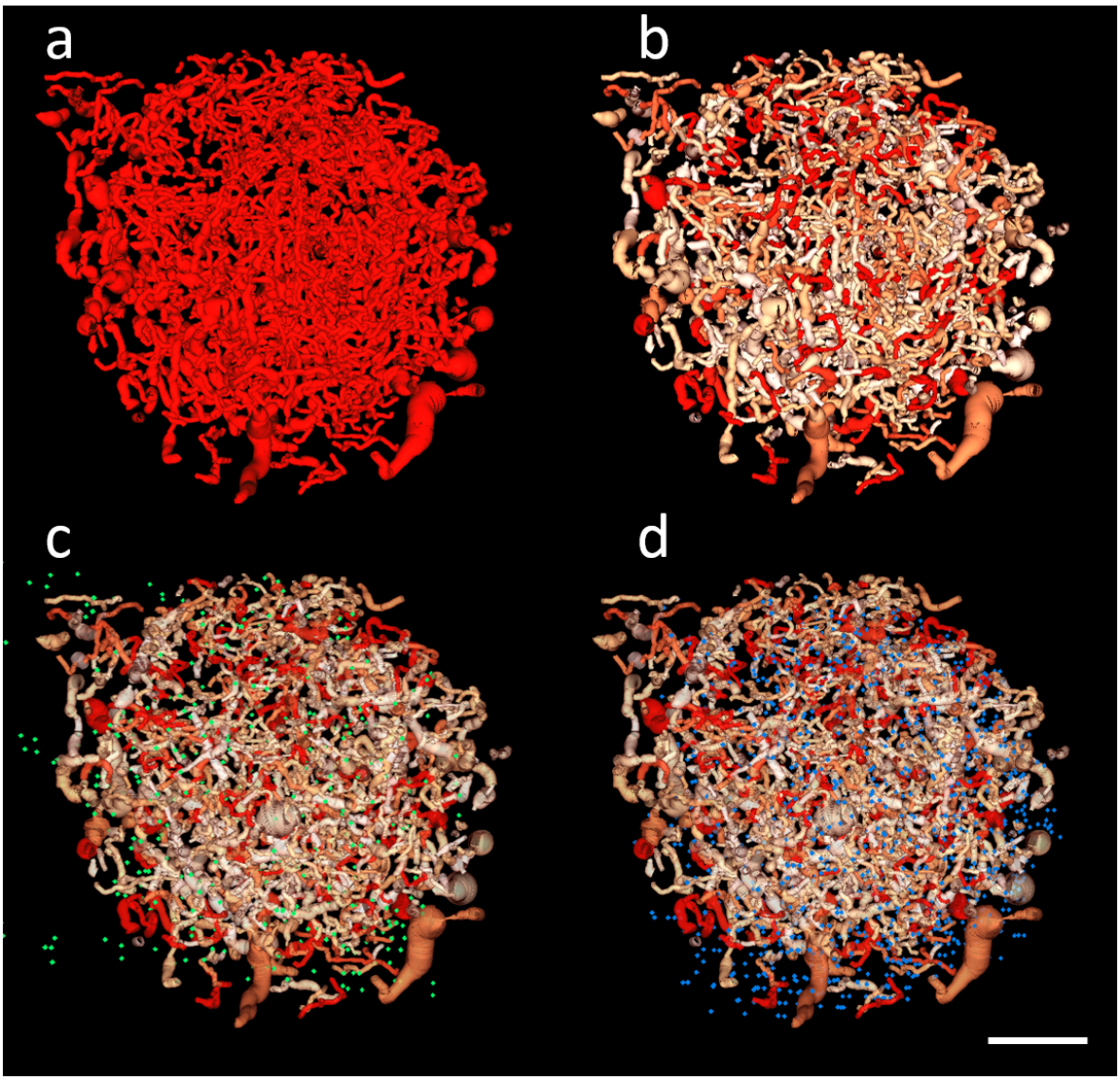

Figure 7.13: Segmented imaging volume containing (a) microvascular imaging data within the tumor, (b) microvascular imaging data with color-coded tortuosity (increasing red indicates increasing tortuosity), (c) microvascular imaging data with color-coded tortuosity and VEGFR2 targeting data (green), and (d) microvascular imaging data with color-coded tortuosity and selectin targeting data (blue). Scale bar represents 2 mm.

APPENDIX A

CLINICAL IMAGING

A.1 INTRODUCTION

Nearly 250,000 women were diagnosed with breast cancer in the United States in 2016, with over 40,000 deaths in the same year [225]. Currently, mammography is used to screen women over the age of 40 and has been shown to increase survival by about 20% [226, 227]. Based on mammographic results, the lesion is assigned a score from 1 to 6 according to the Breast Imaging Reporting and Data System (BI-RADS) [228]. For individuals with a suspicious mammogram (BI-RADS category 3-5), follow-up imaging with other approaches, including diagnostic mammography, breast tomosynthesis [229–231], magnetic resonance imaging [232, 233], and ultrasound [234], may be utilized to clarify the nature of the lesion. Lesions ultimately categorized as BI-RADS 4-5 have a high likelihood of malignancy and are directed toward biopsy or surgical excision.

Pathology results from more than 26,000 patients receiving breast biopsies indicate that 66.8% of the biopsies were benign, suggesting that many of these biopsies are unnecessary [235]. In addition, breast biopsies are known to yield false negatives at a

---

rate of about 2% [236], and many patients are subjected to repeated biopsies depending primarily on the physician's judgment [237]. About 10% of lesions require repeat biopsy, and only approximately 17% of these are malignant [238], suggesting many patients may be subjected to multiple unnecessary biopsies. If a non-invasive, non-ionizing radiation imaging approach could demonstrate sufficient specificity, it might be possible to reduce the rate of unnecessary biopsies, sparing patients pain and anxiety [239].

In order for solid tumors to grow beyond a certain size (typically ≈2 mm), new vessels must form (angiogenesis) [174, 240]. In breast lesions in particular, elevated microvessel density is correlated with the occurrence of metastases and thus has been identified as a potential prognostic indicator, as microvessel density in the region of highest neovascularization has been shown to predict overall and relapse-free survival [241, 242]. Several non-invasive imaging techniques have sought to utilize this knowledge for diagnosis, including magnetic resonance imaging (MRI) [243], computed tomography (CT) [244], color Doppler ultrasound [245], and conventional contrast-enhanced ultrasound imaging [246–250]. However, none of these approaches have yet demonstrated the ability to improve diagnostic accuracy or reduce the need for biopsy in clinical studies.

From an imaging perspective, a key challenge is the ability to resolve the microvessels formed early in tumor angiogenesis, as the vessels observed in histological evaluation of invasive carcinomas typically have diameters <100 μm [251]. In order to form vascular or "angiographic" images, many imaging techniques utilize exogenous contrast agents to image vascular structures in the breast, i.e. iodine in CT [244], gadolinium in MRI [252], and perfluorocarbon-filled microbubbles in contrast-enhanced ultrasound [248]. Even with the use of contrast agents, the ability to both detect and resolve the microvessels of clinical interest remains challenging, as typical spatial resolutions for

clinical imaging systems are ≈700 m for MRI [253], ≈600 m for CT [254], and 300-500 m for conventional ultrasound [255]. Special small animal imaging systems have demonstrated higher resolutions in all modalities, including as high as 100-200 m in MRI [256], as high as 40 m in CT (for scan times >50 min) [257], and 30-200 m for high-frequency ultrasound [258, 259].

Contrast-enhanced ultrasound (CEUS) imaging has been performed in the breast for tumor characterization and diagnosis. Ricci characterized CEUS enhancement as having equal accuracy as MRI for breast cancer diagnosis in humans [260]. Subsequent studies have described contrast enhancement and wash-out patterns, but contrast enhanced ultrasound imaging is still not routine in the breast [261, 262]. Ultrasound molecular imaging also shows promise as a clinical indicator of malignancy. Microbubbles targeted to vascular endothelial growth factor receptor (VEGFR2) have been validated in model systems [263, 264], and it was recently shown in humans that higher targeting was observed in malignant lesions than in benign, and that targeting intensity was related to the level of VEGFR2 expression as measured with immunohistochemistry [265].

We have recently developed a new contrast-enhanced ultrasound microvascular imaging approach based on the superharmonic signal produced by microbubbles. In this approach microbubbles are excited using a low frequency (<6 MHz) pulse and images are formed from high frequency (>20 MHz) signals produced by microbubbles. Resulting images have higher contrast-to-tissue ratio (CTR, ≈25 dB) and spatial resolution (100-200 μm) than conventional contrast-enhanced ultrasound [159]. Because these images show vascular structures alone, we call this technique acoustic angiography due to the similarity to other forms of angiographic imaging, i.e. computed tomography angiography, magnetic resonance angiography [266]. In addition, these images can be segmented and vessel tortuosity computed using previously-established

quantitative metrics [267,268]. This is potentially useful because previous studies using intravital microscopy in animal models have shown that tumor vascular remodeling occurs when tumors consist of <100 cells [269], providing another potential quantitative metric beyond microvessel density. In imaging a genetically-engineered mouse model of ductal carcinoma, quantifying vessel tortuosity has enabled distinguishing 2-3 mm tumors from healthy tissue [148].

In this work, we present the first translation of acoustic angiography imaging to humans. Imaging volumes have been acquired of the vasculature in the wrist of healthy volunteers, as well as in the breast of both healthy volunteers and patients. Due to the high spatial resolution of this technique comparable to that of small animal CT and MRI it represents a potential tool for quantifying the high microvascular density associated with invasive tumors in the breast. Contrast-enhanced ultrasound imaging utilizing the superharmonic response of microbubbles has been described in in vitro and in vivo studies, but clinical studies in humans are limited, and were restricted to examinations of the heart at low frequencies (0.8/2.8 MHz). While CEUS allows imaging of tissue perfusion and power Doppler allows imaging of individual vessels at these spatial scales, acoustic angiography reveals vascular morphology and enables quantification of vessel tortuosity, a marker of malignancy.

A.2 METHODS

This study was approved by the Institutional Review Board (IRB) of the University of North Carolina at Chapel Hill, and all participants were enrolled after voluntary written informed consent. In the first phase of the study, we enrolled healthy male and female volunteers for initial imaging in the wrist, hand, and breast. Images from these subjects were used to assess the feasibility of superharmonic contrast imaging in vivo and determine achievable resolution. A total of 6 individuals volunteered for wrist

and hand imaging (3 males, 3 females), and 6 females volunteered for breast imaging. The second phase of the study included a patient population of women with suspicious breast lesions (BI-RADS 4 and 5) who were scheduled to receive a breast biopsy at UNC Hospital. To date, 11 pre-biopsy patients have been imaged in this trial, with enrollment ongoing.

Ten healthy volunteers received an intravenous bolus of 10 μL/kg of Definity (Lantheus Medical Imaging, Billerica, MA) followed by sterile saline, in accordance with the prescribing information, and 2 volunteers received 20 μL/kg. Pre-biopsy participants also received a bolus of Definity at either 10 μL/kg (n=6) or 20 μL/kg (n=5).

Imaging was performed with a VisualSonics Vevo 770 ultrasound scanner and a modified RMV707 transducer (FUJIFILM VisualSonics Inc., Toronto, ON, Canada). The modified transducer has an additional annular low frequency element (4 MHz center frequency) confocal to the 707 transducer (30 MHz center frequency) in order to allow dual-frequency imaging of microbubble superharmonics by transmitting with the low frequency element and receiving with the high frequency element [143]. Dual-frequency imaging was conducted at a mechanical index of 0.6 (non-derated), which is within the range suggested for safe use with Definity (up to 0.8).

Three-dimensional image volumes were acquired using a linear motion stage, which translated the transducer across the surface of the skin with a step size of 0.2 mm. This motion stage (FUJIFILM VisualSonics Inc., Toronto, ON, Canada) was designed to operate fixed to a platform for small animal imaging, so to enable more flexible positioning for human patients, we mounted the motion stage to an adjustable arm (Photo Variable Friction Arm, Manfrotto, South Upper Saddle River, NJ), supported by a surgical microscope stand. Each image slice in a 3D volume was acquired at a rate of 3 frames per second, with a 3D volume being acquired in approximately 1-2 minutes, depending on the length of the scan (20-30 mm). The transducer (attached to

the motion stage) was positioned by a radiologist and then locked into place to acquire 3-D scans.

De-identified image data was exported for offline analysis and image reconstruction in ImageJ and the VisualSonics Vevo770 imaging software. Volumetric data sets were rendered using maximum intensity projections to display 3-D images in 2-D. Linear interpolation was used to compensate for larger spacing in the elevation direction than the axial-lateral dimension when reconstructing images in orientations other than the acquisition plane.

A.3 RESULTS

This study has demonstrated the feasibility of superharmonic acoustic angiography in human subjects for the first time. We were able to visualize contrast signal and resolve individual vessels using the standard clinical dose of Definity microbubbles, 10 μL/kg. Additionally, we also tested twice the standard dose of Definity, 20 μL/kg, in 5 patients and 2 healthy volunteers and observed stronger contrast signal at the higher dose. Figure A.1 shows examples of acquired images of the wrists of 2 different healthy volunteers. These images are maximum intensity projections of the 3-D image volumes and show the radial artery and the branch of the smaller palmar radiocarpal artery. Both images were acquired immediately following a bolus of 10 μL/kg of contrast. On the left (figure A.1A), an extent of approximately 2.5 cm of the radial artery is shown, while the image on the right (A.1B) is enlarged to show detail from a different subject. The diameters of the radial arteries visible in these images was measured to be between 1.5 and 2 mm wide, consistent with the range observed in other measurements of radial artery size [270].

The images in Figure A.2 were acquired in healthy volunteers and show several branching structures and vasculature of different sizes in normal breast tissue. Both

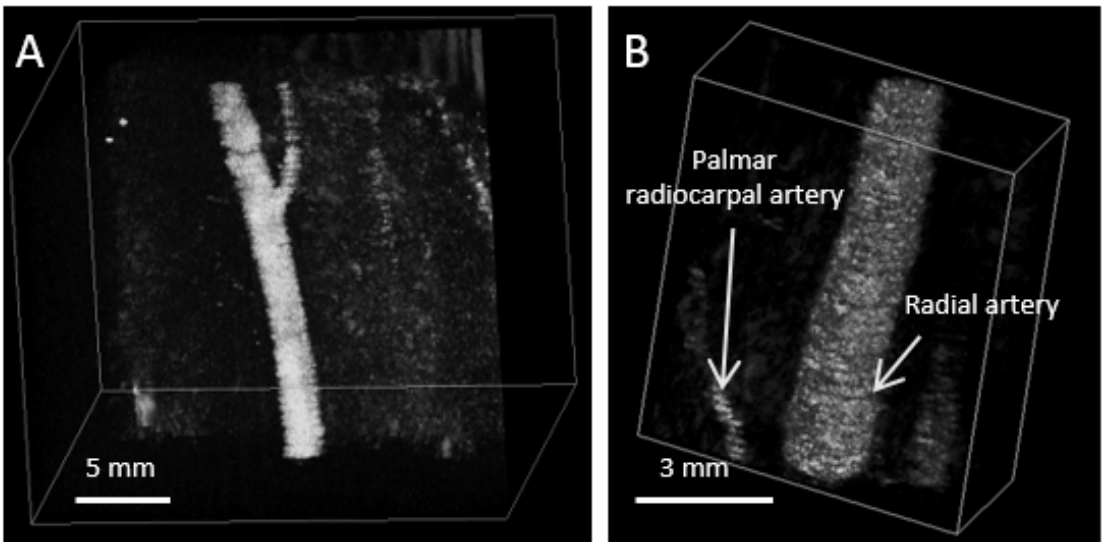

Figure A.1: Figure 1. Maximum intensity projections of "acoustic angiography" images acquired in the wrists of volunteers administered a bolus of 10 μL/kg of Definity.

of these subjects received the 10 μL/kg contrast dose. Additionally, these images also reveal one of the limitations of the confocal, single-element transducer design: the limited depth of field. The transducer elements are focused at a depth of 1.3 cm, and the high frequency element has a depth of field of 2.2 mm, as reported by the manufacturer. In practice, these images show that region of tissue where contrast is visible in dual-frequency imaging spans approximately 8 mm, centered at the focus. In Figure A.2A, the vessels seem to drop off as they plunge deeper into the tissue, and in A.2B, the deep vessel that crosses the center of the image has a weaker signal than the nearby vessels despite the fact that they are similar in size.

Figure A.3 shows a maximum intensity projection with several vessel diameters measured and annotated on the image. This image is the same data as seen in Figure A.2B, reconstructed with a maximum intensity projection at a slightly different angle. In Figure A.3, we see small vessels measuring 0.17 mm wide, with low image contrast. However, slightly larger 0.2 mm vessels have higher contrast, with the largest vessels between 0.43 and 1.24 mm being the easiest to visualize.

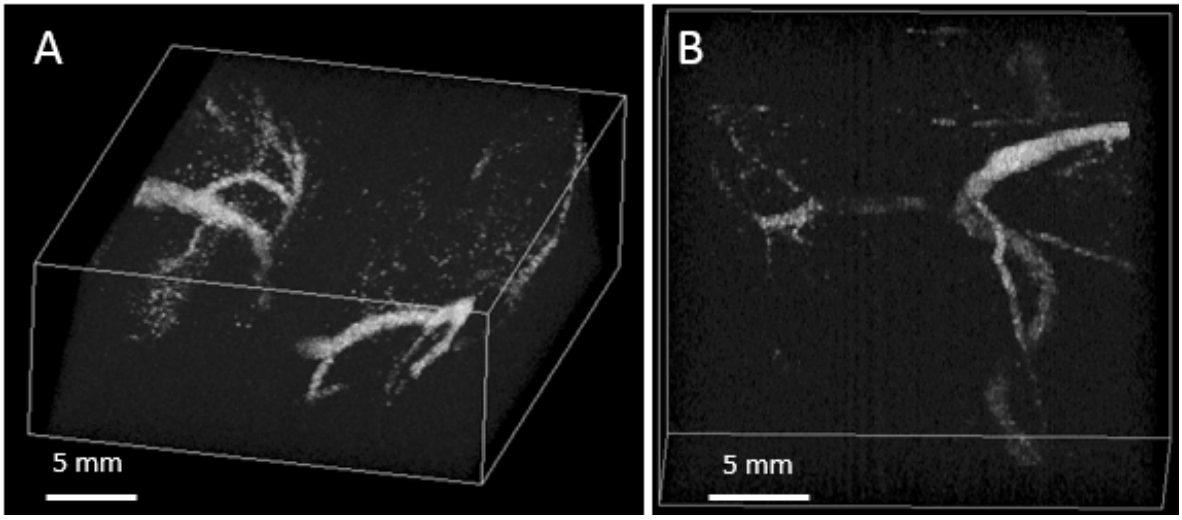

Figure A.2: Figure 2. Images of normal breast vasculature in healthy volunteers who received a 10 L/kg bolus.

While the maximum intensity projections of the 3-D data are useful for resolving the structure of vascular morphology throughout the tissue, there is additional information available in individual image frames. Figure A.4 includes images from a pre-biopsy patient who received 20 μL/kg of Definity. Figure A.4A is a maximum intensity projection showing large vessels branching as well as diffuse contrast signal from sub-resolution vasculature in the surrounding tissue. Figure A.4B is an enlarged view of the main branch, also shown as a maximum intensity projection. Figure A.4C, however, is a single frame from the branching region showing that multiple small vessels are resolvable in the individual frame, but less apparent in the projected data. Therefore, individual frames of acoustic angiography images could be used to understand the relative positions and connections between sub-millimeter vessels.

Comparing the breast images shown in Figure A.5 to the wrist images in Figure A.1, we can see more artifact due to respiration in Figure A.5. The borders of the vessels in Figure A.5 are less smooth than those seen in Figure A.1 due to tissue motion. However, in these examples, respiration motion on the order of 0.3 to 0.5 mm (Figure A.4B, Figure A.5B) is not large enough to obscure the overall morphology.

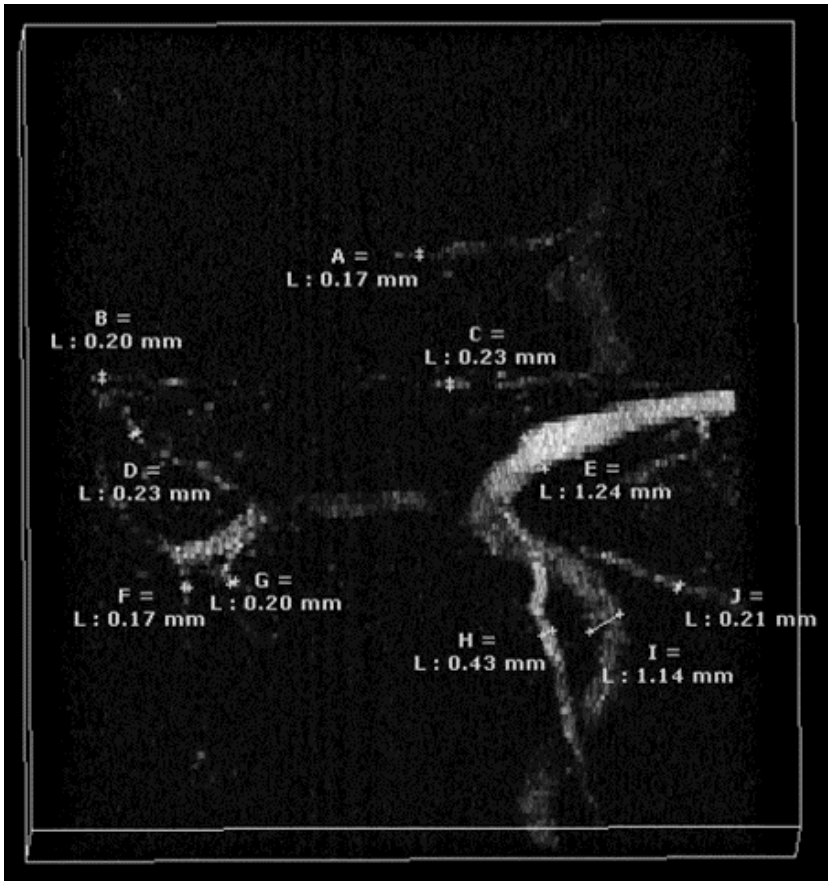

Figure A.3: Figure 3. A maximum intensity projection of breast vasculature from a healthy volunteer annotated with vessel diameters.

Additionally, we can perform motion correction by applying B-spline registration to consecutive frames in the image to produce smoothed images without altering the overall vessel morphology, as demonstrated in Figure A.6.

No serious adverse reactions to the contrast occurred. However, four participants reported mild events. One participant (out of 16) who received 10 μL/kg reported transient back and chest discomfort, and 3 participants (out of 7) who received a bolus of 20 μL/kg experienced mild, transient flushing with no significant changes in vital signs. Although these mild reactions were anticipated in the package insert for Definity, the incidence was higher than expected in our small sample size. It is unknown if this might have been due to an issue with the contrast agent lot, the bolus administration

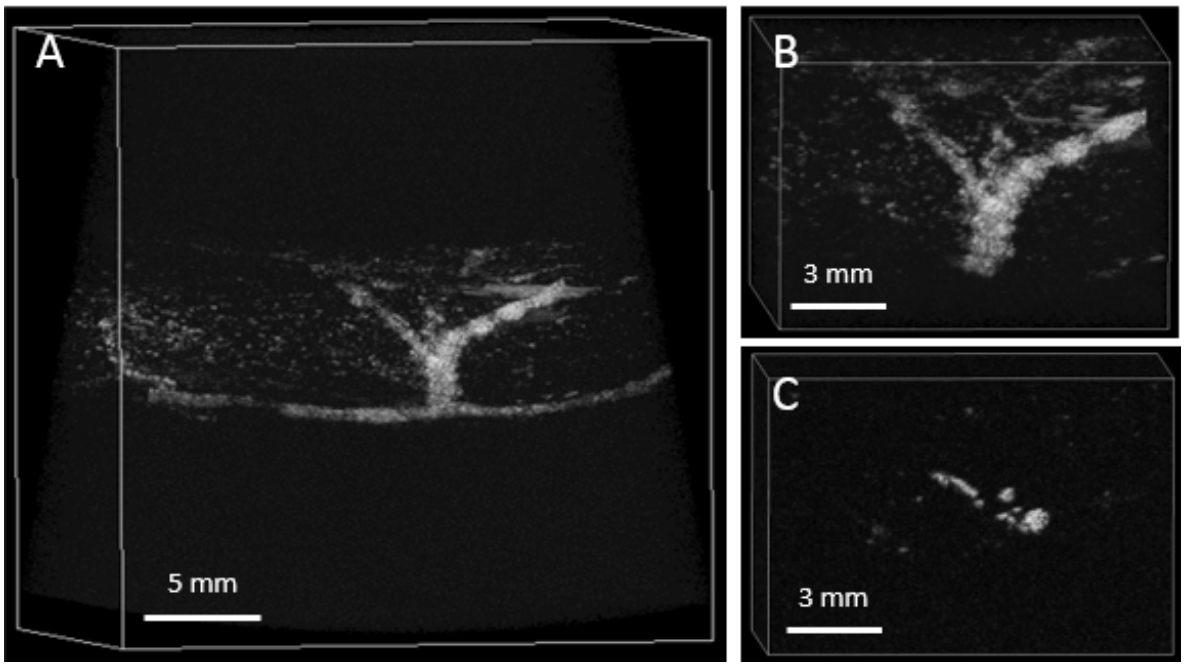

Figure A.4: Figure 4. Images from a pre-biopsy patient who received a bolus of 20 μL/kg of contrast. 4A shows a maximum intensity projection of the image volume, while 4B is enlarged to show detail at the main branching location. 4C is a single frame at the same scale as 4B, showing several distinct vessels in the branching region.

rate, a random occurrence in our patient population, or some other variable. It is worth noting that other groups have used the same contrast agent at the same dose without any reported adverse reactions [249]. As the acoustic angiography imaging approach uses standard clinical imaging parameters (4 MHz, MI = 0.6), it seems unlikely that observed adverse reactions were related to the imaging technique itself.

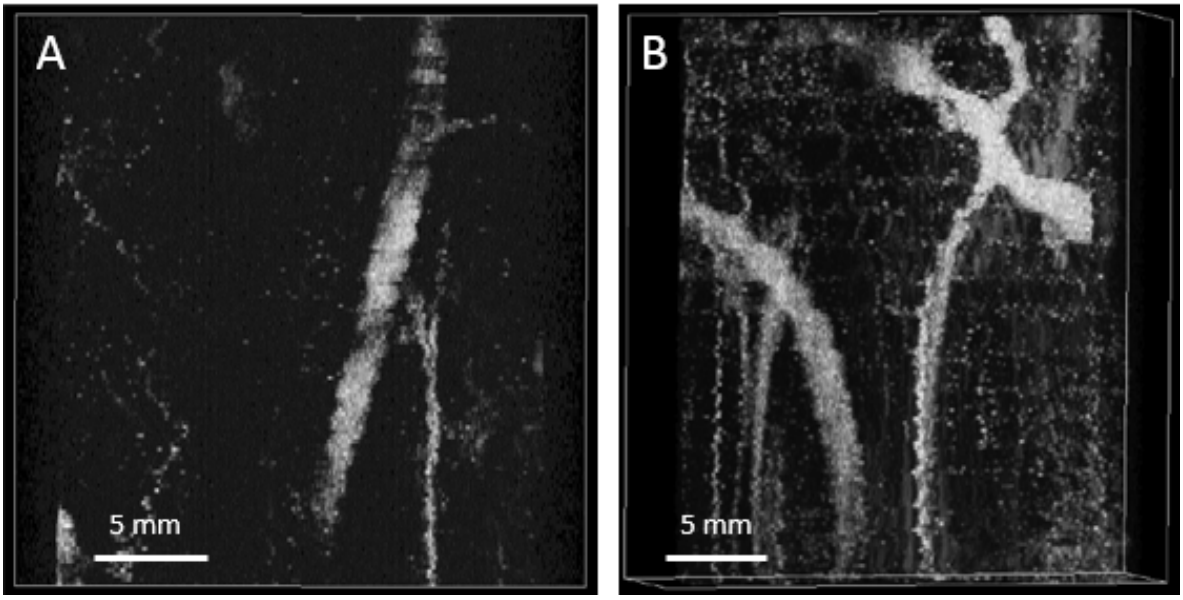

Figure A.5: Figure 5: Images from pre-biopsy patients showing vasculature ranging in size from approximately 0.2 to 2 mm in diameter. Respiration motion artifacts are visible, making the borders of the vessels appear serrated. Subjects received 10 μL/kg of Definity.

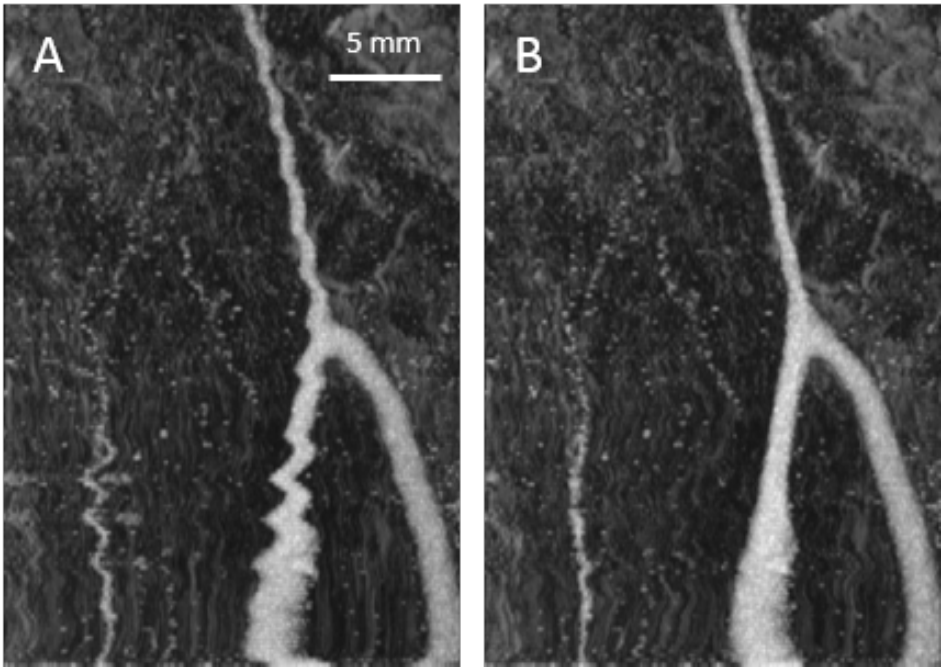

Figure A.6: Figure 6: Image from a pre-biopsy patient who received 10 μL/kg of Definity. 6A shows the original image, clearly subject to respiration motion. 6B shows the smoothed image using B-spline registration to minimize motion artifacts.

A.4 DISCUSSION

In this study, we only included lesions located within approximately 1.5 cm from the skin surface due to the limited depth of field provided by the fixed focus transducer. This prototype, confocal, single-element transducer has a lens with a fixed focus of 13 mm and an approximate field of view of 8 mm in dual-frequency contrast imaging mode. Both the field of view and frame rate might be improved by the development of a dual-frequency array. With a higher frame rate enabled by acquiring an entire imaging slice in real-time without mechanically sweeping the confocally-aligned transducer elements, motion artifacts could be minimized by acquiring the entire 3D image in single breath-hold ($\approx$10 sec) using a translation stage. There is also a clinical need to image lesions deeper than 1.5 cm. Though it is estimated that 30% of breast lesions are located within 1 cm of the skin surface, a larger imaging depth will be necessary to make superharmonic contrast imaging feasible relevant to a greater number of patients [271]. Acoustic angiography can be performed with greater depth of penetration by selecting a lower receive frequency, and we have demonstrated superharmonic contrast imaging as deep as 4 cm using an endoscopic transducer designed to transmit at 4 MHz and receive at 20 MHz [272]. Axial resolution at this frequency combination is expected to be better than 200 μm [159].

Of note, the sensitivity and spatial resolution of the current system used in this study allowed acquisition of images with vessels as small as 100-200 μm (Figure A.3), similar to the resolution provided by pre-clinical MRI and CT systems [256, 257, 273]. Improvements in sensitivity would require either improved transducer sensitivity or increased microbubble dose.

Super-resolution imaging techniques have demonstrated resolution below the diffraction limit, nearly at the capillary scale, using microbubble localization techniques [126–131]. However, super-resolution imaging has not yet been demonstrated in the

clinic and requires the acquisition of thousands to tens of thousands of images to create a single frame. Even with ultrafast plane-wave imaging, the acquisition time for a single frame is on the order of minutes in order to accumulate a sufficient number of microbubble positions to reconstruct microvascular structure with fine detail. Though superharmonic acoustic angiography cannot match the resolution scale promised by super-resolution imaging, microvessels approximately 100-200 μm can be imaged with a single transmit event, and a 3D image volume can be acquired in 1-2 minutes using a translation stage. Dual-frequency array transducers are expected to significantly improve acquisition time for acoustic angiography in the future.

Improving spatial resolution would require either a larger aperture (which would likely prove increasingly difficult to couple to the patient), or the use of a higher receiving frequency. Unfortunately, increasing the receiving frequency would result in a decrease in sensitivity, as the superharmonic signals used to form these images decrease in amplitude with increasing frequency [159], in addition to increasing attenuation, which would also decrease the depth of penetration. Nonetheless, if this technology could be utilized in conjunction with breast ultrasound, existing resolution and sensitivity may eventually prove sufficient for a diagnostic test with adequate specificity to preclude biopsy in lesions lacking vessels greater than approximately 150 μm in diameter. It is worth noting that this technology has demonstrated potential for use for imaging other shallow vasculature such as the carotid arteries for assessment of atherosclerotic disease.

A.5 ACKNOWLEDGEMENTS

Funding was provided by the National Institute of Health from R01CA170665S1, R01CA170665, F99CA212227, and F32EB018715. We would also like to acknowledge the contributions of Michele Vickers, Shanah Kirk, Terry Hartman, nursing support

from the UNC Clinical and Translational Research Center, and the cooperation of the physicians and staff of the Breast Imaging Division in the Department of Radiology. We also thank Samuel Gerber and Stephen Aylward (Kitware, Inc.) for their expert help with image registration. This imaging would not have been possible without the collaborative efforts of Dr. F. Stuart Foster, Mike Lee, Emmanuel Cherin, Chris Chaggares, and technical support from Visualsonics, Inc. P.A.D. declares that he is an inventor on a patent describing the dual-frequency imaging technology, and is a co-founder of SonoVol, Inc., a company which has licensed this technology.

BIBLIOGRAPHY

[1] N. Howlader, A. Noone, M. Krapcho, J. Garshell, N. Neyman, S. Altekruse, C. Kosary, M. Yu, J. Ruhl, Z. Tatalovich, H. Cho, A. Mariotto, D. Lewis, H. Chen, E. Feuer, and K. Cronin, "SEER cancer statistics review, 1975-2011," 2014.

[2] R. Haque, S. A. Ahmed, G. Inzhakova, J. Shi, C. Avila, J. Polikoff, L. Bernstein, S. M. Enger, and M. F. Press, "Impact of breast cancer subtypes and treatment on survival: an analysis spanning two decades," *Cancer Epidemiol Biomarkers Prev*, vol. 21, no. 10, pp. 1848–55, 2012.

[3] T. Sorlie, C. M. Perou, R. Tibshirani, T. Aas, S. Geisler, H. Johnsen, T. Hastie, M. B. Eisen, M. van de Rijn, S. S. Jeffrey, T. Thorsen, H. Quist, J. C. Matese, P. O. Brown, D. Botstein, P. E. Lonning, and A. L. Borresen-Dale, "Gene expression patterns of breast carcinomas distinguish tumor subclasses with clinical implications," *Proc Natl Acad Sci U S A*, vol. 98, no. 19, pp. 10869–74, 2001.

[4] R. Rouzier, C. M. Perou, W. F. Symmans, N. Ibrahim, M. Cristofanilli, K. Anderson, K. R. Hess, J. Stec, M. Ayers, P. Wagner, P. Morandi, C. Fan, I. Rabiul, J. S. Ross, G. N. Hortobagyi, and L. Pusztai, "Breast cancer molecular subtypes respond differently to preoperative chemotherapy," *Clin Cancer Res*, vol. 11, no. 16, pp. 5678–85, 2005.

[5] D. A. Berry, K. A. Cronin, S. K. Plevritis, D. G. Fryback, L. Clarke, M. Zelen, J. S. Mandelblatt, A. Y. Yakovlev, J. D. Habbema, E. J. Feuer, I. Cancer, and C. Surveillance Modeling Network, "Effect of screening and adjuvant therapy on mortality from breast cancer," *N Engl J Med*, vol. 353, no. 17, pp. 1784–92, 2005.

[6] A. Bleyer and H. G. Welch, "Effect of three decades of screening mammography on breast-cancer incidence," *N Engl J Med*, vol. 367, no. 21, pp. 1998–2005, 2012.

[7] T. Wu, R. H. Moore, E. A. Rafferty, and D. B. Kopans, "A comparison of reconstruction algorithms for breast tomosynthesis," *Medical Physics*, vol. 31, no. 9, pp. 2636–2647, 2004.

[8] E. D. Pisano, R. E. Hendrick, M. J. Yaffe, J. K. Baum, S. Acharyya, J. B. Cormack, L. A. Hanna, E. F. Conant, L. L. Fajardo, L. W. Bassett, C. J. D'Orsi, R. A. Jong, M. Rebner, A. N. Tosteson, C. A. Gatsonis, and D. I. Group, "Diagnostic accuracy of digital versus film mammography: exploratory analysis of selected population subgroups in DMIST," *Radiology*, vol. 246, no. 2, pp. 376–83, 2008.

[9] R. A. Hubbard, K. Kerlikowske, C. I. Flowers, B. C. Yankaskas, W. Zhu, and D. L. Miglioretti, "Cumulative probability of false-positive recall or biopsy recommendation after 10 years of screening mammography: a cohort study," *Ann Intern Med*, vol. 155, no. 8, pp. 481–92, 2011.

[10] H. G. Welch and H. J. Passow, "Quantifying the benefits and harms of screening mammography," *JAMA Intern Med*, vol. 174, no. 3, pp. 448–54, 2014.

[11] J. G. Elmore, M. B. Barton, V. M. Moceri, S. Polk, P. J. Arena, and S. W. Fletcher, "Ten-year risk of false positive screening mammograms and clinical breast examinations," *N Engl J Med*, vol. 338, no. 16, pp. 1089–96, 1998.

[12] R. J. Hooley, L. M. Scoutt, and L. E. Philpotts, "Breast ultrasonography: state of the art," *Radiology*, vol. 268, no. 3, pp. 642–59, 2013.

[13] E. Bullitt, M. Ewend, J. Vredenburgh, A. Friedman, W. Lin, K. Wilber, D. Zeng, S. R. Aylward, and D. Reardon, "Computerized assessment of vessel morphological changes during treatment of glioblastoma multiforme: report of a case imaged serially by MRA over four years," *Neuroimage*, vol. 47 Suppl 2, pp. T143–51, 2009.

[14] A. Krogh, "The number and distribution of capillaries in muscles with calculations of the oxygen pressure head necessary for supplying the tissue," *The Journal of Physiology*, vol. 52, no. 6, pp. 409–415, 1919.

[15] A. Krogh, "The supply of oxygen to the tissues and the regulation of the capillary circulation," *The Journal of Physiology*, vol. 52, no. 6, pp. 457–474, 1919.

[16] R. H. Thomlinson and L. H. Gray, "The histological structure of some human lung cancers and the possible implications for radiotherapy," *Br J Cancer*, vol. 9, no. 4, pp. 539–49, 1955.

[17] "Measurement of oxygen diffusion distance in tumor cubes using a fluorescent hypoxia probe," *International Journal of Radiation Oncology, volume =*.

[18] L. P. Schwab, D. L. Peacock, D. Majumdar, J. F. Ingels, L. C. Jensen, K. D. Smith, R. C. Cushing, and T. N. Seagroves, "Hypoxia-inducible factor 1 promotes primary tumor growth and tumor-initiating cell activity in breast cancer," *Breast Cancer Res*, vol. 14, no. 1, p. R6, 2012.

[19] R. Gatenby and R. Gillies, "Why do cancers have high aerobic glycolysis?," *Nat Rev Cancer*, vol. 4, no. 11, pp. 891–899, 2004.

[20] E. A. Jaffe, "Cell biology of endothelial cells"," *Human Pathology*, vol. 18, no. 3, pp. 234 – 239, 1987.

[21] H. G. Augustin, D. H. Kozian, and R. C. Johnson, "Differentiation of endothelial cells: Analysis of the constitutive and activated endothelial cell phenotypes," *BioEssays*, vol. 16, no. 12, pp. 901–906, 1994.

[22] J. Folkman, "Angiogenesis," *Annu Rev Med*, vol. 57, pp. 1–18, 2006.

[23] R. K. Jain, "Determinants of tumor blood flow: a review," *Cancer Res*, vol. 48, no. 10, pp. 2641–58, 1988.

[24] P. Carmeliet and R. K. Jain, "Angiogenesis in cancer and other diseases," *Nature*, vol. 407, no. 6801, pp. 249–57, 2000.

[25] P. Vaupel, A. Mayer, S. Briest, and M. Höckel, *Hypoxia in Breast Cancer*, pp. 333–342. Boston, MA: Springer US, 2005.

[26] A. Hall, "The role of angiogenesis in cancer," *Comp Clin Path*, vol. 13, pp. 95–99, 2005.

[27] J. Stephenson, J. Goddard, O. Al-Taan, A. Dennison, and B. Morgan, "Tumour angiogenesis: A growth area- from John Hunter to Judah Folkmanreard and beyond," *J Cancer Res*, pp. 1–6, 2013.

[28] A. G. Ide, N. H. Baker, and S. L. Warren, "Vascularization of the Brown Pearce rabbit epithelioma transplant as seen in the transparent ear chamber," *Am. J. Roentgeno*, vol. 42, 1939.

[29] G. H. Algire, H. W. Chalkley, F. Y. Legallais, and H. D. Park, "Vascular reactions of normal and malignant tissues in vivo. I. vascular reactions of mice to wounds and to normal and neoplastic transplants," *J. Natl Cancer Inst.*, vol. 6, 1945.

[30] M. Greenblatt and P. Shubick, "Tumor angiogenesis: transfilter diffusion studies in the hamster by the transparent chamber technique," *J. Natl Cancer Inst.*, vol. 41, 1968.

[31] R. Ehrmann and M. Knoth, "Choriocarcinoma. transfilter stimulation of vasoproliferation in the hamster cheek pouch. studied by light and electron microscopy," *J. Natl Cancer Inst.*, vol. 41, 1968.

[32] J. Folkman, "Tumor angiogenesis: therapeutic implications," *N Engl J Med*, vol. 285, no. 21, pp. 1182–6, 1971.

[33] A. L. Harris, "Hypoxia–a key regulatory factor in tumour growth," *Nat Rev Cancer*, vol. 2, no. 1, pp. 38–47, 2002.

[34] R. K. Jain, "Antiangiogenesis strategies revisited: from starving tumors to alleviating hypoxia," *Cancer Cell*, vol. 26, no. 5, pp. 605–22, 2014.

[35] E. M. Conway, D. Collen, and P. Carmeliet, "Molecular mechanisms of blood vessel growth," *Cardiovascular Research*, vol. 49, no. 3, pp. 507–521, 2001.

[36] P. Carmeliet, "Mechanisms of angiogenesis and arteriogenesis," *Nature medicine*, vol. 6, pp. 389–95, 04 2000.

[37] P. H. Burri, R. Hlushchuk, and V. Djonov, "Intussusceptive angiogenesis: Its emergence, its characteristics, and its significance," *Developmental Dynamics*, vol. 231, no. 3, pp. 474–488, 2004.

[38] D. Senger, S. Galli, A. Dvorak, C. Perruzzi, V. Harvey, and H. Dvorak, "Tumor cells secrete a vascular permeability factor that promotes accumulation of ascites fluid," *Science*, vol. 219, no. 4587, pp. 983–985, 1983.

[39] H. Gerhardt, M. Golding, M. Fruttiger, C. Ruhrberg, A. Lundkvist, A. Abramsson, M. Jeltsch, C. Mitchell, K. Alitalo, D. Shima, and C. Betsholtz, "VEGF guides angiogenic sprouting utilizing endothelial tip cell filopodia," *The Journal of Cell Biology*, vol. 161, no. 6, pp. 1163–1177, 2003.

[40] H. L. Goel and A. M. Mercurio, "VEGF targets the tumour cell," *Nat Rev Cancer*, vol. 13, no. 12, pp. 871–82, 2013.

[41] P. Carmeliet, "Angiogenesis in health and disease," *Nat Med*, vol. 9, no. 6, pp. 653–60, 2003.

[42] G. D. Yancopoulos, S. Davis, N. W. Gale, J. S. Rudge, S. J. Wiegand, and J. Holash, "Vascular-specific growth factors and blood vessel formation," *Nature*, vol. 407, no. 6801, pp. 242–8, 2000.

[43] R. S. Kerbel, "Tumor angiogenesis," *N Engl J Med*, vol. 358, no. 19, pp. 2039–49, 2008.

[44] N. W. Gale and G. D. Yancopoulos, "Growth factors acting via endothelial, cell-specific receptor tyrosine kinases: VEGFs, angiopoietins, and ephrins in vascular development," *Genes and Dev*, vol. 13, 1999.

[45] P. Carmeliet, L. Moons, A. Luttun, V. Vincenti, V. Compernolle, M. De Mol, Y. Wu, F. Bono, L. Devy, H. Beck, D. Scholz, T. Acker, T. DiPalma, M. Dewerchin, A. Noel, I. Stalmans, and A. Barra, "Synergism between vascular endothelial growth factor and placental growth factor contributes to angiogenesis and plasma extravasation in pathological conditions," *Nature medicine*, vol. 7, pp. 575–83, 05 2001.

[46] S. Bellou, G. Pentheroudakis, C. Murphy, and T. Fotsis, "Anti-angiogenesis in cancer therapy: Hercules and hydra," *Cancer Lett*, vol. 338, no. 2, pp. 219–28, 2013.

[47] J. M. Ebos, M. Mastri, C. R. Lee, A. Tracz, J. M. Hudson, K. Attwood, W. R. Cruz-Munoz, C. Jedeszko, P. Burns, and R. S. Kerbel, "Neoadjuvant antiangiogenic therapy reveals contrasts in primary and metastatic tumor efficacy," *EMBO Mol Med*, vol. 6, no. 12, pp. 1561–76, 2014.

[48] N. Ferrara, K. J. Hillan, H.-P. Gerber, and W. Novotny, "Discovery and development of bevacizumab, an anti-VEGF antibody for treating cancer," *Nature Reviews.Drug Discovery*, vol. 3, pp. 391–400, 05 2004.

[49] R. K. Jain, "Normalization of tumor vasculature: an emerging concept in antiangiogenic therapy," *Science*, vol. 307, no. 5706, pp. 58–62, 2005.

[50] M. B. Sasongko, T. Y. Wong, T. T. Nguyen, C. Y. Cheung, J. E. Shaw, and J. J. Wang, "Retinal vascular tortuosity in persons with diabetes and diabetic retinopathy," *Diabetologia*, vol. 54, pp. 2409–2416, Sep 2011.

[51] T. Y. Wong, R. Klein, B. E. Klein, J. M. Tielsch, L. Hubbard, and F. J. Nieto, "Retinal microvascular abnormalities and their relationship with hypertension, cardiovascular disease, and mortality," *Surv Ophthalmol*, vol. 46, no. 1, pp. 59–80, 2001.

[52] H. Ozaki, H. Hayashi, S. A. Vinores, Y. Moromizato, P. A. Campochiaro, and K. Oshima, "Intravitreal sustained release of VEGF causes retinal neovascularization in rabbits and breakdown of the blood retinal barrier in rabbits and primates," *Experimental Eye Research*, vol. 64, no. 4, pp. 505 – 517, 1997.

[53] R. Robinson, C. E. H. Ho, Q. S. W. Tan, C. D. Luu, K. T. Moe, C. Y. Cheung, T. Y. Wong, and V. A. Barathi, "Fluvastatin downregulates VEGF-A expression in TNF-α induced retinal vessel tortuosity," *Investigative Ophthalmology and Visual Science*, vol. 52, no. 10, p. 7423, 2011.

[54] M. E. Hartnett, D. Martiniuk, G. Byfield, P. Geisen, G. Zeng, and V. L. Bautch, "Neutralizing VEGF decreases tortuosity and alters endothelial cell division orientation in arterioles and veins in a rat model of ROP: relevance to plus disease," *Invest Ophthalmol Vis Sci*, vol. 49, no. 7, pp. 3107–14, 2008.

[55] P. Carmeliet and R. K. Jain, "Principles and mechanisms of vessel normalization for cancer and other angiogenic diseases," *Nat Rev Drug Discov*, vol. 10, no. 6, pp. 417–27, 2011.

[56] J. A. Nagy, S. H. Chang, A. M. Dvorak, and H. F. Dvorak, "Why are tumour blood vessels abnormal and why is it important to know?," *Br J Cancer*, vol. 100, no. 6, pp. 865–869, 2009.

[57] A. Saaristo, T. Veikkola, B. Enholm, M. Hytonen, J. Arola, K. Pajusola, P. Turunen, M. Jeltsch, M. J. Karkkainen, D. Kerjaschki, H. Bueler, S. Yla-Herttuala, and K. Alitalo, "Adenoviral VEGF-C overexpression induces blood vessel enlargement, tortuosity, and leakiness but no sprouting angiogenesis in the skin or mucous membranes," *FASEB J*, vol. 16, no. 9, pp. 1041–9, 2002.

[58] S. Goel, D. G. Duda, L. Xu, L. L. Munn, Y. Boucher, D. Fukumura, and R. K. Jain, "Normalization of the vasculature for treatment of cancer and other diseases," *Physiol Rev*, vol. 91, no. 3, pp. 1071–121, 2011.

[59] R. Bauer, S. Sheehan, and J. Meyer, "Arteriographic study of cerebrovascular disease: I. cerebral symptoms due to kinking, tortuosity, and compression of carotid and vertebral arteries in the neck," *Archives of Neurology*, vol. 4, no. 2, pp. 119–131, 1961.

[60] D. Fukumura and R. K. Jain, "Tumor microvasculature and microenvironment: targets for anti-angiogenesis and normalization," *Microvasc Res*, vol. 74, no. 2-3, pp. 72–84, 2007.

[61] W. E. Stehbens, C. J. Fee, and G. R. Stehbens, "Flow through s-shaped glass models simulating arterial tortuosities," *Q J Exp Physiol*, vol. 72, no. 2, pp. 201–13, 1987.

[62] N. S. Greenhill and W. E. Stehbens, "Haemodynamically-induced intimal tears in experimental u-shaped arterial loops as seen by scanning electron microscopy," *Br J Exp Pathol*, vol. 66, no. 5, pp. 577–84, 1985.

[63] W. E. Stehbens, "Experimental arterial loops and arterial atrophy," *Exp Mol Pathol*, vol. 44, no. 2, pp. 177–89, 1986.

[64] M. E. Skalina, W. L. Annable, R. M. Kliegman, and A. A. Fanaroff, "Hypertensive retinopathy in the newborn infant," *J Pediatr*, vol. 103, no. 5, pp. 781–6, 1983.

[65] C. Y. Cheung, W. T. Tay, P. Mitchell, J. J. Wang, W. Hsu, M. L. Lee, Q. P. Lau, A. L. Zhu, R. Klein, S. M. Saw, and T. Y. Wong, "Quantitative and qualitative retinal microvascular characteristics and blood pressure," *J Hypertens*, vol. 29, no. 7, pp. 1380–91, 2011.

[66] J. A. Kylstra, T. Wierzbicki, M. L. Wolbarsht, r. Landers, M. B., and E. Stefansson, "The relationship between retinal vessel tortuosity, diameter, and transmural pressure," *Graefes Arch Clin Exp Ophthalmol*, vol. 224, no. 5, pp. 477–80, 1986.

[67] N. C. Taarnhoj, I. C. Munch, B. Sander, L. Kessel, J. L. Hougaard, K. Kyvik, T. I. Sorensen, and M. Larsen, "Straight versus tortuous retinal arteries in relation to blood pressure and genetics," *Br J Ophthalmol*, vol. 92, no. 8, pp. 1055–60, 2008.

[68] T. L. Young, D. C. Anthony, E. Pierce, E. Foley, and L. E. Smith, "Histopathology and vascular endothelial growth factor in untreated and diode laser-treated retinopathy of prematurity," *J AAPOS*, vol. 1, no. 2, pp. 105–10, 1997.

[69] M. Patasius, V. Marozas, A. Lukosevicius, and D. Jegelevicius, "Model based investigation of retinal vessel tortuosity as a function of blood pressure: preliminary results," *Conf Proc IEEE Eng Med Biol Soc*, vol. 2007, pp. 6460–3, 2007.

[70] S. Suresh, "Biomechanics and biophysics of cancer cells," *Acta Biomater*, vol. 3, no. 4, pp. 413–38, 2007.

[71] A. Hellstrm, L. E. Smith, and O. Dammann, "Retinopathy of prematurity," *The Lancet*, vol. 382, no. 9902, pp. 1445 – 1457, 2013.

[72] C. Heneghan, J. Flynn, M. O'Keefe, and M. Cahill, "Characterization of changes in blood vessel width and tortuosity in retinopathy of prematurity using image analysis," *Med Image Anal*, vol. 6, no. 4, pp. 407–29, 2002.

[73] M. B. Sasongko, T. Y. Wong, K. C. Donaghue, N. Cheung, A. J. Jenkins, P. Benitez-Aguirre, and J. J. Wang, "Retinal arteriolar tortuosity is associated with retinopathy and early kidney dysfunction in type 1 diabetes," *American Journal of Ophthalmology*, vol. 153, no. 1, pp. 176 – 183.e1, 2012.

[74] C. Y. Cheung, Y. Zheng, W. Hsu, M. L. Lee, Q. P. Lau, P. Mitchell, J. J. Wang, R. Klein, and T. Y. Wong, "Retinal vascular tortuosity, blood pressure, and cardiovascular risk factors," *Ophthalmology*, vol. 118, no. 5, pp. 812–8, 2011.

[75] M. L. Aisen, B. R. Bacon, A. M. Goodman, and E. M. Chester, "Retinal abnormalities associated with anemia," *Arch Ophthalmol*, vol. 101, no. 7, pp. 1049–52, 1983.

[76] M. Carney and C. E. Ravin, "Intercostal artery laceration during thoracocentesis: increased risk in elderly patients," *Chest*, vol. 75, no. 4, pp. 520–2, 1979.

[77] V. J. Rodrigues, S. Elsayed, B. L. Loeys, H. C. Dietz, and D. M. Yousem, "Neuroradiologic manifestations of Loeys-Dietz syndrome type 1," *AJNR Am J Neuroradiol*, vol. 30, no. 8, pp. 1614–9, 2009.

[78] S. A. Morris, D. B. Orbach, T. Geva, M. N. Singh, K. Gauvreau, and R. V. Lacro, "Increased vertebral artery tortuosity index is associated with adverse outcomes in children and young adults with connective tissue disorders," *Circulation*, vol. 124, no. 4, pp. 388–96, 2011.

[79] Y. G. Wolf, M. Tillich, W. A. Lee, G. D. Rubin, T. J. Fogarty, and C. K. Zarins, "Impact of aortoiliac tortuosity on endovascular repair of abdominal aortic aneurysms: evaluation of 3d computer-based assessment," *J Vasc Surg*, vol. 34, no. 4, pp. 594–9, 2001.

[80] N. B. Wood, S. Z. Zhao, A. Zambanini, M. Jackson, W. Gedroyc, S. A. Thom, A. D. Hughes, and X. Y. Xu, "Curvature and tortuosity of the superficial femoral artery: a possible risk factor for peripheral arterial disease," *J Appl Physiol (1985)*, vol. 101, no. 5, pp. 1412–8, 2006.

[81] E. Bullitt, D. Zeng, B. Mortamet, A. Ghosh, S. R. Aylward, W. Lin, B. L. Marks, and K. Smith, "The effects of healthy aging on intracerebral blood vessels

visualized by magnetic resonance angiography," *Neurobiology of Aging*, vol. 31, no. 2, pp. 290 – 300, 2010.

[82] E. Bullitt, F. Rahman, J. Smith, E. Kim, D. Zeng, L. Katz, and B. Marks, "The effect of exercise on the cerebral vasculature of healthy aged subjects as visualized by MR angiography," *American Journal of Neuroradiology*, vol. 30, no. 10, pp. 1857–1863, 2009.

[83] E. Bullitt, K. E. Muller, I. Jung, W. Lin, and S. Aylward, "Analyzing attributes of vessel populations," *Med Image Anal*, vol. 9, no. 1, pp. 39–49, 2005.

[84] E. Bullitt, D. A. Reardon, and J. K. Smith, "A review of micro and macro vascular analyses in the assessment of tumor-associated vasculature as visualized by mr," *Neuroimage*, vol. 37, pp. S116–S119, 2007.

[85] P. Sladkevicius, L. Jokubkiene, and L. Valentin, "Contribution of morphological assessment of the vessel tree by three-dimensional ultrasound to a correct diagnosis of malignancy in ovarian masses," *Ultrasound Obstet Gynecol*, vol. 30, no. 6, pp. 874–82, 2007.

[86] R. P. Kedar, D. Cosgrove, V. R. McCready, J. C. Bamber, and E. R. Carter, "Microbubble contrast agent for color doppler US: effect on breast masses. work in progress," *Radiology*, vol. 198, no. 3, pp. 679–86, 1996.

[87] A. Sodi, M. Guarducci, L. Vauthier, A. S. Ioannidis, S. Pitz, G. Abbruzzese, F. Sofi, A. Mecocci, A. Miele, and U. Menchini, "Computer assisted evaluation of retinal vessels tortuosity in fabry disease," *Acta Ophthalmol*, vol. 91, no. 2, pp. e113–9, 2013.

[88] A. Scott, M. B. Powner, and M. Fruttiger, "Quantification of vascular tortuosity as an early outcome measure in oxygen induced retinopathy (OIR)," *Exp Eye Res*, vol. 120, pp. 55–60, 2014.

[89] S. Yasuda, S. Kachi, M. Kondo, S. Ueno, H. Kaneko, and H. Terasaki, "Significant correlation between retinal venous tortuosity and aqueous vascular endothelial growth factor concentration in eyes with central retinal vein occlusion," *PLoS One*, vol. 10, no. 7, p. e0134267, 2015.

[90] M. Taudorf, L. P. Jensen, K. C. Vogt, J. Gronvall, T. V. Schroeder, and L. Lonn, "Endograft limb occlusion in evar: iliac tortuosity quantified by three different indices on the basis of preoperative CTA," *Eur J Vasc Endovasc Surg*, vol. 48, no. 5, pp. 527–33, 2014.

[91] P. Lanzer, *Interventional X-Ray Coronary Angiography*, pp. 279–301. Springer-Verlag, 2012.

[92] M. J. Johnson and G. Dougherty, "Robust measures of three-dimensional vascular tortuosity based on the minimum curvature of approximating polynomial spline fits to the vessel mid-line," *Med Eng Phys*, vol. 29, no. 6, pp. 677–90, 2007.

[93] F. Calliada, R. Campani, O. Bottinelli, A. Bozzini, and M. G. Sommaruga, "Ultrasound contrast agents: Basic principles," *European Journal of Radiology*, vol. 27, no. Supplement 2, pp. S157 – S160, 1998.

[94] R. Gramiak and P. M. Shah, "Echocardiography of the aortic root," *Invest Radiol*, vol. 3, no. 5, pp. 356–66, 1968.

[95] J. B. Seward, A. J. Tajik, D. J. Hagler, and D. G. Ritter, "Peripheral venous contrast echocardiography," *The American Journal of Cardiology*, vol. 39, no. 2, pp. 202 – 212, 1977.

[96] C. Tei, T. Sakamaki, P. M. Shah, S. Meerbaum, K. Shimoura, S. Kondo, and E. Corday, "Myocardial contrast echocardiography: a reproducible technique of myocardial opacification for identifying regional perfusion deficits.," *Circulation*, vol. 67, no. 3, pp. 585–593, 1983.

[97] W. J. Bommer, P. M. Shah, H. Allen, R. Meltzer, and J. Kisslo, "The safety of contrast echocardiography: Report of the committee on contrast echocardiography for the american society of echocardiography," *Journal of the American College of Cardiology*, vol. 3, no. 1, pp. 6 – 13, 1984.

[98] N. C. Nanda, "History of echocardiographic contrast agents," *Clinical Cardiology*, vol. 20, no. S1, pp. 7–11, 1997.

[99] R. Schlief, "Echo-enhancing agents: their physics and pharmacology," in *Advances in echo imaging using contrast enhancement* (N. NC, S. R, and G. BB, eds.), Springer, Dordrecht, 1997.

[100] S. B. Feinstein, F. J. Ten Cate, W. Zwehl, K. Ong, G. Maurer, C. Tei, P. M. Shah, S. Meerbaum, and E. Corday, "Two-dimensional contrast echocardiography. i. in vitro development and quantitative analysis of echo contrast agents," *J Am Coll Cardiol*, vol. 3, no. 1, pp. 14–20, 1984.

[101] S. Feinstein, P. Heidenreich, C. Dick, J. Schneider, A. Pastoret, W. Rubenstein, J. Applebaum, J. Brehm, S. Aronson, J. Ellis, *et al.*, "Albunex: a new intravascular ultrasound contrast agent: preliminary safety and efficacy results," *Circulation*, vol. 78, no. Suppl II, p. 565, 1988.

[102] E. Quaia, "Microbubble ultrasound contrast agents: an update," *European Radiology*, vol. 17, pp. 1995–2008, Aug 2007.

[103] J. K. Willmann, Z. Cheng, C. Davis, A. M. Lutz, M. L. Schipper, C. H. Nielsen, and S. S. Gambhir, "Targeted microbubbles for imaging tumor angiogenesis: assessment of whole-body biodistribution with dynamic micro-PET in mice," *Radiology*, vol. 249, no. 1, pp. 212–219, 2008.

[104] D. R. Morel, I. Schwieger, L. Hohn, J. Terrettaz, J. B. Llull, Y. A. Cornioley, and M. Schneider, "Human pharmacokinetics and safety evaluation of sonovue, a new contrast agent for ultrasound imaging," *Investigative radiology*, vol. 35, no. 1, p. 80, 2000.

[105] J.-M. Correas, A. R. Meuter, E. Singlas, D. R. Kessler, D. Worah, and S. C. Quay, "Human pharmacokinetics of a perfluorocarbon ultrasound contrast agent evaluated with gas chromatography," *Ultrasound in medicine & biology*, vol. 27, no. 4, pp. 565–570, 2001.

[106] E. Quaia and T. Bartolotta, *Contrast Media in Ultrasonography: Basic Principles and Applications*. Springer, January 2005.

[107] B. Schrope, V. L. Newhouse, and V. Uhlendorf, "Simulated capillary blood flow measurement using a nonlinear ultrasonic contrast agent," *Ultrason Imaging*, vol. 14, no. 2, pp. 134–58, 1992.

[108] B. A. Schrope and V. L. Newhouse, "Second harmonic ultrasonic blood perfusion measurement," *Ultrasound Med Biol*, vol. 19, no. 7, pp. 567–79, 1993.

[109] T. R. Porter and F. Xie, "Transient myocardial contrast after initial exposure to diagnostic ultrasound pressures with minute doses of intravenously injected microbubbles - demonstration and potential mechanisms," *Circulation*, vol. 92, no. 9, pp. 2391–2395, 1995.

[110] F. A. Duck, "Nonlinear acoustics in diagnostic ultrasound," *Ultrasound in Medicine and Biology*, vol. 28, no. 1, pp. 1–18, 2002.

[111] D. H. Simpson, C. T. Chin, and P. N. Burns, "Pulse inversion doppler: a new method for detecting nonlinear echoes from microbubble contrast agents," *IEEE Trans Ultrason Ferroelectr Freq Control*, vol. 46, no. 2, pp. 372–82, 1999.

[112] P. Phillips, "Contrast pulse sequences (CPS): imaging nonlinear microbubbles," in *IEEE Ultrasonics Symposium*, vol. 2, pp. 1739–1745.

[113] B. Haider and R. Y. Chiao, "Higher order nonlinear ultrasonic imaging," *1999 Ieee Ultrasonics Symposium Proceedings, Vols 1 and 2*, pp. 1527–1531, 1999.

[114] R. J. Eckersley, C. T. Chin, and P. N. Burns, "Optimising phase and amplitude modulation schemes for imaging microbubble contrast agents at low acoustic power," *Ultrasound in Medicine and Biology*, vol. 31, no. 2, pp. 213–219, 2005.

[115] R. J. Eckersley, M. X. Tang, K. Chetty, and J. V. Hajnal, "Microbubble contrast agent detection using binary coded pulses," *Ultrasound in Medicine and Biology*, vol. 33, no. 11, pp. 1787–1795, 2007.

[116] P. M. Shankar, P. D. Krishna, and V. L. Newhouse, "Advantages of subharmonic over second harmonic backscatter for contrast-to-tissue echo enhancement," *Ultrasound in Medicine and Biology*, vol. 24, no. 3, pp. 395–399, 1998.

[117] W. T. Shi, F. Forsberg, J. Liu, L. Needleman, and B. B. Goldberg, "Nonlinear subharmonic imaging with us microbubble contrast agents," *Radiology*, vol. 213P, pp. 362–362, 1999.

[118] J. M. Borsboom, C. T. Chin, and N. de Jong, "Nonlinear coded excitation method for ultrasound contrast imaging," *Ultrasound Med Biol*, vol. 29, no. 2, pp. 277–84, 2003.

[119] C. Leavens, R. Williams, F. S. Foster, P. N. Burns, and M. D. Sherar, "Golay pulse encoding for microbubble contrast imaging in ultrasound," *IEEE Trans Ultrason Ferroelectr Freq Control*, vol. 54, no. 10, pp. 2082–90, 2007.

[120] Y. Sun, D. E. Kruse, and K. W. Ferrara, "Contrast imaging with chirped excitation," *IEEE Trans Ultrason Ferroelectr Freq Control*, vol. 54, no. 3, pp. 520–9, 2007.

[121] M. Crocco, P. Pellegretti, C. Sciallero, and A. Trucco, "Combining multi-pulse excitation and chirp coding in contrast-enhanced ultrasound imaging," *Measurement Science & Technology*, vol. 20, no. 10, 2009.

[122] O. Couture, M. Fink, and M. Tanter, "Ultrasound contrast plane wave imaging," *IEEE Transactions on Ultrasonics Ferroelectrics and Frequency Control*, vol. 59, no. 12, pp. 2676–2683, 2012.

[123] C. Tremblay-Darveau, R. Williams, L. Milot, M. Bruce, and P. N. Burns, "Combined perfusion and doppler imaging using plane-wave nonlinear detection and microbubble contrast agents," *IEEE Transactions on Ultrasonics Ferroelectrics and Frequency Control*, vol. 61, no. 12, pp. 1988–2000, 2014.

[124] S. W. Hell and J. Wichmann, "Breaking the diffraction resolution limit by stimulated emission: stimulated-emission-depletion fluorescence microscopy," *Opt. Lett.*, vol. 19, pp. 780–782, Jun 1994.

[125] E. Betzig, G. H. Patterson, R. Sougrat, O. W. Lindwasser, S. Olenych, J. S. Bonifacino, M. W. Davidson, J. Lippincott-Schwartz, and H. F. Hess, "Imaging intracellular fluorescent proteins at nanometer resolution," *Science*, vol. 313, no. 5793, pp. 1642–1645, 2006.

[126] O. M. Viessmann, R. J. Eckersley, K. Christensen-Jeffries, M. X. Tang, and C. Dunsby, "Acoustic super-resolution with ultrasound and microbubbles," *Phys Med Biol*, vol. 58, no. 18, pp. 6447–58, 2013.

[127] M. A. O'Reilly and K. Hynynen, "A super-resolution ultrasound method for brain vascular mapping," *Med Phys*, vol. 40, no. 11, p. 110701, 2013.

[128] Y. Desailly, O. Couture, M. Fink, and M. Tanter, "Sono-activated ultrasound localization microscopy," *Applied Physics Letters*, vol. 103, no. 17, 2013.

[129] K. Christensen-Jeffries, R. J. Browning, M. X. Tang, C. Dunsby, and R. J. Eckersley, "In vivo acoustic super-resolution and super-resolved velocity mapping using microbubbles," *IEEE Trans Med Imaging*, vol. 34, no. 2, pp. 433–40, 2015.

[130] C. Errico, J. Pierre, S. Pezet, Y. Desailly, Z. Lenkei, O. Couture, and M. Tanter, "Ultrafast ultrasound localization microscopy for deep super-resolution vascular imaging," *Nature*, vol. 527, no. 7579, pp. 499–502, 2015.

[131] F. Lin, S. E. Shelton, D. Espindola, J. D. Rojas, G. Pinton, and P. A. Dayton, "3-d ultrasound localization microscopy for identifying microvascular morphology features of tumor angiogenesis at a resolution beyond the diffraction limit of conventional ultrasound," *Theranostics*, vol. 7, no. 1, pp. 196–204, 2017.

[132] N. de Jong, A. Bouakaz, and P. Frinking, "Harmonic imaging for ultrasound contrast agents," in *Ultrasonics Symposium, 2000 IEEE*, vol. 2, pp. 1869–1876, IEEE, 2000.

[133] T. Muir and E. Carstensen, "Prediction of nonlinear acoustic effects at biomedical frequencies and intensities," *Ultrasound in medicine & biology*, vol. 6, no. 4, pp. 345–357, 1980.

[134] E. Carstensen, W. Law, N. McKay, and T. Muir, "Demonstration of nonlinear acoustical effects at biomedical frequencies and intensities," *Ultrasound in medicine & biology*, vol. 6, no. 4, pp. 359–368, 1980.

[135] A. Bouakaz, S. Frigstad, F. J. Ten Cate, and N. de Jong, "Super harmonic imaging: A new imaging technique for improved contrast detection," *Ultrasound in Medicine and Biology*, vol. 28, no. 1, pp. 59–68, 2002.

[136] A. Bouakaz, S. Frigstad, F. J. Ten Cate, and N. de Jong, "Improved contrast to tissue ratio at higher harmonics," *Ultrasonics*, vol. 40, no. 1, pp. 575–578, 2002.

[137] A. Bouakaz, F. ten Cate, and N. de Jong, "A new ultrasonic transducer for improved contrast nonlinear imaging," *Physics in medicine and biology*, vol. 49, no. 16, p. 3515, 2004.

[138] P. L. M. J. V. Neer, G. Matte, M. G. Danilouchkine, C. Prins, F. V. D. Adel, and N. D. Jong, "Super-harmonic imaging: development of an interleaved phased-array transducer," *IEEE Transactions on Ultrasonics, Ferroelectrics, and Frequency Control*, vol. 57, pp. 455–468, February 2010.

[139] D. E. Kruse and K. W. Ferrara, "A new imaging strategy using wideband transient response of ultrasound contrast agents," *IEEE Transactions on Ultrasonics Ferroelectrics and Frequency Control*, vol. 52, no. 8, pp. 1320–1329, 2005.

[140] S. Zhao, D. E. Kruse, K. W. Ferrara, and P. A. Dayton, "Selective imaging of adherent targeted ultrasound contrast agents," *Phys Med Biol*, vol. 52, no. 8, pp. 2055–72, 2007.

[141] X. W. Hu, H. R. Zheng, D. E. Kruse, P. Sutcliffe, D. N. Stephens, and K. W. Ferrara, "A sensitive TLRH targeted imaging technique for ultrasonic molecular imaging," *IEEE Transactions on Ultrasonics Ferroelectrics and Frequency Control*, vol. 57, no. 2, pp. 305–316, 2010.

[142] X. Hu, C. F. Caskey, L. M. Mahakian, D. E. Kruse, J. R. Beegle, A. E. Decleves, J. J. Rychak, P. L. Sutcliffe, K. Sharma, and K. W. Ferrara, "In vivo validation and 3d visualization of broadband ultrasound molecular imaging," *Am J Nucl Med Mol Imaging*, vol. 3, no. 4, pp. 336–49, 2013.

[143] R. Gessner, M. Lukacs, M. Lee, E. Cherin, F. S. Foster, and P. A. Dayton, "High-resolution, high-contrast ultrasound imaging using a prototype dual-frequency transducer: in vitro and in vivo studies," *IEEE Trans Ultrason Ferroelectr Freq Control*, vol. 57, no. 8, pp. 1772–81, 2010.

[144] R. C. Gessner, S. R. Aylward, and P. A. Dayton, "Mapping microvasculature with acoustic angiography yields quantifiable differences between healthy and tumor-bearing tissue volumes in a rodent model," *Radiology*, vol. 264, no. 3, pp. 733–40, 2012.

[145] R. C. Gessner, C. B. Frederick, F. S. Foster, and P. A. Dayton, "Acoustic angiography: a new imaging modality for assessing microvasculature architecture," *Int J Biomed Imaging*, vol. 2013, p. 936593, 2013.

[146] B. D. Lindsey, J. D. Rojas, and P. Dayton, "On the relationship between microbubble fragmentation, deflation, and broadband superharmonic signal production," *Ultrasound Med Biol*, vol. 41, no. 6, pp. 1711–1725, 2014.

[147] B. D. Lindsey*, S. E. Shelton*, and P. Dayton, "Optimization of contrast-to-tissue ratio through pulse windowing in dual-frequency "acoustic angiography" imaging," *Ultrasound Med Biol*, vol. 41, no. 7, pp. 1884–95, 2015.

[148] S. E. Shelton, Y. Lee, F. S. Foster, M. Lee, E. Cherin, S. R. Aylward, and P. Dayton, "Quantification of microvascular tortuosity during tumor evolution utilizing acoustic angiography," *Ultrasound Med Biol*, vol. 41, no. 7, pp. 1896–1904, 2015.

[149] S. Rao, S. Shelton, and P. Dayton, "The 'fingerprint' of cancer extends beyond solid tumor boundaries: assessment with a novel ultrasound imaging approach," *IEEE Trans Biomed Eng*, vol. 63, no. 5, pp. 1082–1086, 2015.

[150] B. D. Lindsey*, S. E. Shelton*, F. S. Foster, and P. A. Dayton, "Assessment of molecular acoustic angiography for combined microvascular and molecular imaging in preclinical tumor models," *Mol Imaging Biol*, 2016.

[151] B. D. Lindsey, S. E. Shelton, K. H. Martin, K. A. Ozgun, J. D. Rojas, F. S. Foster, and P. A. Dayton, "High resolution ultrasound superharmonic perfusion imaging: In vivo feasibility and quantification of dynamic contrast-enhanced acoustic angiography," *Annals of biomedical engineering*, pp. 1–10, 2016.

[152] J. Ma, K. H. Martin, P. A. Dayton, and X. Jiang, "A preliminary engineering design of intravascular dual-frequency transducers for contrast-enhanced acoustic angiography and molecular imaging," *IEEE transactions on ultrasonics, ferroelectrics, and frequency control*, vol. 61, no. 5, pp. 870–880, 2014.

[153] J. Ma, K. H. Martin, Y. Li, P. A. Dayton, K. K. Shung, Q. Zhou, and X. Jiang, "Design factors of intravascular dual frequency transducers for super-harmonic contrast imaging and acoustic angiography," *Physics in medicine and biology*, vol. 60, no. 9, p. 3441, 2015.

[154] J. Kim, S. Li, S. Kasoji, P. A. Dayton, and X. Jiang, "Phantom evaluation of stacked-type dual-frequency 1–3 composite transducers: A feasibility study on intracavitary acoustic angiography," *Ultrasonics*, vol. 63, pp. 7–15, 2015.

[155] K. H. Martin, B. D. Lindsey, J. Ma, T. C. Nichols, X. Jiang, and P. A. Dayton, "Ex vivo porcine arterial and chorioallantoic membrane acoustic angiography using dual-frequency intravascular ultrasound probes," *Ultrasound in medicine & biology*, vol. 42, no. 9, pp. 2294–2307, 2016.

[156] B. D. Lindsey, K. H. Martin, X. Jiang, and P. A. Dayton, "Adaptive windowing in contrast-enhanced intravascular ultrasound imaging," *Ultrasonics*, vol. 70, pp. 123–135, 2016.

[157] Y. Li, J. Ma, K. H. Martin, M. Yu, T. Ma, P. A. Dayton, X. Jiang, K. K. Shung, and Q. Zhou, "An integrated system for superharmonic contrast-enhanced ultrasound imaging: Design and intravascular phantom imaging study," *IEEE Transactions on Biomedical Engineering*, vol. 63, no. 9, pp. 1933–1943, 2016.

[158] Z. Wang, K. H. Martin, W. Huang, P. A. Dayton, and X. Jiang, "Contrast enhanced superharmonic imaging for acoustic angiography using reduced form-factor lateral mode transmitters for intravascular and intracavity applications," *IEEE transactions on ultrasonics, ferroelectrics, and frequency control*, vol. 64, no. 2, pp. 311–319, 2017.

[159] B. D. Lindsey, J. D. Rojas, K. H. Martin, S. E. Shelton, and P. A. Dayton, "Acoustic characterization of contrast-to-tissue ratio and axial resolution for dual-frequency contrast-specific acoustic angiography imaging," *IEEE Trans Ultrason Ferroelectr Freq Control*, vol. 61, no. 10, pp. 1668–87, 2014.

[160] A. L. Anderson and L. D. Hampton, "Acoustics of gas-bearing sediments i. background," *The Journal of the Acoustical Society of America*, vol. 67, no. 6, pp. 1865–1889, 1980.

[161] I. G. Maroulakou, M. Anver, L. Garrett, and J. E. Green, "Prostate and mammary adenocarcinoma in transgenic mice carrying a rat c3(1) simian virus 40 large tumor antigen fusion gene," *Proc Natl Acad Sci U S A*, vol. 91, no. 23, pp. 11236–40, 1994.

[162] J. E. Green, M. A. Shibata, K. Yoshidome, M. L. Liu, C. Jorcyk, M. R. Anver, J. Wigginton, R. Wiltrout, E. Shibata, S. Kaczmarczyk, W. Wang, Z. Y. Liu, A. Calvo, and C. Couldrey, "The c3(1)/sv40 t-antigen transgenic mouse model of mammary cancer: ductal epithelial cell targeting with multistage progression to carcinoma," *Oncogene*, vol. 19, no. 8, pp. 1020–7, 2000.

[163] T. Schroeder, H. Yuan, B. L. Viglianti, C. Peltz, S. Asopa, Z. Vujaskovic, and M. W. Dewhirst, "Spatial heterogeneity and oxygen dependence of glucose consumption in R3230Ac and fibrosarcomas of the Fischer 344 rat," *Cancer Research*, vol. 65, no. 12, pp. 5163–5171, 2005.

[164] J. P. Grant and S. A. Wells, "Tumor resistance in rats immunized to fetal tissues," *Journal of Surgical Research*, vol. 16, no. 5, pp. 533 – 540, 1974.

[165] L. M. Imaging, "Definity prescribing information," April, 2013 2013.

[166] S. R. Aylward and E. Bullitt, "Initialization, noise, singularities, and scale in height ridge traversal for tubular object centerline extraction," *IEEE Trans Med Imaging*, vol. 21, no. 2, pp. 61–75, 2002.

[167] R Core Team, *R: A Language and Environment for Statistical Computing*. R Foundation for Statistical Computing, Vienna, Austria, 2015.

[168] X. Robin, N. Turck, A. Hainard, N. Tiberti, F. Lisacek, J.-C. Sanchez, and M. Mller, "pROC: an open-source package for R and S+ to analyze and compare ROC curves," *BMC Bioinformatics*, vol. 12, p. 77, 2011.

[169] T. Sing, O. Sander, N. Beerenwinkel, and T. Lengauer, "ROCR: visualizing classifier performance in r," *Bioinformatics*, vol. 21, no. 20, p. 7881, 2005.

[170] M. López-Ratón, M. X. Rodríguez-Álvarez, C. C. Suárez, and F. G. Sampedro, "OptimalCutpoints: An R package for selecting optimal cutpoints in diagnostic tests," *Journal of Statistical Software*, vol. 61, no. 8, pp. 1–36, 2014.

[171] M. Hahsler, *Density Based Clustering of Applications with Noise (DBSCAN) and Related Algorithms*, 2016.

[172] D. Adler, D. Murdoch, and others, *rgl: 3D Visualization Using OpenGL*, 2016.

[173] P. Rouhani, C. D. M. Fletcher, S. S. Devesa, and J. R. Toro, "Cutaneous soft tissue sarcoma incidence patterns in the U.S.," *Cancer*, vol. 113, no. 3, pp. 616–627, 2008.

[174] G. Bergers and L. E. Benjamin, "Tumorigenesis and the angiogenic switch," *Nature Reviews.Cancer*, vol. 3, pp. 401–10, 06 2003.

[175] S. E. Dahln, J. Bjrk, P. Hedqvist, K. E. Arfors, S. Hammarstrm, J. A. Lindgren, and B. Samuelsson, "Leukotrienes promote plasma leakage and leukocyte adhesion in postcapillary venules: in vivo effects with relevance to the acute inflammatory response," *Proceedings of the National Academy of Sciences*, vol. 78, no. 6, pp. 3887–3891, 1981.

[176] E. Mori, G. J. del Zoppo, J. D. Chambers, B. R. Copeland, and K. E. Arfors, "Inhibition of polymorphonuclear leukocyte adherence suppresses no-reflow after focal cerebral ischemia in baboons.," *Stroke*, vol. 23, no. 5, pp. 712–718, 1992.

[177] A. N. Tosteson, M. C. Weinstein, J. Wittenberg, and C. B. Begg, "ROC curve regression analysis: the use of ordinal regression models for diagnostic test assessment," *Environmental Health Perspectives*, vol. 102, no. Suppl 8, pp. 73–78.

[178] S. Dreiseitl and L. Ohno-Machado, "Logistic regression and artificial neural network classification models: a methodology review," *Journal of Biomedical Informatics*, vol. 35, no. 5, pp. 352 – 359, 2002.

[179] M. Ester, H. Kriegel, J. Sander, and X. Xu, "A density-based algorithm for discovering clusters in large spatial databases with noise," in *Data Mining and Knowledge Discovery*, pp. 226–231, 2003.

[180] L. Ertoz, M. Steinbach, and V. Kumar, "Finding clusters of different sizes, shapes, and densities in noisy, high dimensional data," in *in Proceedings of Second SIAM International Conference on Data Mining*, 2003.

[181] R. Xu and D. Wunsch, "Survey of clustering algorithms," *IEEE Transactions on Neural Networks*, vol. 16, pp. 645–678, May 2005.

[182] R. M. Haralick and L. G. Shapiro, "Image segmentation techniques," *Computer Vision, Graphics, and Image Processing*, vol. 29, no. 1, pp. 100 – 132, 1985.

[183] T. Tiirikka, M. Siermala, and M. Vihinen, "Clustering of gene ontology terms in genomes," *Gene*, vol. 550, no. 2, pp. 155 – 164, 2014.

[184] Y. R. Wang and H. Huang, "Review on statistical methods for gene network reconstruction using expression data," *Journal of Theoretical Biology*, vol. 362, no. Supplement C, pp. 53 – 61, 2014.

[185] G. Kerr, H. Ruskin, M. Crane, and P. Doolan, "Techniques for clustering gene expression data," *Computers in Biology and Medicine*, vol. 38, no. 3, pp. 283 – 293, 2008.

[186] D. Jiang, C. Tang, and A. Zhang, "Cluster analysis for gene expression data: a survey," *IEEE Transactions on Knowledge and Data Engineering*, vol. 16, pp. 1370–1386, Nov 2004.

[187] P. Dhaeseleer, S. Liang, and R. Somogyi, "Genetic network inference: from co-expression clustering to reverse engineering," *Bioinformatics*, vol. 16, no. 8, pp. 707–726, 2000.

[188] M. E. Celebi, Y. A. Aslandogan, and P. R. Bergstresser, "Mining biomedical images with density-based clustering," in *International Conference on Information Technology: Coding and Computing (ITCC'05) - Volume II*, vol. 1, pp. 163–168 Vol. 1, April 2005.

[189] F. Ren, L. Hu, H. Liang, X. Liu, and W. Ren, "Using density-based incremental clustering for anomaly detection," in *2008 International Conference on Computer Science and Software Engineering*, vol. 3, pp. 986–989, Dec 2008.

[190] M. Celik, F. Dadaser-Celik, and A. S. Dokuz, "Anomaly detection in temperature data using DBSCAN algorithm," in *2011 International Symposium on Innovations in Intelligent Systems and Applications*, pp. 91–95, June 2011.

[191] B. A. Kaufmann and J. R. Lindner, "Molecular imaging with targeted contrast ultrasound," *Curr Opin Biotechnol*, vol. 18, no. 1, pp. 11–6, 2007.

[192] J. U. Voigt, "Ultrasound molecular imaging," *Methods*, vol. 48, no. 2, pp. 92–7, 2009.

[193] A. Needles, O. Couture, and F. Foster, "A method for differentiating targeted microbubbles in real time using subharmonic micro-ultrasound and interframe filtering," *Ultrasound in medicine & biology*, vol. 35, no. 9, pp. 1564–1573, 2009.

[194] C. R. Anderson, J. J. Rychak, M. Backer, J. Backer, K. Ley, and A. L. Klibanov, "scVEGF microbubble ultrasound contrast agents: a novel probe for ultrasound

molecular imaging of tumor angiogenesis," *Invest Radiol*, vol. 45, no. 10, pp. 579–85, 2010.

[195] C. R. Anderson, X. Hu, H. Zhang, J. Tlaxca, A. E. Decleves, R. Houghtaling, K. Sharma, M. Lawrence, K. W. Ferrara, and J. J. Rychak, "Ultrasound molecular imaging of tumor angiogenesis with an integrin targeted microbubble contrast agent," *Invest Radiol*, vol. 46, no. 4, pp. 215–24, 2011.

[196] Y. Inaba and J. R. Lindner, "Molecular imaging of disease with targeted contrast ultrasound imaging," *Transl Res*, vol. 159, no. 3, pp. 140–8, 2012.

[197] J. M. Hyvelin, I. Tardy, T. Bettinger, M. von Wronski, M. Costa, P. Emmel, D. Colevret, P. Bussat, A. Lassus, C. Botteron, A. Nunn, P. Frinking, and F. Tranquart, "Ultrasound molecular imaging of transient acute myocardial ischemia with a clinically translatable P- and E-selectin targeted contrast agent: correlation with the expression of selectins," *Invest Radiol*, vol. 49, no. 4, pp. 224–35, 2014.

[198] J. M. Warram, A. G. Sorace, M. Mahoney, S. Samuel, B. Harbin, M. Joshi, A. Martin, L. Whitworth, K. Hoyt, and K. R. Zinn, "Biodistribution of P-selectin targeted microbubbles," *J Drug Target*, vol. 22, no. 5, pp. 387–94, 2014.

[199] H. Wang, O. F. Kaneko, L. Tian, D. Hristov, and J. K. Willmann, "Three-dimensional ultrasound molecular imaging of angiogenesis in colon cancer using a clinical matrix array ultrasound transducer," *Invest Radiol*, 2015.

[200] D. B. Khismatullin, "Resonance frequency of microbubbles: effect of viscosity," *J Acoust Soc Am*, vol. 116, no. 3, pp. 1463–73, 2004.

[201] E. Sassaroli and K. Hynynen, "Forced linear oscillations of microbubbles in blood capillaries," *J Acoust Soc Am*, vol. 115, no. 6, pp. 3235–43, 2004.

[202] C. F. Caskey, S. M. Stieger, S. Qin, P. A. Dayton, and K. W. Ferrara, "Direct observations of ultrasound microbubble contrast agent interaction with the microvessel wall," *Journal of the Acoustical Society of America*, vol. 122, no. 2, pp. 1191–1200, 2007.

[203] J. A. Feshitan, C. C. Chen, J. J. Kwan, and M. A. Borden, "Microbubble size isolation by differential centrifugation," *J Colloid Interface Sci*, vol. 329, no. 2, pp. 316–24, 2009.

[204] A. van Wamel, M. Celebi, and J. Hossack, "Molecular imaging with targeted contrast agents and high frequency ultrasound," *IEEE Ultrasonics Symposium Proceedings*, vol. 1, no. 6, pp. 961–964, 2004.

[205] R. J. Cerfolio, B. Ojha, A. S. Bryant, V. Raghuveer, J. M. Mountz, and A. A. Bartolucci, "The accuracy of integrated PET-CT compared with dedicated PET

alone for the staging of patients with nonsmall cell lung cancer," *Ann Thorac Surg*, vol. 78, no. 3, pp. 1017–23; discussion 1017–23, 2004.

[206] K. Tharp, O. Israel, J. Hausmann, L. Bettman, W. H. Martin, M. Daitzchman, M. P. Sandler, and D. Delbeke, "Impact of I-131-SPECT/CT images obtained with an integrated system in the follow-up of patients with thyroid carcinoma," *European Journal of Nuclear Medicine and Molecular Imaging*, vol. 31, no. 10, pp. 1435–1442, 2004.

[207] P. J. Roach, G. P. Schembri, I. A. H. Shon, E. A. Bailey, and D. L. Bailey, "SPECT/CT imaging using a spiral CT scanner for anatomical localization: Impact on diagnostic accuracy and reporter confidence in clinical practice," *Nuclear Medicine Communications*, vol. 27, no. 12, pp. 977–987, 2006.

[208] H. Lerman, G. Lievshitz, O. Zak, U. Metser, S. Schneebaum, and E. Even-Sapir, "Improved sentinel node identification by SPECT/CT in overweight patients with breast cancer," *Journal of Nuclear Medicine*, vol. 48, no. 2, pp. 201–206, 2007.

[209] Z. Garami, Z. Hascsi, J. Varga, T. Dinya, M. Tanyi, I. Garai, L. Damjanovich, and L. Galuska, "The value of 18-FDG PET/CT in early-stage breast cancer compared to traditional diagnostic modalities with an emphasis on changes in disease stage designation and treatment plan," *Eur J Surg Oncol*, vol. 38, no. 1, pp. 31–7, 2012.

[210] J. D. Soyka, M. A. Muster, D. T. Schmid, B. Seifert, U. Schick, R. Miralbell, S. Jorcano, K. Zaugg, H. H. Seifert, P. Veit-Haibach, K. Strobel, N. G. Schaefer, D. B. Husarik, and T. F. Hany, "Clinical impact of 18F-choline PET/CT in patients with recurrent prostate cancer," *Eur J Nucl Med Mol Imaging*, vol. 39, no. 6, pp. 936–43, 2012.

[211] S. E. Shelton*, B. D. Lindsey*, J. K. Tsuruta, F. S. Foster, and P. Dayton, "Molecular acoustic angiography: a new technique for high resolution superharmonic ultrasound molecular imaging," *Ultrasound in Medicine and Biology*, vol. 42, no. 3, pp. 769–781, 2015.

[212] S. Fokong, A. Fragoso, A. Rix, A. Curaj, Z. Wu, W. Lederle, O. Iranzo, J. Gatjens, F. Kiessling, and M. Palmowski, "Ultrasound molecular imaging of E-selectin in tumor vessels using poly n-butyl cyanoacrylate microbubbles covalently coupled to a short targeting peptide," *Invest Radiol*, vol. 48, no. 12, pp. 843–50, 2013.

[213] L. Biancone, M. Araki, K. Araki, P. Vassalli, and I. Stamenkovic, "Redirection of tumor metastasis by expression of E-selectin in vivo," *J Exp Med*, vol. 183, no. 2, pp. 581–7, 1996.

[214] D. Schadendorf, S. Diehl, T. Zuberbier, C. Schadendorf, and B. M. Henz, "Quantitative detection of soluble adhesion molecules in sera of melanoma patients correlates with clinical stage," *Dermatology*, vol. 192, no. 2, pp. 89–93, 1996.

[215] I. C. Haznedaroglu, M. Benekli, O. Ozcebe, M. C. Savas, I. H. Gullu, S. V. Dundar, and S. Kirazli, "Serum L-selectin and P-selectin levels in lymphomas," *Haematologia (Budap)*, vol. 30, no. 1, pp. 27–30, 2000.

[216] A. D. Blann, D. Gurney, M. Wadley, D. Bareford, P. Stonelake, and G. Y. Lip, "Increased soluble P-selectin in patients with haematological and breast cancer: a comparison with fibrinogen, plasminogen activator inhibitor and von Willebrand factor," *Blood Coagul Fibrinolysis*, vol. 12, no. 1, pp. 43–50, 2001.

[217] G. J. Caine, G. Y. Lip, and A. D. Blann, "Platelet-derived VEGF, Flt-1, angiopoietin-1 and P-selectin in breast and prostate cancer: further evidence for a role of platelets in tumour angiogenesis," *Ann Med*, vol. 36, no. 4, pp. 273–7, 2004.

[218] G. J. Caine, G. Y. Lip, P. S. Stonelake, P. Ryan, and A. D. Blann, "Platelet activation, coagulation and angiogenesis in breast and prostate carcinoma," *Thromb Haemost*, vol. 92, no. 1, pp. 185–90, 2004.

[219] M. Nguyen, J. Folkman, and J. Bischoff, "1-deoxymannojirimycin inhibits capillary tube formation in vitro. analysis of n-linked oligosaccharides in bovine capillary endothelial cells," *J Biol Chem*, vol. 267, no. 36, pp. 26157–65, 1992.

[220] A. E. Koch, M. M. Halloran, C. J. Haskell, M. R. Shah, and P. J. Polverini, "Angiogenesis mediated by soluble forms of E-selectin and vascular cell adhesion molecule-1," *Nature*, vol. 376, no. 6540, pp. 517–9, 1995.

[221] M. Aoki, M. Kanamori, K. Yudoh, K. Ohmori, T. Yasuda, and T. Kimura, "Effects of vascular endothelial growth factor and E-selectin on angiogenesis in the murine metastatic RCT sarcoma," *Tumour Biol*, vol. 22, no. 4, pp. 239–46, 2001.

[222] K. Egami, T. Murohara, M. Aoki, and T. Matsuishi, "Ischemia-induced angiogenesis: role of inflammatory response mediated by P-selectin," *J Leukoc Biol*, vol. 79, no. 5, pp. 971–6, 2006.

[223] I. Y. Oh, C. H. Yoon, J. Hur, J. H. Kim, T. Y. Kim, C. S. Lee, K. W. Park, I. H. Chae, B. H. Oh, Y. B. Park, and H. S. Kim, "Involvement of E-selectin in recruitment of endothelial progenitor cells and angiogenesis in ischemic muscle," *Blood*, vol. 110, no. 12, pp. 3891–9, 2007.

[224] A. K. Stannard, R. Khurana, I. M. Evans, V. Sofra, D. I. Holmes, and I. Zachary, "Vascular endothelial growth factor synergistically enhances induction of E-selectin by tumor necrosis factor-alpha," *Arterioscler Thromb Vasc Biol*, vol. 27, no. 3, pp. 494–502, 2007.

[225] *SEER Cancer Statistics Factsheets: Female Breast Cancer.* National Cancer Institute.

[226] F. E. Alexander, T. J. Anderson, H. K. Brown, A. P. Forrest, W. Hepburn, A. E. Kirkpatrick, B. B. Muir, R. J. Prescott, and A. Smith, "14 years of follow-up from the Edinburgh randomised trial of breast-cancer screening," *Lancet*, vol. 353, no. 9168, pp. 1903–8, 1999.

[227] N. Bjurstam, L. Bjorneld, J. Warwick, E. Sala, S. W. Duffy, L. Nystrom, N. Walker, E. Cahlin, O. Eriksson, L. O. Hafstrom, H. Lingaas, J. Mattsson, S. Persson, C. M. Rudenstam, H. Salander, J. Save-Soderbergh, and T. Wahlin, "The Gothenburg breast screening trial," *Cancer*, vol. 97, no. 10, pp. 2387–96, 2003.

[228] American College of Radiology, "Breast imaging reporting and data system BI-RADS," *American College of Radiology*, 2013.

[229] E. A. Rafferty, J. M. Park, L. E. Philpotts, S. P. Poplack, J. H. Sumkin, E. F. Halpern, and L. T. Niklason, "Assessing radiologist performance using combined digital mammography and breast tomosynthesis compared with digital mammography alone: results of a multicenter, multireader trial," *Radiology*, vol. 266, no. 1, pp. 104–13, 2013.

[230] J. Shan, A. W. Tucker, Y. Z. Lee, M. D. Heath, X. Wang, D. H. Foos, J. Lu, and O. Zhou, "Stationary chest tomosynthesis using a carbon nanotube x-ray source array: a feasibility study," *Phys Med Biol*, vol. 60, no. 1, pp. 81–100, 2015.

[231] A. W. Tucker, J. Calliste, E. M. Gidcumb, J. Wu, C. M. Kuzmiak, N. Hyun, D. Zeng, J. Lu, O. Zhou, and Y. Z. Lee, "Comparison of a stationary digital breast tomosynthesis system to magnified 2D mammography using breast tissue specimens," *Acad Radiol*, vol. 21, no. 12, pp. 1547–52, 2014.

[232] H. Elsamaloty, M. S. Elzawawi, S. Mohammad, and N. Herial, "Increasing accuracy of detection of breast cancer with 3-T MRI," *AJR Am J Roentgenol*, vol. 192, no. 4, pp. 1142–8, 2009.

[233] C. Mountford, S. Ramadan, P. Stanwell, and P. Malycha, "Proton MRS of the breast in the clinical setting," *NMR Biomed*, vol. 22, no. 1, pp. 54–64, 2009.

[234] W. K. Moon, D. Y. Noh, and J. G. Im, "Multifocal, multicentric, and contralateral breast cancers: bilateral whole-breast US in the preoperative evaluation of patients," *Radiology*, vol. 224, no. 2, pp. 569–76, 2002.

[235] D. L. Weaver, R. D. Rosenberg, W. E. Barlow, L. Ichikawa, P. A. Carney, K. Kerlikowske, D. S. Buist, B. M. Geller, C. R. Key, S. J. Maygarden, and R. Ballard-Barbash, "Pathologic findings from the breast cancer surveillance consortium: population-based outcomes in women undergoing biopsy after screening mammography," *Cancer*, vol. 106, no. 4, pp. 732–42, 2006.

[236] M. Boba, U. Koltun, B. Bobek-Billewicz, E. Chmielik, B. Eksner, and T. Olejnik, "False-negative results of breast core needle biopsies - retrospective analysis of 988 biopsies," *Pol J Radiol*, vol. 76, no. 1, pp. 25–9, 2011.

[237] "Physicians' considerations for repeat biopsy in patients with recurrent metastatic breast cancer," *Clinical breast cancer*, vol. 16, pp. 43–48, 2016.

[238] J. H. Youk, E. K. Kim, M. J. Kim, J. Y. Lee, and K. K. Oh, "Missed breast cancers at us-guided core needle biopsy: how to reduce them," *Radiographics*, vol. 27, no. 1, pp. 79–94, 2007.

[239] M. A. Hayes Balmadrid, R. A. Shelby, A. A. Wren, L. S. Miller, S. C. Yoon, J. A. Baker, L. A. Wildermann, and M. S. Soo, "Anxiety prior to breast biopsy: Relationships with length of time from breast biopsy recommendation to biopsy procedure and psychosocial factors," *J Health Psychol*, vol. 22, no. 5, pp. 561–571, 2017.

[240] J. Folkman and Y. Shing, "Angiogenesis," *J Biol Chem*, vol. 267, no. 16, pp. 10931–4, 1992.

[241] N. Weidner, J. P. Semple, W. R. Welch, and J. Folkman, "Tumor angiogenesis and metastasis–correlation in invasive breast carcinoma," *N Engl J Med*, vol. 324, no. 1, pp. 1–8, 1991.

[242] N. Weidner, J. Folkman, F. Pozza, P. Bevilacqua, E. N. Allred, D. H. Moore, S. Meli, and G. Gasparini, "Tumor angiogenesis: a new significant and independent prognostic indicator in early-stage breast carcinoma," *J Natl Cancer Inst*, vol. 84, no. 24, pp. 1875–87, 1992.

[243] H. E. Daldrup-Link, J. Rydland, T. H. Helbich, A. Bjornerud, K. Turetschek, K. A. Kvistad, E. Kaindl, T. M. Link, K. Staudacher, D. Shames, R. C. Brasch, O. Haraldseth, and E. J. Rummeny, "Quantification of breast tumor microvascular permeability with feruglose-enhanced MR imaging: initial phase II multicenter trial," *Radiology*, vol. 229, no. 3, pp. 885–92, 2003.

[244] J. M. Boone, A. L. Kwan, K. Yang, G. W. Burkett, K. K. Lindfors, and T. R. Nelson, "Computed tomography for imaging the breast," *J Mammary Gland Biol Neoplasia*, vol. 11, no. 2, pp. 103–11, 2006.

[245] D. D. Adler, P. L. Carson, J. M. Rubin, and D. Quinn-Reid, "Doppler ultrasound color flow imaging in the study of breast cancer: preliminary findings," *Ultrasound Med Biol*, vol. 16, no. 6, pp. 553–9, 1990.

[246] S. Barnard, E. Leen, T. Cooke, and W. Angerson, "A contrast-enhanced ultrasound study of benign and malignant breast tissue," *S Afr Med J*, vol. 98, no. 5, pp. 386–91, 2008.

[247] F. Forsberg, B. Kuruvilla, M. B. Pascua, M. H. Chaudhari, D. A. Merton, J. P. Palazzo, and B. B. Goldberg, "Comparing contrast-enhanced color flow imaging and pathological measures of breast lesion vascularity," *Ultrasound Med Biol*, vol. 34, no. 9, pp. 1365–72, 2008.

[248] K. Hoyt, H. Umphrey, M. Lockhart, M. Robbin, and A. Forero-Torres, "Ultrasound imaging of breast tumor perfusion and neovascular morphology," *Ultrasound Med Biol*, vol. 41, no. 9, pp. 2292–302, 2015.

[249] A. Sridharan, J. R. Eisenbrey, P. Machado, H. Ojeda-Fournier, A. Wilkes, A. Sevrukov, R. F. Mattrey, K. Wallace, C. L. Chalek, K. E. Thomenius, and F. Forsberg, "Quantitative analysis of vascular heterogeneity in breast lesions using contrast-enhanced 3-d harmonic and subharmonic ultrasound imaging," *IEEE Trans Ultrason Ferroelectr Freq Control*, vol. 62, no. 3, pp. 502–10, 2015.

[250] C. F. Wan, J. Du, H. Fang, F. H. Li, J. S. Zhu, and Q. Liu, "Enhancement patterns and parameters of breast cancers at contrast-enhanced us: correlation with prognostic factors," *Radiology*, vol. 262, no. 2, pp. 450–9, 2012.

[251] A. Ottinetti and A. Sapino, "Morphometric evaluation of microvessels surrounding hyperplastic and neoplastic mammary lesions," *Breast Cancer Res Treat*, vol. 11, no. 3, pp. 241–8, 1988.

[252] H. Rahbar, W. B. DeMartini, A. Y. Lee, S. C. Partridge, S. Peacock, and C. D. Lehman, "Accuracy of 3 T versus 1.5 T breast MRI for pre-operative assessment of extent of disease in newly diagnosed DCIS," *Eur J Radiol*, vol. 84, no. 4, pp. 611–6, 2015.

[253] K. Pinker, W. Bogner, P. Baltzer, S. Trattnig, S. Gruber, O. Abeyakoon, M. Bernathova, O. Zaric, P. Dubsky, Z. Bago-Horvath, M. Weber, D. Leithner, and T. H. Helbich, "Clinical application of bilateral high temporal and spatial resolution dynamic contrast-enhanced magnetic resonance imaging of the breast at 7 t," *Eur Radiol*, vol. 24, no. 4, pp. 913–20, 2014.

[254] C. S. Reiner, M. Roessle, T. Thiesler, D. Eberli, E. Klotz, T. Frauenfelder, T. Sulser, H. Moch, and H. Alkadhi, "Computed tomography perfusion imaging of renal cell carcinoma: systematic comparison with histopathological angiogenic and prognostic markers," *Invest Radiol*, vol. 48, no. 4, pp. 183–91, 2013.

[255] T. T. Rissanen, P. Korpisalo, H. Karvinen, T. Liimatainen, S. Laidinen, O. H. Grohn, and S. Yla-Herttuala, "High-resolution ultrasound perfusion imaging of therapeutic angiogenesis," *JACC Cardiovasc Imaging*, vol. 1, no. 1, pp. 83–91, 2008.

[256] K. H. Herrmann, S. Schmidt, A. Kretz, R. Haenold, I. Krumbein, M. Metzler, C. Gaser, O. W. Witte, and J. R. Reichenbach, "Possibilities and limitations for

high resolution small animal MRI on a clinical whole-body 3T scanner," *MAGMA*, vol. 25, no. 3, pp. 233–44, 2012.

[257] Z. Starosolski, C. A. Villamizar, D. Rendon, M. J. Paldino, D. M. Milewicz, K. B. Ghaghada, and A. V. Annapragada, "Ultra high-resolution in vivo computed tomography imaging of mouse cerebrovasculature using a long circulating blood pool contrast agent," *Sci Rep*, vol. 5, p. 10178, 2015.

[258] F. S. Foster, M. Y. Zhang, Y. Q. Zhou, G. Liu, J. Mehi, E. Cherin, K. A. Harasiewicz, B. G. Starkoski, L. Zan, D. A. Knapik, and S. L. Adamson, "A new ultrasound instrument for in vivo microimaging of mice," *Ultrasound Med Biol*, vol. 28, no. 9, pp. 1165–72, 2002.

[259] F. S. Foster, J. Mehi, M. Lukacs, D. Hirson, C. White, C. Chaggares, and A. Needles, "A new 15-50 MHz array-based micro-ultrasound scanner for preclinical imaging," *Ultrasound Med Biol*, vol. 35, no. 10, pp. 1700–8, 2009.

[260] P. Ricci, V. Cantisani, L. Ballesio, E. Pagliara, E. Sallusti, F. M. Drudi, F. Trippa, F. Calascibetta, S. M. Erturk, M. Modesti, and R. Passariello, "Benign and malignant breast lesions: efficacy of real time contrast-enhanced ultrasound vs. magnetic resonance imaging," *Ultraschall Med*, vol. 28, no. 1, pp. 57–62, 2007.

[261] H. Liu, Y. X. Jiang, J. B. Liu, Q. L. Zhu, and Q. Sun, "Evaluation of breast lesions with contrast-enhanced ultrasound using the microvascular imaging technique: Initial observations," *Breast*, vol. 17, no. 5, pp. 532–539, 2008.

[262] H. Zhao, R. Xu, Q. Ouyang, L. Chen, B. Dong, and Y. Huihua, "Contrast-enhanced ultrasound is helpful in the differentiation of malignant and benign breast lesions," *European Journal of Radiology*, vol. 73, no. 2, pp. 288 – 293, 2010.

[263] J. Bzyl, M. Palmowski, A. Rix, S. Arns, J.-M. Hyvelin, S. Pochon, J. Ehling, S. Schrading, F. Kiessling, and W. Lederle, "The high angiogenic activity in very early breast cancer enables reliable imaging with VEGFR2-targeted microbubbles (BR55)," *European Radiology*, vol. 23, no. 2, pp. 468–475, 2013.

[264] S. Pochon, I. Tardy, P. Bussat, T. Bettinger, J. Brochot, M. von Wronski, L. Passantino, and M. Schneider, "BR55: a lipopeptide-based VEGFR2-targeted ultrasound contrast agent for molecular imaging of angiogenesis," *Invest Radiol*, vol. 45, no. 2, pp. 89–95, 2010.

[265] J. K. Willmann, L. Bonomo, A. C. Testa, P. Rinaldi, G. Rindi, K. S. Valluru, G. Petrone, M. Martini, A. M. Lutz, and S. S. Gambhir, "Ultrasound molecular imaging with BR55 in patients with breast and ovarian lesions: First-in-human results," *Journal of Clinical Oncology*, vol. 0, no. 0, p. JCO.2016.70.8594, 0.

[266] G. Rubin and N. Rofsky, *CT & MRI Angiography: comprehensive vascular assessment*. Lippincott Williams and Wilkins, 2009.

[267] E. Bullitt, G. Gerig, S. M. Pizer, W. Lin, and S. R. Aylward, "Measuring tortuosity of the intracerebral vasculature from MRA images," *IEEE Trans Med Imaging*, vol. 22, no. 9, pp. 1163–71, 2003.

[268] E. Bullitt, P. A. Wolthusen, L. Brubaker, W. Lin, D. Zeng, and T. Van Dyke, "Malignancy-associated vessel tortuosity: a computer-assisted, MR angiographic study of choroid plexus carcinoma in genetically engineered mice," *AJNR Am J Neuroradiol*, vol. 27, no. 3, pp. 612–9, 2006.

[269] C. Y. Li, S. Shan, Q. Huang, R. D. Braun, J. Lanzen, K. Hu, P. Lin, and M. W. Dewhirst, "Initial stages of tumor cell-induced angiogenesis: evaluation via skin window chambers in rodent models," *J Natl Cancer Inst*, vol. 92, no. 2, pp. 143–7, 2000.

[270] M. A. Kotowycz, K. W. Johnston, J. Ivanov, N. Asif, A. M. Almoghairi, A. Choudhury, C. D. Nagy, M. Sibbald, W. Chan, P. H. Seidelin, A. W. Barolet, C. B. Overgaard, and V. Dzavik, "Predictors of radial artery size in patients undergoing cardiac catheterization: insights from the good radial artery size prediction (grasp) study," *Can J Cardiol*, vol. 30, no. 2, pp. 211–6, 2014.

[271] S. A. Feig, G. S. Shaber, A. Patchefsky, G. F. Schwartz, J. Edeiken, H. I. Libshitz, R. Nerlinger, R. F. Curley, and J. D. Wallace, "Analysis of clinically occult and mammographically occult breast tumors," *AJR Am J Roentgenol*, vol. 128, no. 3, pp. 403–8, 1977.

[272] B. D. Lindsey, J. Kim, P. A. Dayton, and X. Jiang, "Dual-frequency piezoelectric endoscopic transducer for imaging vascular invasion in pancreatic cancer," *IEEE Trans Ultrason Ferroelectr Freq Control*, vol. 64, no. 7, pp. 1078–1086, 2017.

[273] S. A. Jansen, T. Paunesku, X. Fan, G. E. Woloschak, S. Vogt, S. D. Conzen, T. Krausz, G. M. Newstead, and G. S. Karczmar, "Ductal carcinoma in situ: X-ray fluorescence microscopy and dynamic contrast-enhanced MR imaging reveals gadolinium uptake within neoplastic mammary ducts in a murine model," *Radiology*, vol. 253, no. 2, pp. 399–406, 2009.